New methodologies for electronic structure calculations on organic materials

by

Jason Douglas Weibel

B.S. Chemistry (North Carolina State University) 1994
B.S. Aerospace Engineering (North Carolina State University) 1994
M.S. Chemistry (Wake Forest University) 1996

A dissertation submitted in partial satisfaction of the
requirements for the degree of
Doctor of Philosophy

in

Chemistry

in the

GRADUATE DIVISION
of
CARNEGIE MELLON UNIVERSITY

Committee in charge:

David Yaron, Advisor
Hyung Kim
Jeffery Madura
Richard McCullough
Linda Peteanu

2001

New methodologies for electronic structure calculations on organic materials

This thesis is dedicated to Rebecca, Dylan, Douglas and Connie Weibel and to Thomas and Anne Marie Nicolls, thanks for all your help and support

Acknowledgements

I would like to thank my advisor, Dr. David Yaron for all his help in making sure that I was able to get the most out of my years here at Carnegie Mellon.

I would also like to thank the members of my committee, Dr. Hyung Kim, Dr. Jeffery Madura, Dr. Richard McCullough, and Dr. Linda Peteanu for taking time out of their schedules to act as my examining committee. Dr. Kim has been most helpful with his insight into the theoretical aspects of my work and Dr.'s Peteanu and McCullough have been extremely important in reminding me of the experimental aspects of chemistry, helping to keep me in touch with reality.

I would also like to thank the other members of the Yaron group, past and present, and especially Missy and Eric who were here in the beginning. And I would also like to thank all the members of the department of chemistry for helping make this experience a truly memorable one, for interesting and stimulating scientific discussions, and for all their help and support. I also gratefully acknowledge all the help Rea Freeland has given me working on my presentation and question answering skills. I also greatly appreciate all the support that I have received from my family, in-laws, and from my friends outside of the chemistry department.

Finally, I am deeply indebted to all the help, conversation, confidence, and support that I have received from my wifie Rebecca, and now also from our little boy, Dylan.

Contents

II Periodic Materials 53

List of Tables

List of Figures

Abstract

New methodologies for electronic structure calculations on organic materials

by

Jason Douglas Weibel
Doctor of Philosophy in Chemistry

Carnegie Mellon University

David Yaron, Advisor

Organic materials have great potential for use in electronic and photophysical devices. A detailed understanding of the electronic structure of these materials will allow us to better understand the structure-property relationships of relevance to device design. This thesis develops and applies methods for studying the electronic structure of three classes of organic electronic materials: nonlinear optical chromophores, conjugated polymers, and carbon nanotubes.

The first part of this thesis examines the nonlinear optical properties of multipolar organic chromophores. This is done by extending the internal field model of Oudar, which is applicable only to pseudo one-dimensional systems such as push-pull polyenes, to chromophores with general multi-dimensional acceptor-donor substitution patterns. The model developed here takes full account of the multipolar nature of the internal potential applied by the acceptors and donors, and the tensor properties of the resulting nonlinear optical susceptibility. The model is tested against quantum chemical calculations on representative systems.

The second part of this thesis concerns the development of a method that allows intermediate neglect of differential overlap (INDO) calculations to be performed under periodic boundary conditions. This allows the results of calculations on conjugated polymers to be expressed in the language of solid state physics. The method is used to study the absorption spectrum of poly(para-phenylene vinylene) (PPV). INDO calculations on oligomers of PPV as well as long chains with periodic boundary conditions

are reported. The long-chain calculations are used to assign the spectral features to transitions between bands, and these assignments are transferred to oligomers by examining how the calculated oligomer spectra evolve with chain length. The combination of periodic calculations and oligomer calculations enables a more complete description of the experimental absorption spectra of PPV and its derivatives.

The second part of this thesis also examines electron-hole symmetry breaking in carbon nanotubes. This study is facilitated by an analytical approach for including the effects of next-nearest-neighbor interactions in Hückel calculations on carbon nanotubes. These next-nearest-neighbor interactions break electron-hole symmetry. While this symmetry breaking does not alter the band gap, it does alter the thermoelectric power which is zero in a system that has electron-hole symmetry.

The third and final part of this thesis extends the dynamic dielectric model of Moore *et al.* Inclusion of dielectric effects is necessary to obtain reliable exciton binding energies for conjugated polymers. The original dynamic dielectric model used Hückel theory to describe the polarization induced in the dielectric medium. Here, this Hückel model is replaced by a more accurate Pariser-Parr-Pople model. The results indicate that the use of Hückel theory is valid, provided the parameters are chosen correctly.

Chapter 1

Introduction

Organic materials have opened up many possibilities in the creation of electronic devices such as flat screen displays[3, 4], lasers[5, 6], nonlinear optical chromophores[7, 8, 9, 10, 11], and transistors[12]. The potential advantages of using organic materials include ease of construction, low cost, low weight, and flexibility.[9, 8, 13] To take full advantage of the structural flexibility afforded by organic synthesis, it is useful to have a more complete understanding of the relationships between the chemical structure and the properties of relevance to device design. The electronic and photophysical properties are directly related to the electronic structure of the materials, and the development and application of electronic structure methods to these materials is an active area of research.[14, 15, 16, 17, 18, 9, 7, 8, 19, 20, 11] This thesis develops and applies a number of new methods for studying the electronic structure of organic materials. The materials and methods studied here can be grouped into three classes of organic electronic materials: nonlinear optical chromophores, conjugated polymers, and carbon nanotubes.

1.1 Thesis overview

Part I of this thesis deals with calculations on non-linear optical materials. These materials typically consist of medium-sized organic molecules that are collected into a bulk sample to form an actual device. In these systems, calculations on single molecules are adequate to reflect the properties of the bulk sample.[21, 9] Chapter 2 develops some background on the materials, including traditional chromophores and new multipolar chromophores that have become of interest due to the development of optical poling techniques. It is the description of these new multipolar chromophores that motivated the theory developed here.

An expansion of the energy of the molecule in a field, F, defines the nonlinear optical susceptibilities,

$$W = W_0 - \mu F - \frac{1}{2}\alpha F^2 - \frac{1}{3}\beta F^3 - \frac{1}{4}\gamma F^4 - \cdots, \tag{1.1}$$

where W_0 is the energy in zero field, and the nonlinear optical susceptibilities are tensors of increasing rank, μ first rank, α second rank, β third rank, γ fourth rank, and so on. The increasingly complex tensor nature of the higher order terms in the expansion makes their description increasingly challenging. Additionally, since the odd order rank susceptibilities are zero in a molecule or bulk sample that is centrosymmetric, methods must be found to ensure an non-centrosymmetric distribution.

Traditionally, nonlinear optical chromophores are created by adding electron donor and/or acceptor substituents to the ends of a linear centrosymmetric molecular skeleton. The presence of the substituents breaks the inversion center of the molecular skeleton and creates a dipole moment within the molecule. The absence of a center of symmetry allows for the possibility of non-zero odd-order nonlinear susceptibilities, such as the first hyperpolarizability, β. The presence of a dipole moment also allows the molecules of the bulk sample to be aligned using a dc electric field. Since the substituents typically lie along the same axis, the hyperpolarizabilities of these traditional linear, rod-like molecules are dominated by a single component. This one-dimensional character greatly simplifies the analysis. In particular, Oudar derived a one-dimensional internal field model that relates the response of the molecule to the properties of the skeleton.[22]

Optical poling has made it possible to utilize a new class of chromophores with multi-dimensional substitution patterns. For a multi-polar system, the response may no longer be dominated by a single component. The possibility of multiple components in the response has necessitated the development of a model where the electron acceptors and donors are viewed as creating an internal potential within the molecule and the susceptibilities are treated in their full tensorial form.

Chapter 3 begins our development of a general internal potential model for multipolar non-linear optical chromophores. Viewing the substituents as creating an internal potential and using the full tensor expansion of the energy allows for a model that, similar to the linear model, relates the non-linear response to the substitution pattern of acceptors and donors on the molecular skeleton.

The internal field model is a linear response theory. To obtain information from the complex tensorial relationship between the internal field and the hyperpolarizability, the potentials are first expressed in vector form. The relationship between the internal potential and the hyperpolarizability then reduces to a matrix multiplication. To analyse the relationship between substitution and hyperpolarizability response, singular value decomposition (SVD) is performed on the matrix connecting the internal potential and hyperpolarizability response ($\mathbf{L}$).

To examine the effectiveness of the generalized internal potential model, calculations are performed on a benzene skeleton and a series of substituted benzenes. In a highly symmetric molecule, such as benzene, symmetry analysis and singular value decomposition give the same results. Calculations done using internal potential patterns with arbitrary strength and on a series of substituted benzene skeletons with substituents of varying strength provide information about the range of chemical acceptors and donors over which the generalized internal potential model is valid.

Chapter 4 continues our examination of the generalized internal potential model through calculations on three additional molecular skeletons. The symmetry analysis and singular value decomposition for these additional molecular skeletons are performed following the methods of Chapter 3.

Part II of this thesis concerns calculations done on a different class of molecular system. In this part, calculations are performed on conjugated polymers and molecules for which the use of periodic boundary conditions is convenient. Chapter 5 provides a general background on periodic boundary conditions, outlining concepts such as the lattice of the system, the reciprocal lattice, the Brillouin zone, forms for periodic wave functions, and an example of the evaluation of an operator under periodic boundary conditions.

Chapter 6 discusses and establishes the formalism for using the intermediate neglect of differential overlap (INDO) model under periodic boundary conditions. Development of this model allows the results of calculations to be stated in the context of solid state physics, so comparisons can be made with other calculations. Calculations performed under periodic boundary conditions also allow the optical transitions in oligomers to be assigned to bands.

As an application of this approach, we study the absorption spectrum of poly(*para*-phenylene vinylene) (PPV) and the questions concerning assignment of the UV/VIS absorption spectrum. The use of the INDO model allows for geometric effects, such as non-planar molecular geometries, to be examined and the periodic boundary conditions allow band assignments to be made. In addition to calculations utilizing periodic boundary conditions, calculations are also done on a series of PPV oligomers with varying numbers of phenylene rings. The long-chain calculations are used to assign the spectral features to transitions between bands, and these assignments are transferred to oligomers by examining how the calculated oligomer spectra evolve with chain length. From our study, the combination of finite chain size, substituents, and non-planarity of the sample results in a better understanding of the absorption spectra.

Chapter 7 concerns the examination of electron-hole symmetry breaking in carbon nanotubes. This is facilitated by a new method for inclusion of next-nearest-neighbor interactions in such systems. This method uses a graph theoretical representation of system connectivity to derive an analytical expression for the effects of next-nearest-neighbor interactions. These interactions break electron-hole symmetry by expanding the valence bands and contracting the conduction bands. While this symmetry breaking does not alter the band gap, it does alter the thermoelectric power. In a system with electron-hole symmetry, the thermoelectric power is zero.[23, 24, 25] The method developed here allows the thermoelectric power of a single nanotube to be determined analytically.

Finally, Part III and Chapter 8 examine dielectric effects in calculations on conjugated polymers. Semi-empirical quantum chemistry consistently determines exciton binding energies that are larger than those seen in experiment.[26, 27, 28] To obtain agreement with experiment, many quantum chemical calculations are parameterized so that the Coulombic repulsion between electrons is much lower than that found in gas phase calculations.[29, 30, 31] This likely reflects the importance of interactions between polymer chains in the solid state. Our group has previously developed a dynamic dielectric model that explicitly includes dielectric interactions with surrounding polymer chains.[32] Chapter 8 continues the investigation into this dynamic dielectric model. Originally, the model used Hückel theory for the solvent chains. Here, the Pariser-Parr-Pople model is used for the solvent, and the results are compared to those obtained using the Hückel model. The results indicate that the use of Hückel theory is adequate, provided the Hückel parameters are chosen appropriately.

Part I

Nonlinear Optical Materials

Chapter 2

A brief introduction to nonlinear optical materials

2.1 Introduction

The energy of a molecule in an external electric field, F, can be expanded as follows,

$$W = W_0 - \mu F - \frac{1}{2}\alpha F^2 - \frac{1}{3}\beta F^3 - \frac{1}{4}\gamma F^4 - \cdots, \tag{2.1}$$

where W_0 is the energy in zero field, and the nonlinear optical susceptibilities are tensors of increasing rank, μ first rank, α second rank, β third rank, γ fourth rank, and so on. The response of primary interest here is the first hyperpolarizability, or second order nonlinear optical susceptibility, β.

Odd-order responses, such as the first hyperpolarizability, are zero if the molecule or bulk sample is centrosymmetric.[33] Typically, construction of a nonlinear optical chromophore starts with a centrosymmetric molecule, to which substituents are added to break the center of symmetry. In the bulk sample, these molecules may be randomly distributed so as to produce a centrosymmetric distribution. To obtain a bulk second order nonlinear optical susceptibility, a methods must be found to align the molecules and create a non-centrosymmetric distribution. In molecules with a permanent dipole moment, the molecules may be aligned with a dc electric field. In more complicated molecules that may not possess a permanent dipole moment, alternative methods, such as optical poling, must be found to induce alignment.

Traditionally, linear molecules with a permanent dipole moment have been used to generate nonlinear optical responses because the presence of the dipole allows for alignment of the molecules in the bulk sample through the use of a dc electric field. The design scheme of these types of molecules is typically pseudo one-dimensional,

[Donor]-[Electronic conjugated pathway]-[Acceptor],

with the conjugated pathway being benzene, polyene, stilbene or similar conjugated molecular skeleton.[7] Variations in conjugation length and acceptor and/or donor strength are common methods undertaken to optimize the nonlinear response, while still maintaining a reasonable stability.[7, 10, 9] It has been shown that β should scale with chain length.[34, 9] Therefore, one method of attempting to achieve large hyperpolarizabilities is to increase the chain length between electron and donor groups. Along these lines, Marder *et al.* have been able to achieve high hyperpolarizabilities by reducing the effective bond length alternation in the conjugated pathway. This is done by tuning the relative contributions of neutral and charge-separated resonance to the ground electronic state. They have been able to achieve hyperpolarizabilities between 20 and $911 \mathrm{x} 10^{-30}$ esu.[10]

Collection and alignment of linear optical chromophores in the bulk sample is often done using corona poling.[35] In corona poling the sample is dispersed in a polymer matrix. The chromophore/polymer matrix is then heated above the glass transition temperature of the polymer matrix in the presence of a strong electric field. Heating the system above the polymer's glass transition temperature allows the chromophores to align in response to the applied electric field and create a noncentrosymmetric distribution. The system is then allowed to cool in the presence of the electric field, retaining the alignment in the bulk sample.

2.2 Multipolar systems

Another class of materials whose hyperpolarizability response is under investigation is molecules with multi-dimensional substitution patterns.[7, 8] Often, the multi-dimensional molecules do not possess a permanent dipole moment, precluding the use of a dc electric field to align the molecules in the bulk sample. Elimination of the center of symmetry in collections of multi-polar molecules can be achieved through the use of optical poling methods. One such molecule of interest is ethyl violet, an octupolar triphenyl based *para*-substituted cation. Zyss *et al.* have been able to achieve a hyperpolarizability response of between 510 and 580x10^{-30} esu in ethyl violet after optical poling.[36, 37]

Progressing beyond an effectively one-dimensional model opens up a wealth of two- and three-dimensional chemical possibilities. One must also keep in mind that, at this time, the goal of the study of multi-dimensional chromophores is not necessarily to maximize the response, but to eliminate some of the problems associated with the linear molecules, such as disruption of crystallization due to dipolar aggregation, the necessity of using electric fields to achieve parallel alignment of the molecules, limits on the electrooptic applications due to the anisotropic structure of the material, and the requirement that the modulating field and optical beam both be parallel to the common crystalline and molecular axis.[7, 8]

One way of understanding and predicting the nonlinear optical behavior of a molecule is to develop models that relate the substitution pattern on a molecular skeleton to the optical response that is generated by the potential field induced by those substituents. When the chemical substituents of the molecule lie along the same axis, the responses due to the internal field created by these substituents are dominated by a single component. Because the responses are essentially one-dimensional, a direct relationship between the internal field and the hyperpolarizability response can be derived. For a more complicated, multi-dimensional substitution pattern, the responses due to the internal field are no longer dominated by a single component. In order to account for the multi-dimensional nature of the substitution pattern, the expansion of the energy of the molecule is done in its full tensorial form. A relationship similar to the one-dimensional one can then be found for any substitution pattern. The development of the generalized model for the hyperpolarizability response can be found in detail in chapters 3 and 4.

2.3 Optical poling

In order for a material to exhibit an odd-order response such as β, the material cannot be centrosymmetric and/or a non-centrosymmetric distribution in the bulk material must produced. Traditionally, quasi one-dimensional, rod-like, linear molecules that possess a permanent dipole moment have been used in applications because the dipole allows the non-centrosymmetric distrubution of molecules in the bulk sample to be created using a dc electric field.

For a multi-dimensional substitution pattern, such as the octupolar substituted benzene of Figure 2.1, the molecule may no longer possess a permanent dipole moment and thus a dc electric field can not be used to achieve molecular alignment. Optical poling methods have been developed that allow for the center of symmetry of the bulk sample to be broken, even in molecules without a permanent dipole moment.[37, 21, 7, 8] The optical poling methods uses interference between one- and two-photon absorption processes to discriminate between molecules based on molecular orientation. In other words, only molecules in certain orientations within the sample will be excited by the incoming light beams creating orientational hole burning conditions. The excited molecules then undergo relaxation through some photo-induced isomerization, intramolecular, or intermolecular vibrational process, resulting in a distribution of molecular orientations that differs from the one present at the start of the optical poling process.

As an example, we will start by defining the orientation of a D_{3h} type molecule by an angle φ (Figure 2.1). Then let us assume, for illustrative purposes, that the possible orientations of the molecules in the sample are evenly distributed (Figure 2.2). Let the excitation by the write beams only effect those orientations of φ between φ_1 and φ_2. This subset of molecules will then relax, resulting in a distribution of the relaxed molecules similar to that of the initial configuration. The new overall distribution of

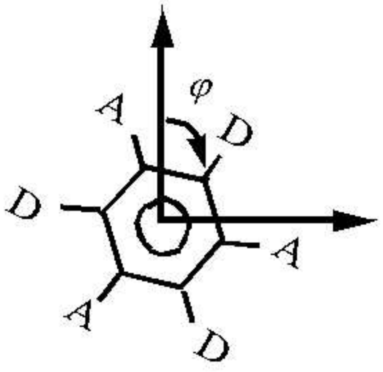

Figure 2.1: Sample D_{3h} molecule defining the angle φ used to discriminate between the various orientations of the molecule.

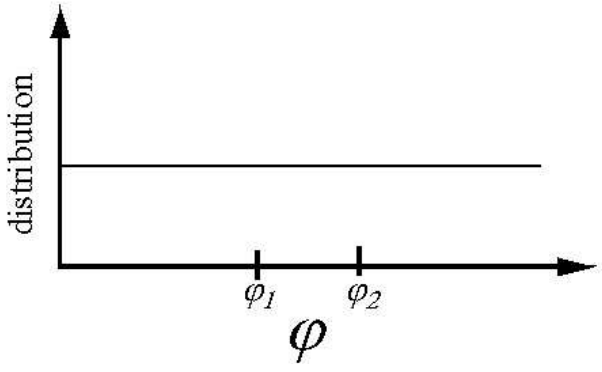

Figure 2.2: Plot of relative abundance vs. orientation angle, φ for a evenly distributed sample.

orientations will have a dip in the area between φ_1 and φ_2 (Figure 2.3).

2.4 The write field tensor

Optical poling breaks center of symmetry in the sample through a multiphoton absorption process described by the write field tensor, a time-averaged tensorial product of optical fields, $\left\langle E^{2\omega *} \otimes E^{\omega} \otimes E^{\omega} \right\rangle_t$. [37, 21, 36, 8] The combination of optical fields on the sample takes advantage of an interference pattern created by a combination of one and two photon absorption processes (see Figure 2.4). The power of the incoming light beams is chosen so both absorption processes of Figure 2.4 would

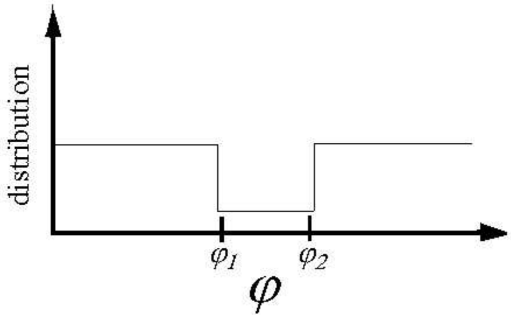

Figure 2.3: Plot of relative abundance vs. orientation angle, φ for the sample after having undergone the hole-burning, optical poling process.

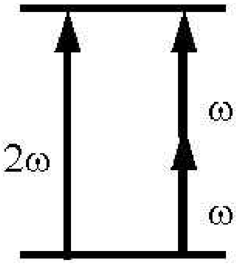

Figure 2.4: Schematic of the the one and two photon absorption processes involved in optical poling.

lead to equivalent population transfers.

Examination of how the optical fields can interact to produce the necessary interference patterns can be achieved by considering the electric field components of the impinging optical fields. A general form of the electric field vector of the incident optical field is

$$\vec{E}(\vec{r},t) = (E_1\hat{\epsilon}_1 + E_2\hat{\epsilon}_2)\, e^{(i\vec{k}\cdot\vec{r}-i\omega t)}, \tag{2.2}$$

where E_1 and E_2 are the complex amplitudes of the vector in the directions $\hat{\epsilon}_1$ and $\hat{\epsilon}_2$ respectively, $\vec{k}$ is the wave vector, $\vec{r}$ is the direction of propagation, and ω is the frequency.[38] There are two important concepts in considering the effects of the write field tensor,

$$\left\langle E^{2\omega *} \otimes E^{\omega} \otimes E^{\omega} \right\rangle_t, \tag{2.3}$$

on the sample. First, the time average of eq. 2.3 must be non-zero. Second, coupling of the three electric field vectors of the optical fields must have the symmetry components required for interaction with molecules of corresponding symmetry.

To determine the conditions necessary for optical poling we will start by considering two fields with arbitrary frequencies, ω_1 and ω_2. The product of the fields of eq. 2.2 in eq. 2.3 is,

$$E^{(\omega_2)*} \otimes E^{(\omega_1)} \otimes E^{(\omega_1)} = \vec{A}^* e^{(-i\vec{k}_{\omega_2}\cdot\vec{r}+i\omega_2 t)} \otimes \vec{B} e^{(i\vec{k}_{\omega_1}\cdot\vec{r}-i\omega_1 t)} \otimes \vec{B} e^{(i\vec{k}_{\omega_1}\cdot\vec{r}-i\omega_1 t)}, \tag{2.4}$$

where $\vec{A}$ and $\vec{B}$ are the vector components of the electric component of the optical fields, $(E_1^{(\omega_2)}\hat{\epsilon}_1 + E_2^{(\omega_2)}\hat{\epsilon}_2)$ and $(E_1^{(\omega_1)}\hat{\epsilon}_1 + E_2^{(\omega_1)}\hat{\epsilon}_2)$ respectively. Collecting the spacial and temporal exponential terms of eq. 2.4 expresses the equation in a form where the time average and spacial effects of optical poling can be investigated individually:

$$E^{(\omega_2)*} \otimes E^{(\omega_1)} \otimes E^{(\omega_1)} = \vec{A}^* \otimes \vec{B} \otimes \vec{B}\ e^{i(2\vec{k}_{\omega_1}-\vec{k}_{\omega_2})\cdot\vec{r}} e^{i(\omega_2-2\omega_1)t}. \tag{2.5}$$

The first condition that must be met in order for the combination of laser beams impinging on the sample to have a net effect is that the time average of the write field tensor (eq. 2.3) must be non-zero.[37, 36, 7, 8] Only the second exponential in eq. 2.5 concerns time. Recalling Euler's relations for $e^{i\alpha}$ and that it is the real part of eq. 2.5 that makes up the actual electric component of the optical field, the temporal contribution to optical poling is,

$$\langle E^{\omega_2 *} \otimes E^{\omega_1} \otimes E^{\omega_1} \rangle_t \propto cos\,[(\,\omega_2 - 2\omega_1\,)t]\,. \tag{2.6}$$

The time average of eq. 2.6 is zero except when $\omega_2 = 2\omega_1$, as the case here (see Fig. 2.4).

Each of the optical electric fields of eq. 2.3 interacting with the sample are vectors of the type of eq. 2.2, *i.e.,* first rank tensors with J = 1. Coupling three first rank J = 1 tensors together results in the formation of a third rank tensor with J = 0,1,2, and 3 spherical components. The presence of J = 3 components in the interference pattern created by the vectorial optical fields can interact with the J = 3 components of the nonlinear response of the sample. For example, a D_{3h} molecule, such as that seen in Figure 2.1, does not possess a permanent J = 1 dipole moment vector. The absence of a J = 1 component of the optical response precludes the use of a J = 1 dc electric field to achieve alignment of the molecules. These D_{3h} molecules do, however, possess J = 3 octupolar components in their nonlinear responses. The presence of J = 3 response components in the molecule allows for an interaction with the J = 3 components of the interference pattern created through interaction of the three J = 1 components of the optical fields.

To understand how the interference of two incident optical fields can induce a hyperpolarizability in a bulk sample, consider how the spacial dependence of the incoming optical fields is modulated,

$$\left(E^{2\omega *} \otimes E^{\omega} \otimes E^{\omega}\right)_{\text{spacial}} \propto cos\,[(\,2\vec{k}_{\omega} - \vec{k}_{2\omega}\,)\cdot\vec{r}]\,. \tag{2.7}$$

This is obtained following the same procedure used in eq. 2.6 and using the knowledge that $\omega_2 = 2\omega_1$. As an example of how the vector portions of eq. 2.2 couple, we will consider the example of a simple planar molecule oriented such that it lies in the xy plane with the $\hat{x}$ axis being an axis of two-fold symmetry, and such that the molecule possesses only β_{xxx} and β_{xyy} response components (similar to an example provided by Zyss and Ledoux in ref. [8]). For this example, the J = 1 and J = 3 irreducible tensorial spaces are spanned by $\frac{3}{4}\vec{X} \otimes \left(\vec{X} \otimes \vec{X} + \vec{Y} \otimes \vec{Y}\right)$ and $\frac{1}{4}\vec{X} \otimes \left(\vec{X} \otimes \vec{X} - 3\vec{Y} \otimes \vec{Y}\right)$, respectively, where $\vec{X}$ and $\vec{Y}$ are vectors in the x and y directions. We will first consider circularly polarized light with both $E^{2\omega}$ and E^{ω} having the same handedness, for example, right-handed polarization. If we take the vector portion of eq. 2.2 to be $\vec{E} = E\left(\vec{X} + i\vec{Y}\right)$, then the product eq. 2.3 becomes

$$\left\langle E^{2\omega *} \otimes E^{\omega} \otimes E^{\omega} \right\rangle_{J=1} = E^{2\omega} \left(E^{\omega}\right)^2 \vec{X} \otimes \left(\vec{X} \otimes \vec{X} + \vec{Y} \otimes \vec{Y}\right), \tag{2.8}$$

which has the same form as the J = 1 irreducible component of the hyperpolarizability.

Consider instead, two incoming circularly polarized beams with opposite handedness, for example, $\vec{E}^{(2\omega)} = E^{(2\omega)}\left(\vec{X} - i\vec{Y}\right)$ and $\vec{E}^{(\omega)} = E^{(\omega)}\left(\vec{X} + i\vec{Y}\right)$. Eq. 2.3 now becomes

$$\left\langle E^{2\omega *} \otimes E^{\omega} \otimes E^{\omega} \right\rangle_{J=3} = E^{2\omega} \left(E^{\omega}\right)^2 \vec{X} \otimes \left(\vec{X} \otimes \vec{X} - 3\vec{Y} \otimes \vec{Y}\right), \tag{2.9}$$

which has the same form as the J = 3 irreducible component of the hyperpolarizability. This simple example illustrates the use of an interference pattern of two incident optical fields in creating the irreducible tensor components of the hyperpolarizability.

Chapter 3

Generalization of the internal potential model to multi-polar nonlinear optical chromophores

Work done in collaboration with Professor Joseph Zyss
Ecole Normale Supérieure de Cachan, Cachan, France

3.1 Introduction

There are two main aspects to the design of organic materials for second-order nonlinear optical applications. The first is the design of the nonlinear optical chromophore. The second is the construction of a macroscopic sample in which these chromophores are arranged in a non-centrosymmetric manner. Construction of a chromophore typically starts with a centrosymmetric conjugated molecule such as benzene, stilbene, or a polyene. The symmetry is then broken by attaching electron donor and acceptor substituents. In most cases, this substitution induces a substantial permanent dipole in the molecule. An advantage of this dipole moment is that it allows macroscopic alignment to be induced via an external electric field,

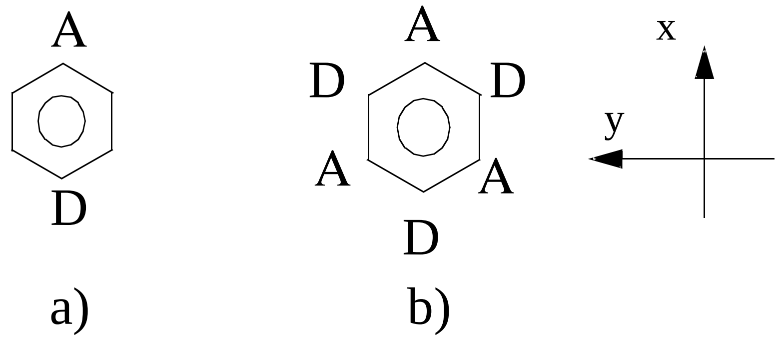

Figure 3.1: Dipolar and octupolar substitution patterns for benzene. A and D represent electron and donor substituents, respectively.

as in corona poling.[35] However, the macroscopic polarization of the resulting material leads to long-term stability issues.[8] A number of approaches are being used to address these stability issues, including cross-linking of a host polymer and the attachment of the chromophore as a side chain to the host polymer. An alternative is to create an acceptor-donor substitution pattern, such as the octupolar substituted benzene shown in Figure 3.1(b). This type of octupolar substitution pattern does not induce a permanent dipole moment in the molecule, but it does lead to a substantial hyperpolarizability.[7, 8] Although the lack of a dipole moment precludes corona polling, optical polling techniques can be used to achieve macroscopic alignments.[7, 8] Indeed, optical poling may have advantages for the construction of novel materials in which the optical susceptibilities are modulated with micron resolution. Construction of such materials is an interesting design problem since both the linear and nonlinear susceptibilities may be modulated and these modulation patterns may be intimately coupled. In designing chromophores for this new class of materials, we can take advantage of the flexibility afforded by the large number of available electron donor and acceptor substituents, the number of substitution sites on a chromophore such as benzene or stilbene where these may be placed, and the wealth of possibilities opened up with two and three dimensional substitution patterns. To take full advantage of this flexibility, it is useful to understand the structure/property relationships and here these are explored using semi-empirical quantum chemistry.

In constructing a model for the structure/property relationships, it is useful to be able to continuously vary the strength of the electron acceptors and donors. Two general schemes are currently in use. In one scheme, the acceptors and donors are viewed as applying an internal electric field to the central conjugated unit. This scheme was recently used to provide a unified description of the linear and nonlinear susceptibilities of push-pull polyene systems.[10] This unification was achieved by writing the energy, W, of an unsubstituted polyene in an electric field as

$$W = -\alpha\left(E\right)E^2 = -\alpha\left(0\right)E^2 + \beta\left(0\right)E^3 + \gamma\left(0\right)E^4, \tag{3.1}$$

where $\alpha(E)$ is used to indicate that the polarizability is a function of the applied electric field. It follows that,

$$\beta\left(E\right) = -\left.\frac{\partial\alpha\left(E'\right)}{\partial E'}\right|_{E'=E} \quad ; \quad \gamma\left(E\right) = \left.\frac{\partial\beta\left(E'\right)}{\partial E'}\right|_{E'=E}. \tag{3.2}$$

Marder treated the acceptor and donor of a push-pull polyene system as applying an internal electric field to the central polyene, with the solvent serving to reinforce this internal field.[10] The linear and nonlinear susceptibilities where then shown to obey eq. (3.2), with E being the internal electric field.

The second scheme commonly used to continuously vary the strength of electron acceptors and donors is to view the acceptor or donor as perturbing the energy of the carbon atom to which it is attached.[39] This second scheme is more convenient for the current study. In push-pull polyenes, the optical susceptibilities lie primarily along the long axis and thus, the one dimensional approximation of eq. 3.1 is sufficient. For the substituted benzenes under consideration here, or other multidimensional substitution pattern, the susceptibilities are not dominated by any one tensor component. While it may be possible to use an internal electric field scheme to study these various tensor components, the second scheme is more convenient since it allows us to easily consider substitution effects at each of the benzenoid carbons.

Despite the complexity introduced by the large number of tensor components in the second hyperpolarizability, a rather simple picture emerges in the limit where the hyperpolarizability is linearly dependent on the strength of the acceptors and donors. In the formalism of eqs. 3.1 and 3.2, this linear regime may be viewed as that range of internal electric field F_l where

$$\beta_{ijk} = \gamma_{ijkl} F_l. \tag{3.3}$$

We begin by characterizing this linear regime within the Hückel, Pariser-Parr-Pople (PPP) and intermediate neglect of differential overlap (INDO) quantum chemical descriptions. INDO calculations performed on a variety of chromophores are then used to determine how close these chromophores are to the linear regime of eq. 3.3. We then discuss the extension to nonlinear effects and summarize the results.

3.2 Internal Potential Model

The model developed here extends the one-dimensional scalar-like internal field model of Oudar to multipolar systems.[22] In extending the model, we continue to view the molecule as a skeleton to which electron-acceptor/electron-donor substituents have been attached. These substituents exert an effective potential on the skeleton which we will refer to as the internal potential. This internal potential perturbs the skeleton and accounts for the hyperpolarizability of the total, or "dressed", system. For instance, if we assume the system to be essentially one-dimensional, as in Oudar's restricted approach, then the internal potential can be viewed as the source of an internal electric field applied along the x axis, F_x. Under later illumination, the skeleton experiences both this internal field, F_x, and the external electric field of the laser, E_x, such that the total field applied to the skeleton is

$$F_x^{(tot)} = F_x + E_x \tag{3.4}$$

The energy, W, of the skeleton in the total field of eq. 3.4 is given by,

$$W = W_0 - \mu_x F_x^{(tot)} - \frac{1}{2}\alpha_{xx} F_x^{(tot)^2} - \frac{1}{3}\beta_{xxx} F_x^{(tot)^3} - \frac{1}{4}\gamma_{xxxx} F_x^{(tot)^4} \tag{3.5}$$

where W_0 is the energy of the skeleton in zero field, and μ, α, β and γ are the susceptibilities of the skeleton. In eqs. 3.6-3.9, we assume a centrosymmetric skeleton, such that μ and β of the skeleton are both zero. The susceptibilities of the dressed system may be obtained by substituting eq. 3.4 into eq. 3.5,

$$\bar{W} = \bar{W}_0 - \bar{\mu}_x E_x - \frac{1}{2}\bar{\alpha}_{xx}{E_x}^2 - \frac{1}{3}\bar{\beta}_{xxx}{E_x}^3 - \frac{1}{4}\bar{\gamma}_{xxxx}{E_x}^4 \tag{3.6}$$

$$\bar{\alpha}_{xx} = \alpha_{xx}; \bar{\gamma}_{xxxx} = \gamma_{xxxx} \tag{3.7}$$

$$\bar{\mu}_x = \alpha_{xx} F_x \tag{3.8}$$

$$\bar{\beta}_{xxx} = 3\gamma_{xxxx} F_x \tag{3.9}$$

(Throughout this paper, we will use a bar to denote properties of the dressed system, as compared to those of the skeleton.) We also ignore terms that are higher than linear order in F_x. This assumption of linear response with respect to the internal potential is discussed in more detail below.

Note that according to eqs. 3.8 and 3.9, even rank tensors $\bar{\alpha}$ and $\bar{\gamma}$ are unchanged at first order in F_x. The odd-rank tensors $\bar{\mu}$ and $\bar{\beta}$ are both proportional to the internal field, F_x, with proportionality constants that depend only on properties of the skeleton. This model therefore predicts that the ratio $\bar{\beta}/\bar{\mu}$ will be the same for all chemical substitutions of a given skeleton. Furthermore, this ratio can be derived from the susceptibilities, α and γ, of the skeleton.

In order to generalize this model so as to allow for the description of multipolar systems, we must take into account the full tensor character of both the internal potential and the resulting hyperpolarizability. While we will retain the view that the substituents apply an electrostatic potential to the skeleton, we will use a more general expanded form for the internal potential,

$$\Phi(r, \theta, \phi) = \sum_{j=0}^{\infty} \sum_{m=-j}^{j} V_m^j r^j Y_m^j(\theta, \phi) \tag{3.10}$$

(See Appendix 3.9.1) The $j = 1$ terms of eq. 3.10 are equivalent to application of a uniform electric field to the skeleton, with the coefficients, V_m^j, being the electric field expressed in spherical tensor notation. Although the $j = 1$ term is sufficient for the one-dimensional model summarized above, multipolar systems require terms with $j \neq 1$, which can not be modeled as an internal electric field. Consider, for instance, the octupolar substitution pattern of Figure 3.1, which applies an internal potential corresponding to j=3.

In eq. 3.5, the energy of the skeleton is expanded as a power series in the total field. This may be generalized to the internal-potential model by expanding the energy as a power series in the coefficients, V_m^j, of eq. 3.10.

$$\begin{aligned} W &= W_0 - \sum_{j,m} \chi_m^j V_m^j - \frac{1}{2} \sum_{j,j',m,m'} \chi_{m,m'}^{j,j'} V_m^j V_{m'}^{j'} \\ &\quad - \frac{1}{3} \sum_{\substack{j,j',m,m' \\ j'',m''}} \chi_{m,m',m''}^{j,j',j''} V_m^j V_{m'}^{j'} V_{m''}^{j''} \\ &\quad - \frac{1}{4} \sum_{\substack{j,j',m,m' \\ j'',j''',m'',m'''}} \chi_{m,m',m'',m'''}^{j,j',j'',j'''} V_m^j V_{m'}^{j'} V_{m''}^{j''} V_{m'''}^{j'''} \end{aligned} \tag{3.11}$$

where the χ's are generalized susceptibilities of the skeleton. Those terms of eq. 3.11 for which all j's are equal to 1 are equivalent to the expansion of eq. 3.5, with the susceptibilities transformed from Cartesian to spherical tensor notation. For multipolar systems, the internal potential has components with $j \neq 1$, and this introduces generalized susceptibilities which do not occur when the energy is expanded in the presence of an electric field. The χ's may be defined in terms of energy derivatives, for example,

$$\chi_{m,m',m'',m'''}^{j,j',j'',j'''} = \frac{1}{3!} \frac{\partial^4 W}{\partial V_m^j \partial V_{m'}^{j'} \partial V_{m''}^{j''} \partial V_{m'''}^{j'''}} \tag{3.12}$$

By analogy to eq. 3.4, the potential experienced by the skeleton is a sum of the external potential due to the laser, $(V_m^j)^{ext}$, and the internal potential due to the chemical substituents, $(V_m^j)^{int}$

$$V_m^j = \left(V_m^j\right)^{ext} + \left(V_m^j\right)^{int} \tag{3.13}$$

As with eq. 3.6, the susceptibilities of the dressed system may be obtained by substituting eq. 3.13 into eq. 3.11, and extracting the coefficient of the appropriate powers of $(V_m^j)^{ext}$. Terms that are linear in the external potential give the permanent electrostatic moments of the dressed system. For instance, the coefficients of $(V_m^1)^{ext}$, $(V_m^2)^{ext}$ and $(V_m^3)^{ext}$ yield the permanent dipole, quadrupole and octupole moments of the dressed system. Similarly, the susceptibilities with respect to an applied electric field are obtained from the coefficients of the appropriate powers of $(V_m^1)^{ext}$. Just as in the one dimensional model of eq. 3.6, we retain only up to linear terms with respect to the internal potential. This thereby provides a recipe for relating the properties of the dressed system to those of the skeleton and the internal potential. For example, to obtain the first hyperpolarizability, which is related to $\bar{\chi}^{1,1,1}_{m,m',m''}$, we extract the coefficient of $\left((V^1_m)^{ext}\right)^3$ and retain up to linear terms in $(V^j_m)^{int}$

$$\bar{\chi}^{1,1,1}_{m,m',m''} = \chi^{1,1,1}_{m,m',m''} + \frac{3!}{2!}\sum_{j,m'''} \chi^{1,1,1,j}_{m,m',m'',m'''} \left(V^j_{m'''}\right)^{int} \tag{3.14}$$

This is a generalization of eq. 3.9 that allows for both a multipolar internal potential and includes all tensor components of the susceptibility. Eq. 3.14 may also be written as

$$\bar{\chi}^{1,1,1}_{m,m',m''} = \chi^{1,1,1}_{m,m',m''} + \sum_{j,m'''} \frac{\partial \chi^{1,1,1}_{m,m',m''}}{\partial \left(V^j_{m'''}\right)^{int}} \left(V^j_{m'''}\right)^{int}. \tag{3.15}$$

In analogy to eq. 3.6, where γ is the derivative of β with respect to the field, the derivative in eq. 3.15 is related to γ if $j = 1$ and to a generalized susceptibility if $j \neq 1$.

Equations 3.11 through 3.15 represent a formal generalization of the internal potential model to multipolar systems, providing a means for obtaining the properties of the dressed system from the properties of the skeleton and the internal potential. However, due to the large number of tensor components in both the internal potential and the generalized susceptibilities, it is useful to develop a systematic means, readily connected to symmetry reductions, to summarize the relevant relationships for particular skeletons.

A convenient representation of the internal potential is obtained by recognizing that the molecular energy is most sensitive to the value of the potential at the atoms. Indeed, for the quantum chemical models used in section 3.3, the Hamiltonian contains only the value of the potential at the atomic sites. The internal potential for the benzene skeleton can then be represented by its value at each of the six carbon atoms. These six degrees of freedom may be arranged in vector form,

$$\mathbf{V} = (V^{int}_1, V^{int}_2, V^{int}_3, V^{int}_4, V^{int}_5, V^{int}_6), \tag{3.16}$$

where V_i^{int} is the the value of the potential at the i^{th} site. Since, in relating the properties of the dressed system to those of the skeleton, we retain only up to linear terms with respect to the internal potential, it is convenient to rewrite eq. 3.15 in a manner that emphasizes this linear relationship. This may be done by arranging the tensor components of the susceptibility into a column vector. For instance, the 27 tensor components of the first hyperpolarizability may be arranged into a vector β. Equation 3.15 may then be written,

$$\bar{\beta} = \beta + \mathbf{L}\mathbf{V}, \tag{3.17}$$

where $\mathbf{L}$ is a matrix with elements defined as,

$$L_{i,j} = \frac{\partial \beta_i}{\partial V_j^{int}}. \tag{3.18}$$

Equation 3.17 provides a linear relationship between the susceptibility of the dressed system and the internal potential. The linear response matrix, $\mathbf{L}$, is a function only of the skeleton, and completely specifies the linear response of the molecule. Below, we use quantum chemistry to calculate the matrix $\mathbf{L}$. For the benzene skeleton, $\mathbf{L}$ is a large 27 by 6 matrix and we will consider two ways to extract the relevant information. The first is an analysis based on the molecular symmetry of the skeleton. The second is singular value decomposition (SVD), a numerical approach that summarizes the information contained in $\mathbf{L}$.

3.3 Quantum Chemical Calculations

The linear response matrix, $\mathbf{L}$ of eq. 3.17, will be calculated using three quantum chemical models, Hückel theory, PPP (Pariser-Parr-Pople) theory, and INDO (Intermediate Neglect of Differential Overlap) theory. In all three models, the benzene molecule is taken to lie in the (x,y) plane with D_{6h} symmetry and bond lengths of 1.41Å and 1.10Å for the C-C and C-H bonds, respectively.

Both the Hückel and PPP models consider only the π electrons. The form of the π-electron Hamiltonian is,

$$H_{benzene} \;=\; \sum_{\mu} \epsilon_\mu n_\mu + \sum_{\mu \neq \nu, \sigma} t_{\mu,\nu} a^\dagger_{\mu\sigma} a_{\nu\sigma} + \sum_{\mu,\nu,\sigma} a^\dagger_{\mu\sigma} a_{\nu\sigma} \frac{\gamma_{\mu,\mu}}{2} n_\mu \left(n_\mu - 1\right)$$

$$+ \sum_{\mu \neq \nu} \frac{\gamma_{\mu,\nu}}{2} \left(n_\mu - 1\right)\left(n_\nu - 1\right), \tag{3.19}$$

where $a^\dagger_{\mu\sigma}(a_{\mu\sigma})$ creates (destroys) an electron with spin σ in the p_z orbital on the μ^{th} carbon atom, $n_\mu = \sum_\sigma a^\dagger_{\mu\sigma} a_{\mu\sigma}$ is the number operator for electrons on carbon μ, ϵ_μ is the on-site energy, and the sums are over the six carbon atoms of benzene. Transfer matrix elements, $t_{\mu\nu}$, are included only between adjacent carbon atoms.

Hückel theory ignores Coulomb interactions between electrons and so includes only the first two terms of eq. 3.19. The hyperpolarizability predicted by Hückel theory depends only on the molecular structure and the transfer integral, $t_{\mu,\nu}$, between adjacent carbons. Since the results will be compared to those of INDO theory, and the hyperpolarizability is sensitive to the energy of the lowest excited state, the Hückel transfer integral is set to -2.65eV. Using this value, the lowest optically allowed state obtained from Hückel theory agrees with that of INDO theory.

PPP theory includes Coulomb interactions between electrons via the last two terms of eq. 3.19. The calculations presented here use the Ohno parameterization for the electron-electron potential,

$$\gamma_{\mu,\nu}[eV] = \frac{14.397}{\sqrt{\left(\frac{14.397}{11.26}\right)^2 + \left(r_{\mu\nu}[\mathring{A}]\right)^2}}. \tag{3.20}$$

The ground electronic state is obtained from Hartree-Fock theory, and the excited states are obtained from singles-configuration interaction (S-CI) theory. The S-CI calculations include all molecular orbitals. The transfer matrix element, $t_{\mu\nu}$, between adjacent carbons is set to -2.52eV, such that the lowest optically allowed state agrees with that obtained from INDO theory.

INDO theory includes both σ and π electrons and includes Coulomb interactions between electrons. Unlike the above two models, the INDO model has been parameterized such that the Hamiltonian may be obtained for any organic molecular structure[27]. The electronic states are obtained in the same manner as for PPP theory. Hartree-Fock theory is used for the ground state and S-CI theory with a complete set of molecular orbitals is used for the excited states. Since INDO is parameterized for arbitrary organic structures, we also use INDO theory for the calculations on the substituted benzene molecules presented below.

The linear response matrix, **L** of eq. 3.18, is obtained by adding the internal potential of eq. 3.16 to the Hamiltonian,

$$H = H_{benzene} + \sum_{\mu} V_{\mu}^{int} n_{\mu} \tag{3.21}$$

For Hückel and PPP theory, n_{μ} is the number operator for the p-orbital on the μ^{th} carbon atom. For INDO theory, we consider two possibilities for the number operator. The first is to use the number operator for just the p-orbital on the μ^{th} carbon, which is consistent with the orbital perturbation argument in Appendix 3.9.1. The second choice is to use the number operator for the total number of valence electrons on the μ^{th} carbon, which corresponds to placing the entire atom in an electrostatic potential with value V_{μ}^{int}.

The hyperpolarizability, in Cartesian coordinates, is calculated using a sum over states expression

$$\beta_{ijk} = \frac{1}{2} \sum_{\wp} \sum_{m,n \neq 0} \frac{\langle 0|\, \mu_i \,|n\rangle \langle n|\, \Delta\mu_j \,|m\rangle \langle m|\, \mu_k \,|0\rangle}{E_{0n} E_{0m}}, \tag{3.22}$$

where $|0\rangle$ is the Hartree-Fock ground state, $|m\rangle$ and $|n\rangle$ are S-CI excited states, $\Delta\mu_j = \mu_j - \langle 0\, |\mu_j|\, 0\rangle$, E_{0m} is the difference in energy between the ground and excited states, and $\wp$ is a summation over all six permutations of the tensor indices. Eq. 3.22 is first evaluated in atomic units (energy in Hartrees, charge in units of e, and length in Bohr radii), and then multiplied by $8.6392 * 10^{-33}$ to convert to esu[11].

It is convenient to transform the Cartesian tensor of eq. 3.22 to a spherical tensor representation. This is done via Clebsch-Gordon coefficients, as discussed in reference [40]. The norm of β is taken as,

$$\left|\beta^J\right| = \sqrt{\sum_{M} \left(\beta_M^J\right)\left(\beta_{-M}^J\right)} \;\; ; \;\; |\beta| = \sqrt{\sum_{J,M} \left(\beta_M^J\right)\left(\beta_{-M}^J\right)} \tag{3.23}$$

where the sum is over all J and M. Due to Kleinmann symmetry [7, 8] in the non-resonant response, only the $J = 1$ and $J = 3$ components are non-zero.

The linear response matrix, **L**, is obtained by numerical evaluation of the derivative in eq. 3.18, using central differencing with a step size of 0.001eV. The central difference is evaluated for each of the internal potential values, V_j^{int} of eq. 3.16. For example, the derivative of the hyperpolarizability with respect to the first component of eq. 3.16 is,

$$\frac{\partial\beta}{\partial V_1^{int}} = \frac{\beta(V_1^{int}=h) - \beta(V_1^{int}=-h)}{2h}, \tag{3.24}$$

where h is the step size and $\beta(V_1^{int}=h)$ is the first hyperpolarizability evaluated with an internal potential of magnitude h applied to site 1.

3.4 Symmetry Analysis

The quantum chemical methods described above yield a 27x6 linear response matrix, **L** of eq. 3.17. The first approach we will use to extract information from **L** is based on the molecular symmetry of the skeleton. In this approach, the tensors β and **V** are decomposed into components that transform as irreducible representations of the D_{6h} point group of the benzene skeleton. For substituted benzenes, β of the skeleton is zero and eq. 3.17 becomes

$$\bar{\beta} = \mathbf{LV}. \tag{3.25}$$

Since **L** is a property of the molecular skeleton, it transforms as the totally symmetric representation, A_{1g}. The product **LV** then transforms according to the symmetry properties of **V**, since $A_{1g} \otimes \Gamma = \Gamma$ for any symmetry representation Γ. Thus application of an internal potential that transforms as symmetry representation Γ induces a hyperpolarizability that also transforms as Γ.

To create symmetry-adapted forms of the hyperpolarizability tensor, we first define a projection operator P^Γ that, when applied to a function, retains only that component of the function that transforms as the symmetry species Γ. In other words, P is the projection operator from the unrestricted tensor onto the irreducible subset Γ. It is convenient to work with spherical tensors, $\bar{\beta}_M^J$, such that the transformation properties of $\bar{\beta}_M^J$ are identical to those of the spherical harmonic Y_M^J. The projection operator P^Γ is defined by its action on $\bar{\beta}_M^J$ as,

$$P^\Gamma \bar{\beta}_M^J = \left(\frac{d^\Gamma}{h}\right) \sum_R \chi^\Gamma(R)(-1)^{inv*J} \sum_N D_{M,N}(R)\bar{\beta}_N^J \tag{3.26}$$

Table 3.1: Symmetry-adapted hyperpolarizability tensors and internal potentials for the D_{6h} point group of benzene. The notation $\{\bar{\beta}^3_1, \bar{\beta}^3_{-1}\}$ indicates that any linear combination of β^3_1 and β^3_{-1} will transform with the indicated symmetry. The internal potentials are given as a normalized vector representing the value of the potential on each of the six carbon atoms in benzene, **V** of eq. (3.16).

	Hyperpolarizabilities	
Symmetry	J = 3	J = 1
A_{2u}	$\bar{\beta}^3_0$	$\bar{\beta}^1_0$
B_{1u}	$\bar{\beta}^3_3 + \bar{\beta}^3_{-3}$	
B_{2u}	$\bar{\beta}^3_{-3} - \bar{\beta}^3_3$	
E_{1u}	$\{\bar{\beta}^3_1, \bar{\beta}^3_{-1}\}$	$\{\bar{\beta}^1_1, \bar{\beta}^1_{-1}\}$
E_{2u}	$\{\bar{\beta}^3_2, \bar{\beta}^3_{-2}\}$	
	Internal Potentials	
B_{1u}	$\frac{1}{\sqrt{6}}[1, -1, 1, -1, 1, -1]$	
$E^{(a)}_{1u}$	$\frac{1}{\sqrt{12}}[2, 1, -1, -2, -1, 1]$	
$E^{(b)}_{1u}$	$\frac{1}{\sqrt{4}}[0, 1, 1, 0, -1, -1]$	
E_{2g}	$\frac{1}{\sqrt{12}}[2, -1, -1, 2, -1, -1]$	
E_{2g}	$\frac{1}{\sqrt{4}}[0, 1, -1, 0, 1, -1]$	
A_{1g}	$\frac{1}{\sqrt{6}}[1, 1, 1, 1, 1, 1]$	

where h is the order of the group, d is the degeneracy of the symmetry species Γ, R labels the symmetry operations of the point group, χ is the character for operation R in symmetry species Γ, D(R) is the rotation matrix associated with the operation R[41], and *inv* is 1 if R involves an inversion and zero otherwise. By applying the projection operator to each of the components, $\bar{\beta}^J_M$, we can determine all linear combinations of the $\bar{\beta}^J_M$ that transform as species Γ. The results are listed in Table 3.1. A similar procedure yields the symmetry-adapted internal potentials of Table 3.1.

As was discussed above, since **L** of eq. 3.25 transforms as the totally symmetric representation, A_{1g}, an acceptor-donor substitution pattern that causes the skeleton to experience an internal potential of symmetry Γ, within the linear response approximation, induces a hyperpolarizability of symmetry Γ in the dressed system. For example, an internal potential with B_{1u} symmetry, corresponding to the octupolar substitution pattern of Figure 3.1, will induce a hyperpolarizability response of B_{1u} symmetry, $\bar{\beta}^3_3 + \bar{\beta}^3_{-3}$. Comparison of the symmetry adapted internal potentials and hyperpolarizabilities reveals some general features. In Table 3.1 only the B_{1u} and E_{1u}

representations are present in both the symmetry-adapted hyperpolarizabilities and internal potentials. Although it is possible to form hyperpolarizabilities that transform as A_{2u}, B_{2u}, and E_{2u}, these will not arise from a linear response with respect to an internal potential applied to the carbon atoms of benzene. Similarly, the absence of g-symmetry hyperpolarizability tensors in Table 3.1 indicates that application of the g-symmetry internal potentials, A_{1g} and E_{2g}, will not induce a hyperpolarizability. This is as expected, since application of a g-symmetry internal potential does not remove the center of symmetry.

3.5 Singular Value Decomposition

The symmetry analysis of the previous section reveals characteristic directions associated with the linear response matrix, **L**. Another approach to extract information from the linear response matrix, **L**, is via singular value decomposition (SVD). SVD is essentially the diagonalization of a rectangular matrix and decomposes the 27x6 matrix, **L** into a product of three matrices

$$\mathbf{L} = \mathbf{U}\mathbf{T}\mathbf{W}^{\dagger} \tag{3.27}$$

where **U** and $\mathbf{W}^{\dagger}$ are unitary matrices with sizes 27x27 and 6x6 respectively. **T** is a 27x6 matrix that is zero except for the upper-left corner which contains a diagonal 6x6 matrix. Eq. (3.17) may be rewritten in terms of the output of the SVD factorization as,

$$\bar{\beta} = \beta + \mathbf{U}\mathbf{T}\mathbf{W}^{\dagger}\mathbf{V}. \tag{3.28}$$

Eq. (3.28) can be interpreted as follows. The rows of $\mathbf{W}^{\dagger}$ give characteristic directions for the internal potential. A general internal potential **V** can be written as a linear combination of these characteristic directions. This is accomplished by the matrix multiplication, $\mathbf{W}^{\dagger}\mathbf{V}$, which returns a vector containing the projection of **V** onto the characteristic directions. The elements of the diagonal matrix **T** give the magnitude of the hyperpolarizability induced by an internal potential of unit magnitude applied along each of these characteristic directions. Finally, in the multiplication by **U**, the columns of $\mathbf{U}$ give the distribution of the response among the various tensor components. In particular, application of an internal potential with a form equal to the i^{th} row of $\mathbf{W}^\dagger$ induces a hyperpolarizability with norm $T_{i,i}$ and hyperpolarizability components given by the i^{th} column of $\mathbf{U}$.

For the benzene skeleton, the characteristic directions for the internal potential are determined by symmetry, and the rows of $\mathbf{W}$ are identical to the symmetrized internal potentials of Table 3.1. The columns of $\mathbf{U}$ indicate that application of a B$_{1u}$ potential induces a hyperpolarizability of form $\bar{\beta}^3_3 + \bar{\beta}^3_{-3}$, just as in Table 3.1. For an E$_{1u}$ internal potential, the columns of $\mathbf{U}$ indicate that $\bar{\beta}^3_1 = -\bar{\beta}^{3*}_{-1}$ and $\bar{\beta}^1_1 = -\bar{\beta}^{1*}_{-1}$. Note that B$_{1u}$ potentials induce $m = 3$ components, while E$_{1u}$ potentials induce $m = 1$ components.

Table 3.2 shows the magnitude of the hyperpolarizabilities induced by B$_{1u}$ and E$_{1u}$ potentials, as given by the diagonal elements of $\mathbf{T}$ in eq. 3.28. The three quantum chemical models are shown in order of increasing complexity. As we go from Hückel to PPP theory, we stay within a π electron model but add Coulomb interactions between electrons. Addition of these Coulomb interactions reduces the B$_{1u}$ response by 66% and the E_{1u} response by 92%. The ratio of the B$_{1u}$ to E$_{1u}$ response is then raised from 3 in Hückel theory to 12 in PPP theory. In going to INDO theory, we include the σ bonding network as well as the π electrons. As discussed in Section 3.3, there are two ways to apply an internal potential within INDO theory. The first is to apply the potential to the π orbitals only. For this case, the only difference between the INDO and PPP models is the explicit inclusion of the sigma electrons. This reduces the B$_{1u}$ response by about 30% and the E_{1u} response by only 3%, thereby lowering the B_{1u} to E_{1u} ratio to about 7. Finally, Table 3.2 shows the results when the internal potential is applied to both the σ and π electrons of the INDO model. Relative to the π electron potential, the B$_{1u}$ and E_{1u} responses are lowered by 40% and 15%, thereby lowering the B_{1u} to E_{1u} ratio to about 5. Since the INDO model is the most complete, we take the range 5 to 7 as a reasonable quantum chemical estimate of the B_{1u} to E_{1u} ratio.

Table 3.2: Results of the SVD analysis on the benzene skeleton, using the quantum chemical models discussed in Section 3.3. The values give the magnitude of the hyperpolarizability (in esu's) induced by an internal potential of unit magnitude (in volts), along each of the symmetry directions in Table 3.1. For the INDO model, results are shown with the internal potential applied to the entire atom and to the just the π orbitals.

Hyperpolarizability Magnitudes, from the matrix **T**		
Hamiltonian	B_{1u}	E_{1u}
Hückel	4.38	1.79
PPP, S-CI	1.47	0.148
INDO, S-CI,π orbitals only	1.02	0.143
INDO, S-CI, entire atom	0.615	0.121

3.6 Nonlinearity Within the Internal Field Model

Both the symmetry and SVD analyses assume linear response, such that the optical susceptibilities and other properties of the dressed system are linearly related to the internal potential (eqs. 3.25 and 3.28). In this section, we stay within the internal potential model, but consider breakdown in the linear response approximation. This is done by examining the hyperpolarizability as a function of the strength of the internal potential. The potential is applied along the symmetry-adapted directions of Table 3.1. Note that internal potentials of *gerade* symmetry do not remove the center of symmetry, and so do not induce a hyperpolarizability.

Figure 3.2 shows the norm of the hyperpolarizability induced by internal potentials applied in the B_{1u} symmetry direction. Table 3.1 indicates that the linear response with respect to this internal potential will be of the form $\beta^3_{-3}+\beta^3_{+3}$. This holds also for arbitrary strength internal potentials. (The perturbed system has D_{3h} symmetry, and $\beta^3_{-3}+\beta^3_{+3}$ is the only tensor that transforms as the totally symmetric A_1' representation of the D_{3h} point group.)

The three quantum chemical models yield similar results. For all three models, the response rises to a maximum between approximately 2.5 and 4eV. As expected from the results of the linear response analysis in Table 3.2, the predictions from the Hückel model are substantially larger than that of the PPP or INDO models. The hyperpolarizability in Figure 3.2 increases nearly linearly with internal potential up to

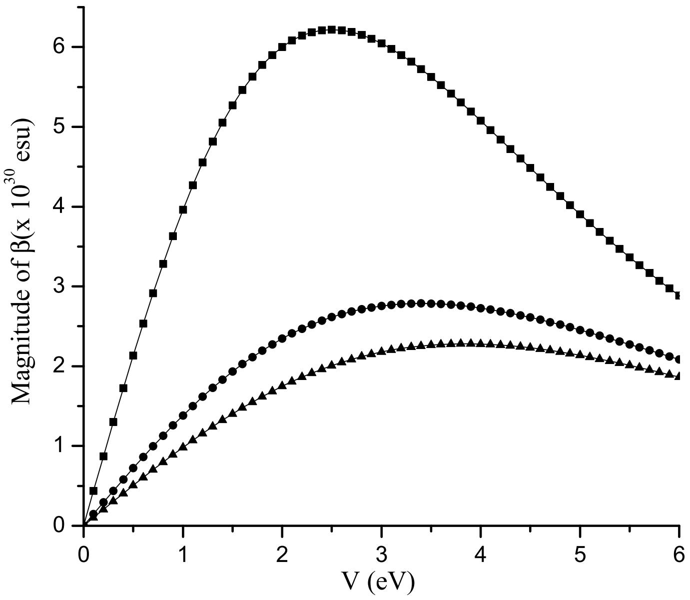

Figure 3.2: Norm of the hyperpolarizability induced by an internal potential of B_{1u} symmetry for the Hückel (squares), PPP (circles), and INDO (triangles) Hamiltonians. V is the root mean square (RMS) magnitude of the potential. For all V, the hyperpolarizability tensor has B_{1u} symmetry, $\beta_3^3 + \beta_{-3}^3$.

about 2eV, corresponding to an internal potential with magnitude 0.8eV alternating from atom to atom according to the internal potential of Table 3.1. This places the validity of the linear response regime at about 0.8eV applied to each atom, or equivalently, a difference of 1.6eV in the potential applied to adjacent carbon atoms.

The existence of a maximum in Figure 3.2 may be rationalized by analogy to a similar behavior seen in push-pull polyenes[20]. In those systems, increasing the strength of the acceptors and donors enhances the change in permanent dipole moment upon excitation to the charge-transfer states, while simultaneously decreasing the transition moments to these states. Since these two factors have opposing effects on the hyperpolarizability, a maximum response is obtained for an intermediate acceptor-donor strength. Although there is no permanent dipole moment for the ground and excited states of a benzene perturbed with a B_{1u} potential, it seems likely the maximum still results from a balance between the amount of charge being displaced on excitation and the transition moment to these charge-displaced states.

The hyperpolarizability induced by an internal potential with E_{1u} symmetry is shown in Figures 3.3 and 3.4. The total magnitude of the response is shown in Figure 3.3. In the linear response analysis of Table 3.2, the hyperpolarizability predicted by Hückel theory is a factor of 12 larger than that of PPP or INDO theory. Figure 3.3 shows that this discrepancy becomes even larger for strong potentials. Apparently, inclusion of electron-electron interactions has a large effect on the predicted hyperpolarizability and so Hückel theory is not adequate for calculations on these systems.

Figure 3.4 shows the various tensor components of the hyperpolarizability induced by an E_{1u} internal potential. The slopes near zero potential are as expected from the linear response results in Table 3.2. For the m = 1 components that are allowed in linear response, $\beta^3_{\pm 1}$ and $\beta^1_{\pm 1}$, the linear regime extends to about 5eV. The dominant nonlinear effect is the appearance of m = 3, $\beta^3_{\pm 3}$, components. Although these are not allowed in linear response, they grow in nonlinearly and become comparable to the other components above about 2eV. At this magnitude, the carbon atoms at opposite sides of the benzene ring differ in potential by up to 2eV.

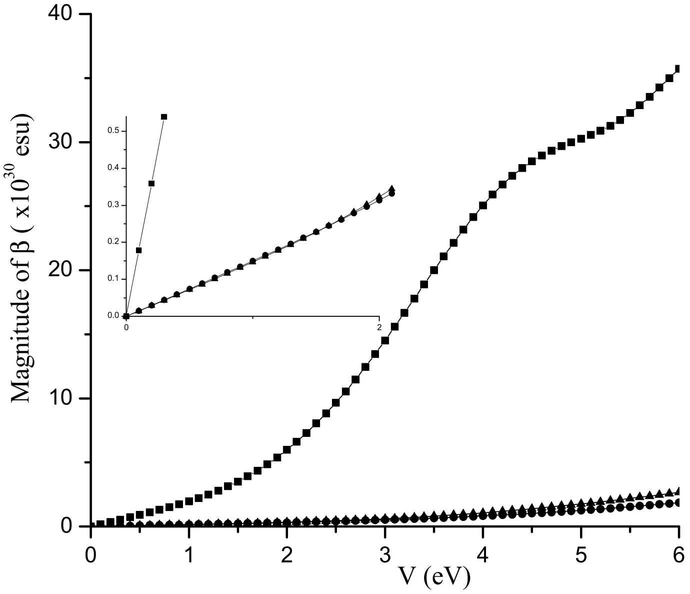

Figure 3.3: Norm of the hyperpolarizability induced by an internal potential of E_{1u} symmetry for the Hückel, PPP, and INDO Hamiltonians. The insert is a detail for small V, showing that the slopes near V=0 agree with the linear response results of Table 3.2. Notation is as in Figure 3.2.

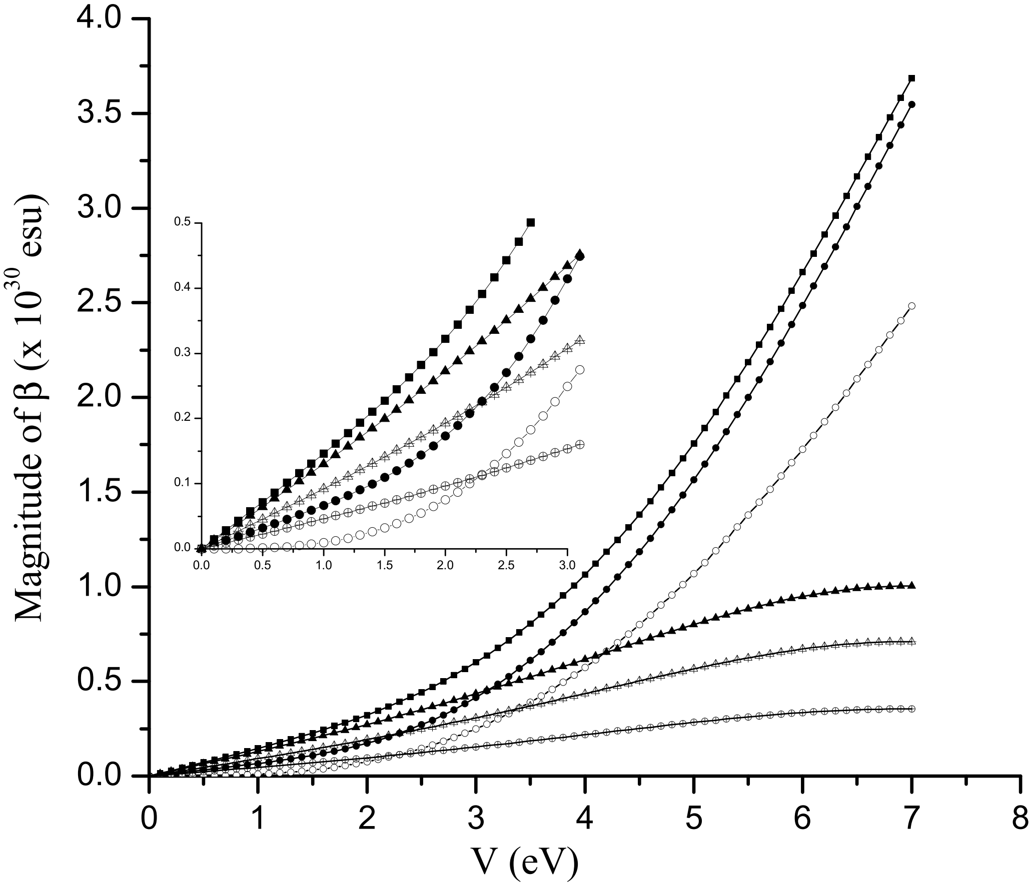

Figure 3.4: Decomposition of the INDO results of Figure 3.3 into its spherical tensor components. The insert is a detail for small V. Note that the $\beta^3_{\pm 3}$ component is zero in the linear response analysis, and here grows in quadratically with V. The filled squares are the total response, filled circles are the total $J = 3$ components, the empty circles are the $J = 3, m = 3$ components, the crossed circles are the $J = 3, m = 1$ components, the filled triangles are the total $J = 1$ components, and the crossed triangles the $J = 1, m = 1$ components.

Table 3.3: Results from INDO calculations on substituted benzene molecules. In the notation for substitution patterns, such as (X, H, H, H, H, H) for monosubstitution, the parenthesis enclose the substituents attached to each of the carbon atoms in order around the ring. The units for the hyperpolarizability are 10^{-30} esu.

Monosubstituted

Substituent	$\lvert\beta\rvert$	$\lvert\beta^{(3)}_{\pm3}\rvert$	$\lvert\beta^{(3)}_{\pm1}\rvert$	$\lvert\beta^{(1)}_{\pm1}\rvert$	$\frac{\lvert\beta^{(1)}_{\pm1}\rvert}{\lvert\beta^{(3)}_{\pm1}\rvert}$	$\frac{\lvert\beta_{(m=3)}\rvert}{\lvert\beta_{(m=1)}\rvert}$
1) X = NO_2	6.55	3.73	1.22	2.45	2.01	1.36
2) X = CN	0.956	0.487	0.209	0.419	2.00	1.34
3) X = F	0.570	0.237	0.146	0.291	1.99	0.728
4) X = CH_3	0.614	0.292	0.178	0.266	1.49	0.912
5) X = OCH_3	1.45	0.653	0.355	0.705	1.99	0.827
6) X = OH	1.33	0.590	0.327	0.653	2.00	0.808
7) X = NH_2	2.52	1.06	0.643	1.28	1.99	0.740

ortho Disubstituted, (H, X, X, H, H, H)

							Comparison to monosubstituted	
Substituent	$\lvert\beta\rvert$	$\lvert\beta^{(3)}_{\pm3}\rvert$	$\lvert\beta^{(3)}_{\pm1}\rvert$	$\lvert\beta^{(1)}_{\pm1}\rvert$	$\frac{\lvert\beta^{(1)}_{\pm1}\rvert}{\lvert\beta^{(3)}_{\pm1}\rvert}$	$\frac{\lvert\beta_{(m=3)}\rvert}{\lvert\beta_{(m=1)}\rvert}$	$\frac{\lvert\beta^{(3)}_{\pm1}\rvert_{di}}{\lvert\beta^{(3)}_{\pm1}\rvert_{mono}}$	$\frac{\lvert\beta^{(1)}_{\pm1}\rvert_{di}}{\lvert\beta^{(1)}_{\pm1}\rvert_{mono}}$
1) X = NO_2	3.19	0.156	1.59	1.17	0.735	0.0790	1.30	0.477
2) X = CN	0.653	0.123	0.199	0.398	2.00	0.276	0.952	0.952
3) X = F	0.856	0.00553	0.271	0.542	2.00	0.00913	1.86	1.86
4) X = CH_3	0.822	0.0131	0.319	0.486	1.52	0.0225	1.79	1.83
5) X = OCH_3	2.21	0.0338	0.680	1.41	2.07	0.00995	1.91	2.00
6) X = OH	1.91	0.0786	0.604	1.21	2.00	0.0581	1.85	1.85
7) X = NH_2	3.29	0.00768	1.06	2.07	1.96	0.00330	1.65	1.62

meta Disubstituted, (X, H, X, H, H, H)

							Comparison to monosubstituted		
Substituent	$\lvert\beta\rvert$	$\lvert\beta^{(3)}_{\pm3}\rvert$	$\lvert\beta^{(3)}_{\pm1}\rvert$	$\lvert\beta^{(1)}_{\pm1}\rvert$	$\frac{\lvert\beta^{(1)}_{\pm1}\rvert}{\lvert\beta^{(3)}_{\pm1}\rvert}$	$\frac{\lvert\beta_{(m=3)}\rvert}{\lvert\beta_{(m=1)}\rvert}$	$\frac{\lvert\beta^{(3)}_{\pm3}\rvert_{di}}{\lvert\beta^{(3)}_{\pm3}\rvert_{mono}}$	$\frac{\lvert\beta^{(3)}_{\pm1}\rvert_{di}}{\lvert\beta^{(3)}_{\pm1}\rvert_{mono}}$	$\frac{\lvert\beta^{(1)}_{\pm1}\rvert_{di}}{\lvert\beta^{(1)}_{\pm1}\rvert_{mono}}$
1) X = NO_2	9.30	6.35	0.769	1.54	2.00	3.69	1.70	0.628	0.628
2) X = CN	1.22	0.843	0.0743	0.149	2.00	5.06	1.73	0.355	0.355
3) X = F	0.861	0.525	0.138	0.275	2.00	1.71	2.21	0.946	0.945
4) X = CH_3	0.964	0.607	0.191	0.243	1.27	1.96	2.08	1.08	0.913
5) X = OCH_3	2.21	1.41	0.308	0.614	1.99	2.05	2.16	0.867	0.871
6) X = OH	2.03	1.29	0.283	0.566	2.00	2.04	2.19	0.867	0.867
7) X = NH_2	4.53	2.91	0.592	1.19	2.01	2.19	2.75	0.920	0.933

3.7 INDO Calculations on Specific Chemical Acceptor and Donor Substituents

This section reports INDO calculations for a variety of acceptor/donor substitution patterns on the benzene skeleton, using the approach discussed in Section 3.3.

3.7.1 Hyperpolarizabilities

Tables 3.3 and 3.4 show the norm of the hyperpolarizability for a variety of substitution patterns on the benzene skeleton, which we will examine in light of the above analyses. Table 3.3 compares monosubstituted systems with disubstituted

Table 3.4: Results from INDO calculations on trisubstituted benzene molecules, using the notation of Table 3.3. Only $|\beta|$ is reported since $\beta^3_{\pm 3}$ are the only allowed components.

	trisubstituted (X, H, X, H, X, H)		
Substituent	$\lvert\beta\rvert$	$\lvert\beta_{tri}\rvert/\lvert\beta^{(3)}_{mono}\rvert$	$\lvert\beta_{tri}/\lvert(\beta^{j=3}_{m=3})_{mono}\rvert$
1) X = NO_2	11.7	2.10	3.13
2) X = CN	1.49	1.99	3.05
3) X = F	1.17	2.97	4.91
4) X = CH_3	1.40	2.88	4.78
5) X = OCH_3	3.18	3.03	4.87
6) X = OH	2.94	3.08	4.98
7) X = NH_2	5.45	3.20	5.14

species, for both ortho and meta substitution. *Para* substitution is not included, since such systems have a center of symmetry and so have no hyperpolarizability. Assuming that the substituents can be viewed as altering the internal potential of the carbon to which they are attached, the internal potentials of the various substitution patterns can be written as linear combinations of the symmetry-adapted potentials of Table 3.1. For instance, a unit internal potential for monosubstituted benzene can be written in the vector notation of Table 3.1 as $V_{mono} = [1, 0, 0, 0, 0, 0]$. This potential can be expanded as:

$$V_{mono} = \frac{1}{\sqrt{6}} A_{1g} + \frac{2}{\sqrt{12}} E^{(b)}_{1u} + \frac{2}{\sqrt{12}} E^{(b)}_{2g} + \frac{1}{\sqrt{6}} B_{1u}, \tag{3.29}$$

Similarly, the di-substitutions lead to,

$$V_{ortho} = \frac{1}{\sqrt{3}} A_{1g} + \frac{1}{\sqrt{8}} E^{(a)}_{1u} + \sqrt{\frac{3}{8}} E^{(b)}_{1u} + \frac{1}{\sqrt{8}} E^{(a)}_{2g} + \frac{1}{\sqrt{24}} E^{(b)}_{2g}. \tag{3.30}$$

and

$$V_{meta} = \frac{1}{\sqrt{3}} A_{1g} + \frac{1}{\sqrt{8}} E^{(a)}_{1u} + \frac{1}{\sqrt{24}} E^{(b)}_{1u} - \frac{1}{\sqrt{8}} E^{(a)}_{2g} + \frac{1}{\sqrt{24}} E^{(b)}_{2g} + \frac{1}{3} B_{1u}. \tag{3.31}$$

The *gerade* internal potentials are centro-symmetric and so do not induce a hyperpolarizability. The hyperpolarizability then depends only on the relative amounts of the two *ungerade* configurations. Assuming the hyperpolarizability depends linearly on the internal potential, the hyperpolarizability tensor induced by a B_{1u} potential exhibits only m=3 components, $\beta^3_{\pm 3}$, while an E_{1u} potential induces only m=1 components, $\beta^3_{\pm 1}, \beta^1_{\pm 1}$. In addition, for an E_{1u} potential, the norm of the J=1 components is predicted to be twice that of the J=3, $|\beta^1| \,/\, |\beta^3| = 2$. This ratio is observed for all molecules in Table 3.3, except those involving methyl substituents and meta-dinitrobenzene.

According to eq. 3.30, the *ortho* internal potential has no B_{1u} component, and so the hyperpolarizability should reflect only the E_{1u} potential. The hyperpolarizability resulting from an E_{1u} potential has, assuming linear response, only m=1 components. In Figure 3.4, m=3 components are seen to result from nonlinear effects, and so the magnitude of the m=3 components measures the degree of nonlinearity. For most substituents in Table 3.3, the m=3 components are two orders of magnitude smaller than the m=1 components, indicating that the nonlinearity is quite small. However, for the nitro and cyano substituents, the m=3 components are nearly 10% those of the m=1 components.

A convenient means of comparing the monosubstituted and disubstituted molecules is by considering the effects of rotations on the m=3 and m=1 components of the hyperpolarizability tensor. Within linear response, the effects of the internal potential are additive. Therefore, the ortho-substitution can be considered as the sum of a [1,0,0,0,0,0] internal potential and a [0,1,0,0,0,0] internal potential. Since these two potentials are related by a 60^o rotation about the C_6 symmetry axis of the benzene skeleton, their contributions to the hyperpolarizability can be modeled by rotating the hyperpolarizability of the monosubstituted system by 60^o and adding the resulting tensor to the original, unrotated tensor. For a rotation by an angle ϕ about the C_6 symmetry axis, the tensor components transform as $e^{im\phi}$. For m=1, this is equivalent to the transformation properties of a vector, and so we can use vector addition to determine the expected ratio between disubstituted and monosubstituted species. Addition of two unit vectors with a 60^o angle between them yields a vector of length $\sqrt{3}$. Therefore, within linear response, the ratio of the hyperpolarizabilities for di- and monosubstituted species, $|\beta^{(3)}_{\pm 1}|_{di}/|\beta^{(3)}_{\pm 1}|_{mono}$, should be about 1.7. This it true to within about 10% for all substituents except cyano and nitro, which deviate by up to 70%. These are the same two substituents that showed significant nonlinearity above, as measured by the magnitude of the m=3 components.

The meta disubstituted species may be treated in a manner similar to that of the ortho, but with a rotation of 120^o connecting the two contributing internal potentials, [1,0,0,0,0,0] and [0,0,1,0,0,0]. Addition of two unit vectors with a 120^o angle between them yields a vector of length 1. Thus the ratio of the meta disubstituted species to the monosubstituted species, $|\beta^{(3)}_{\pm 1}|_{di}/|\beta^{(3)}_{\pm 1}|_{mono}$, should be about 1 within linear response. This it true to within about 15% for all substituents except cyano and nitro, again confirming that these substituents lead to significant nonlinearity.

The m=3 components of the hyperpolarizability transform as $e^{i3\phi}$ with respect to rotation about the C_6 axis. The 60^o rotation associated with ortho substitution therefore leads to an exact cancellation of the m=3 components of the hyperpolarizability. This is consistent with the above analysis which concluded that the lack of a B_{1u} component in the internal potential of eq. 3.30 prevents, in linear order, the potential from inducing m=3 tensor components in the hyperpolarizability. For the 120^o rotation associated with *meta* substitution, the m=3 components of the hyperpolarizability add constructively, such that the norm of the m=3 components of the hyperpolarizability, $|\beta^{(3)}_{\pm 3}|_{di}/|\beta^{(3)}_{\pm 3}|_{mono}$, should be 2 for linear response. The observed ratios are within 10% of this value for most substituents. As expected based on previous measures of nonlinearity, the deviation is larger for cyano and nitro. Somewhat surprisingly, the amino substitution deviates by the largest amount, 37%.

For the trisubstituted species of Table 3.4, the internal potential can be considered as arising from the addition of [1,0,0,0,0,0], [0,0,1,0,0,0], and [0,0,0,0,1,0]. These contributions are related by 120^o rotations, and the summation causes the m=1 components to cancel and the m=3 components to add constructively. The lack of m=1 components is a general consequence of the D_{3h} symmetry of the dressed system and so applies even in nonlinear order. Since the m=3 components add constructively, the norm of the hyperpolarizability of the trisubstituted species should be three times the norm of the m=3 components of the monosubstituted species. However, the observed ratio is much closer to 5 for all substituents, with nitro and cyano substituents giving a ratio close to 3. Somewhat surprisingly, the expected ratio of 3 is obtained for the ratio between the hyperpolarizability of the trisubstituted species and the norm of the J=3 components of the monosubstituted species.

In the above arguments, the m=3 (B_{1u} symmetry) and m=1 (E_{1u} symmetry) components of the hyperpolarizability were compared between different substitution patterns. Here, we consider the relative magnitude of the m=3 and m=1 components for a given substitution pattern. The SVD analysis of Table 3.2 indicates that a B_{1u} potential will induce a hyperpolarizability that is 5 to 7 times larger than an E_{1u} potential of identical magnitude. This, combined with the decompositions of eqs. 3.29-3.31 allows us to predict the magnitude of the m=3 and m=1 tensor components of the hyperpolarizability. For the mono-substitution potential of eq. 3.29, the ratio between the B_{1u} and E_{1u} components is $1/\sqrt{2}$. This, combined with the above ratio of 5 to 7 suggests that the ratio of norms of the m=3 to m=1 components should be between 3.5 and 5. However, the observed ratios are less than one. This suggests that an E_{1u} potential induces a hyperpolarizability of roughly equal magnitude to that induced by a B_{1u} potential of the same strength, in disagreement with the ratio of 1/5 to 1/7 obtained from the SVD calculation.

3.7.2 Permanent Moments

In the 1-D model of eqs. 3.8 and 3.9, application of an internal electric field to the skeleton induces both a permanent dipole moment and a hyperpolarizability. The ratio of these two quantities is then a constant that depends only on the skeleton. Here, we consider the extension of this relation to multi-polar systems, by comparing the permanent moments of the benzene skeleton with the hyperpolarizability. In calculating the permanent moments, we consider only the charges due to the π electrons of the benzene skeleton, since it is the π system that dominates the hyperpolarizability. The octupole tensor of the π electron distribution is first calculated in Cartesian coordinates,

$$\mathbf{O}_{i,j,k} = \sum_{A} q_A r_{i,A} r_{j,A} r_{k,A} \tag{3.32}$$

where $r_{i,A}$ is the position of the A^{th} atom along the i^{th} Cartesian axis, and q_A is its π charge. This Cartesian tensor is then transformed into spherical tensor notation using the same method as was used in Section 3.3.

Table 3.5: Comparison of the permanent moments of the π electron density with the hyperpolarizability, as discussed in Section 3.7.2. Monosubstituted systems correspond to the substitution pattern (X, H, H, H, H, H) and trisubstituted systems correspond to (X,H,X,H,X,H).

	Monosubstituted				trisubstituted	
	$\lvert\mathbf{O}_{J=3}\rvert$	$\lvert\mathbf{O}_{J=1}\rvert$	$\lvert\frac{\beta^3}{\mathbf{O}_{J=3}}\rvert$	$\lvert\frac{\beta^1}{\mathbf{O}_{J=1}}\rvert$	$\lvert\mathbf{O}_{J=3}\rvert$	$\lvert\frac{\beta^3}{\mathbf{O}_{J=3}}\rvert$
1) X = NO_2	19.1	17.4	0.291	0.199	62.2	0.188
2) X = CN	8.22	8.67	0.0910	0.0691	23.8	0.0626
3) X = F	7.83	8.52	0.0503	0.0483	35.7	0.0328
4) X = CH_3	14.3	2.22	0.0340	0.170	56.8	0.0246
5) X = OCH_3	21.2	4.32	0.0496	0.231	92.7	0.0343
6) X = OH	22.5	4.59	0.0424	0.201	96.5	0.0305
7) X = NH_2	25.3	3.17	0.0694	0.569	109	0.0501

The permanent moments of the molecule based on the π electron density on the six carbon atoms of benzene were determined and are shown in Table 3.5.[41] The Cartesian permanent octupole moment is then transformed into spherical coordinates using the same method as was used in Section 3.3. With the permanent moments in spherical coordinate notation, we can compare the $J = 3$ and $J = 1$ components of the permanent moments and the first hyperpolarizability responses.

Figure 3.5 shows the relationship between the permanent octupole moment of the molecules versus the $J = 3$ component of the hyperpolarizability. Those molecules which were shown to be linear in Table 3.3 (molecules 3 through 7) exhibit a good correlation between the $J = 3$ component of the hyperpolarizability and the permanent octupole moments. Figure 3.6 shows the relationship between the $J = 1$ component of the permanent octupole moment of the molecule due to the presence of substituents and the $J = 1$ component of the hyperpolarizability of the molecule. Unlike the case with the octupole moments, we do not see the same type of correlation between these values.

3.8 Conclusion

This chapter extends the one-dimensional, scalar-like internal field model of Oudar to multipolar chromophores. The internal field of the one-dimensional model is re-

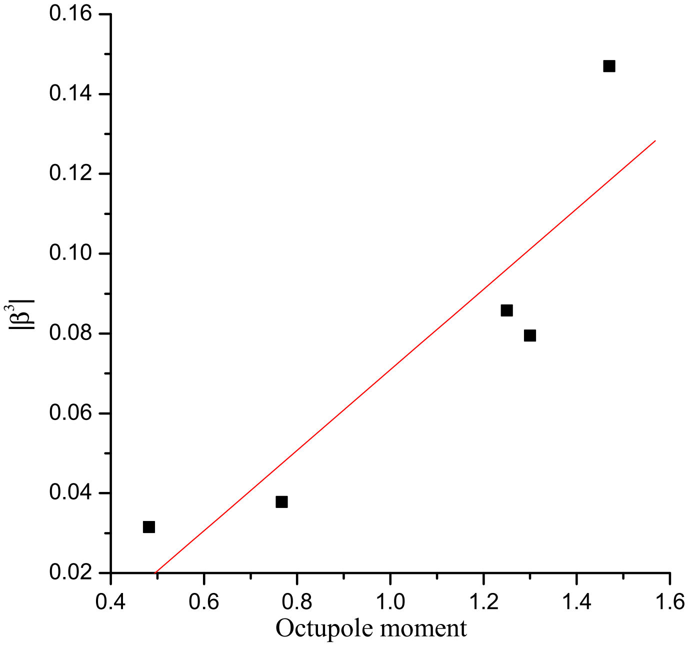

Figure 3.5: Correlation of the norm of the hyperpolarizability with the permanent octupole moment, for the trisubstituted molecules numbered 3 through 7 in Table 3.3. The line is a least squares fit to a linear relationship.

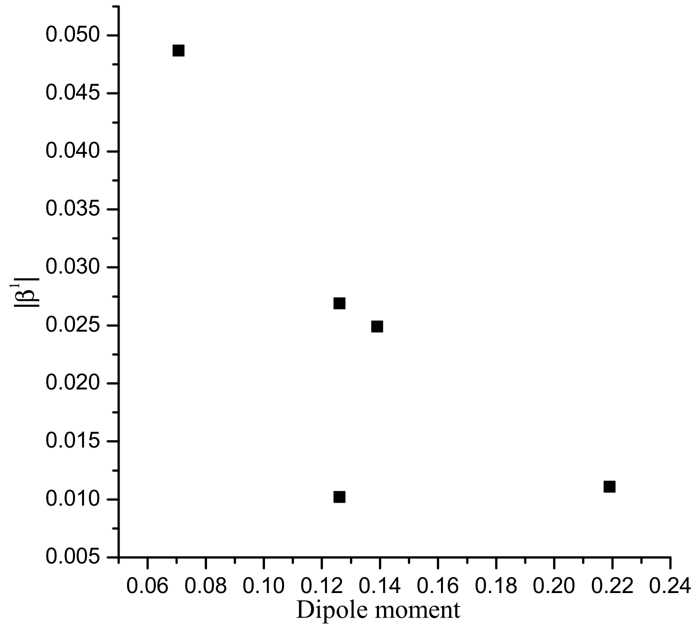

Figure 3.6: Correlation of the norm of the J=1 portion of the hyperpolarizability with the permanent dipole moment for the monosubstituted molecules numbered 3 through 7 in Table 3.3.

placed with a generalized internal potential, and this internal potential may induce hyperpolarizabilities with a variety of tensor components. As in the one-dimensional model, the properties of the substituted molecule are directly related to the properties of the molecular skeleton, eq. 3.15.

The internal potential model assumes the hyperpolarizability and permanent moments are linearly related to the internal potential. An analysis based on symmetry leads to symmetry-adapted internal potentials which, when applied to the molecular skeleton, induce hyperpolarizabilities with the corresponding symmetry. For benzene, two types of potentials, B_{1u} and E_{1u}, lead to non-zero hyperpolarizabilities. The hyperpolarizability induced by a B_{1u} potential has only $m = 3$ tensor components, while that induced by a E_{1u} potential has only $m = 1$ tensor components. An alternative approach to analysing the linear response is through singular value decomposition (SVD). The SVD analysis yields all of the information extracted from the symmetry analysis, and in addition, predicts that a B_{1u} potential will induce a hyperpolarizability that is 5 to 7 times larger in magnitude than that induced by an E_{1u} potential of equivalent magnitude.

By applying internal potentials of large magnitude to the benzene skeleton, we can determine the point at which nonlinear effects become important. Nonlinear effects become important when the potential between adjacent atoms differs by more than about 1eV. For an E_{1u} potential, nonlinear effects introduce hyperpolarizability tensor components with $m = 3$, whereas only $m = 1$ components are allowed in linear response.

A series of substituted benzene molecules are used to test various predictions of the internal potential model. For the substituents (F, $\mathrm{CH_3}$, $\mathrm{OCH_3}$, OH and $\mathrm{NH_2}$), many of the predictions of the internal potential model apply. We will refer to these as weak substituents. The substituents $\mathrm{NO_2}$ and CN appear to be outside of the linear response regime, and we will refer to these as strong substituents. Ortho substitution corresponds to a pure E_{1u} potential and so should lead to hyperpolarizabilities with only $m = 1$ components. This is indeed seen for the weaker substituents, while the stronger substituents do induce some $m = 3$ components. The assumption of linear response also leads to specific predictions for the ratios between the hyperpolarizability induced by mono-, ortho- and meta- substitution on benzene. The predicted ratios differ for the $m = 1$ and $m = 3$ components, since these have very different transformation properties with respect to rotation about the C_6 axis of benzene. Again, the predicted ratios are found to hold for the weak substituents but not for the strong substituents. Linear response also predicts that the ratio between the J=3 components of the hyperpolarizability and the permanent octupole moment of the molecular skeleton should be a constant that depends only on properties of the skeleton. This ratio is relatively constant for the weak substituents, but not the strong substituents. So for the weak substituents, a number of the predictions of the internal field model are found to hold for substituted benzene molecules.

Some predictions of the internal field model are not observed in the series of substituted benzene molecules. For instance, the SVD analysis predicted that the hyperpolarizability induced by a B_{1u} potential should be 5 to 7 times larger than that for an E_{1u} potential.Results for the substituted benzene molecules indicate that the hyperpolarizabilities induced by these potentials have roughly equal magnitudes. This suggests that predictions that rely on the relative magnitudes of the response, rather than just the transformation properties of the various tensor components, may not be reliable. Linear response also predicts that the ratio between the $J = 1$ components of the hyperpolarizability and the permanent dipole moment should be a constant. This is not observed to be the case.

In summary, the internal field model has been extended to multipolar chromophores, and tested against explicit calculations on substituted benzene molecules. The results indicate that for weak acceptor-donor substituents, many of the predictions of the internal field model hold. It therefore provides a good starting point with which to think about the tensor components of the hyperpolarizability that will result from various substitution patterns.

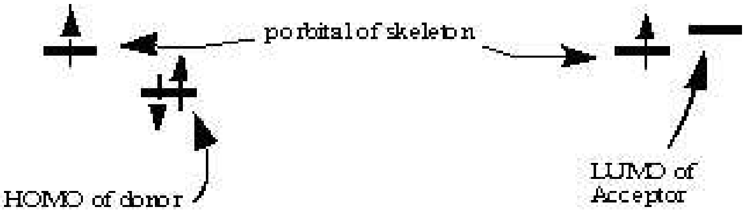

Figure 3.7: Schematic representation of the effects of electron donor and acceptor substituents on the benzene skeleton. The left panel shows the interaction between the p-orbital on benzene and the HOMO of a donor. The right panel shows the interaction between the p-orbital on benzene and the LUMO of an acceptor.

3.9 Appendix

3.9.1 Quantum chemical representation of acceptor and donor substituents

The presence of acceptor and donor substituents attached to a molecular skeleton creates an internal potential within the molecule. To achieve this in the model, we view the effect of the substituent as a perturbation to the energy of the orbitals of the carbon atom to which the substituent is attached. The rationale for this approach is shown schematically in Figure 3.7.

For an electron donating substituent, the HOMO of the substituent interacts with the orbitals of the benzene ring. Since this orbital has an energy below the benzene π system, interactions raise the energy of the orbitals on the carbon to which the substituent is attached. For an electron withdrawing substituent, the LUMO of the substituent has an energy above the benzene π system, and interactions lower the energy of the carbon atom to which the substituent is attached.

Chapter 4

Investigation of additional molecular substitution patterns using the generalized internal potential model

Work done in collaboration with Professor Joseph Zyss
Ecole Normale Supérieure de Cachan, Cachan, France

4.1 Introduction

This chapter presents symmetry analysis and singular value decomposition (SVD) calculations following the procedures of chapter 3 on three additional molecular skeletons. The molecular skeletons considered in this chapter are a carbon tetrahedral skeleton (T_d), D_{3h}, and D_3 molecular skeletons (Figure 4.1). The carbon tetrahedral skeleton is of interest because it has the same geometry as carbon tetrachloride which, as early as 1964, had been shown to exhibit only β_{xyz} hyperpolarizability components.[42] The triphenyl skeleton is of interest because it is the molecular

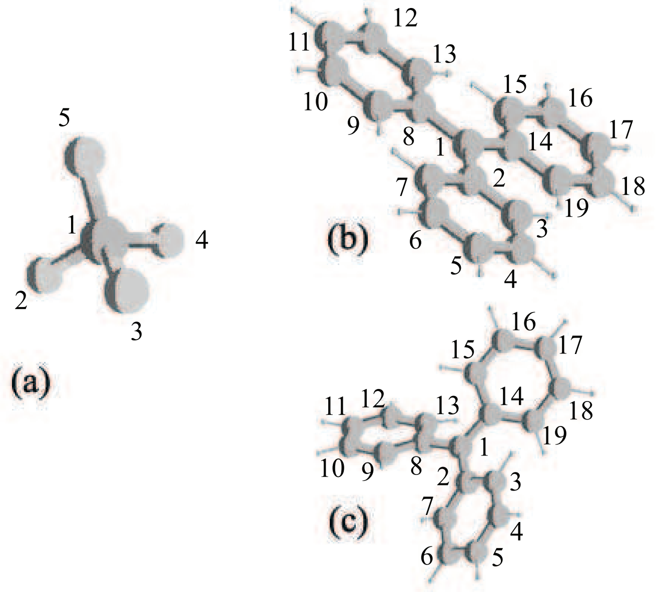

Figure 4.1: Molecular skeletons for (a) carbon tetrafluoride, (b) the idealized triphenyl geometry, and (c) the geometry optimized triphenyl molecule. Molecule (a) has tetrahedral (T_d) symmetry, molecule (b) D_{3h} symmetry, and molecule (c) D_3 symmetry.

skeleton for molecules such as crystal or ethyl violet which have been the subject of numerous experimental studies.[21, 36, 43] These skeletons allow us to examine a variety of two and three dimensional substitution patterns.

4.2 Symmetry Analysis

Following the procedure of section 3.4, the symmetry-adapted hyperpolarizability tensors and potentials were determined for the three molecular skeletons of Figure 4.1. Carbon tetrafluoride has tetrahedral (T_d) symmetry, the idealized planar triphenyl molecule has D_{3h} symmetry, and the optimized geometry has D_3 symmetry. Unlike section 3.4 however, here only a limited number of sites on the molecular skeletons are considered as locations for acceptor-donor substitution. In the carbon tetrafluoride molecular skeleton, the fluoride atoms are considered as substitution sites. In the triphenyl skeleton, atoms 5, 11, and 17 are considered as substitution sites (see Figure 4.1).

Examination of the symmetry adapted internal potentials and the hyperpolarizabilities show some of the same characteristics as those seen in section 3.4. Note that none of the molecular skeletons considered here have a center of inversion. Therefore, it is possible that the substituted molecule may give rise to a non-zero hyperpolarizability. The absence of a center of inversion is reflected by the the presence of the totally symmetric irreducible representations in the hyperpolarizabilities and potentials of Table 4.1. But, as in section 3.4, only those hyperpolarizabilities of Table 4.1 corresponding to the molecular substitution patterns (**V**) found in the table are accessible. For example, although the symmetry analysis shows T_1 symmetry as a possible hyperpolarizability for the tetrahedral skeleton, it is not accessible by any substitution pattern on the molecule. In the optimized triphenyl geometry hyperpolarizabilities with A_1, A_2, and E representations are possible. Of these, however, only A_1 and E representations are accessible through molecular substitution patterns. Also, as in benzene, the SVD results show that the hyperpolarizability depends on the m value of the spherical harmonic representation. In other words, the A_1 representation for the tetrahedral molecule of Table 4.1 only has $m = 2$ components and the T_2 representation has $m = 0, 1, 3$ components.

4.3 Singular value decomposition

As in section 3.5, it is also possible to extract the information contained in Table 4.1 through singular value decomposition (SVD). In the tetrahedral molecules, the **L** matrix of eq. 3.27 is 27x4 and for the triphenyl skeletons, 27x3. As in benzene, the characteristic directions of the tetrahedral and triphenyl skeletons match those determined in the symmetry analysis of the previous section (Table 4.1). Similar to section 3.5, the values of **T** (Table 4.2) can provide information about the relative contributions of the allowed substitution patterns of Table 4.1 in a general substitution pattern on a molecular skeleton. In these molecular skeletons, all of the representations are expected to have roughly equal magnitudes.

Table 4.1: Symmetry-adapted hyperpolarizability tensors and internal potentials for tetrahedral, idealized triphenyl, and geometry optimized triphenyl molecular skeletons of Figure 4.1. The notation $\{\bar{\beta}^3_1, \bar{\beta}^3_{-1}\}$ indicates that any linear combination of β^3_1 and β^3_{-1} will transform with the indicated symmetry. The internal potentials are given as a normalized vector representing the value of the potential on each of the three carbon atoms 5, 11, and 17 for the triphenyl skeleton of Figure 4.1. In the doubly and triply degenerate internal potentials, any linear combination of the given potentials is valid.

	Carbon tetrafluoride, T_d symmetry Hyperpolarizabilities	
Symmetry	J = 3	J = 1
A_1	$\frac{1}{\sqrt{2}}\left[\bar{\beta}^3_{-2} - \bar{\beta}^3_2\right]$	
T_1	$\{\bar{\beta}^3_3, \bar{\beta}^3_{-3}, \bar{\beta}^3_2, \bar{\beta}^3_{-2}, \bar{\beta}^3_1, \bar{\beta}^3_{-1}\}$	$\{\bar{\beta}^1_1, \bar{\beta}^1_{-1}, \bar{\beta}^1_0\}$
T_2	$\{\bar{\beta}^3_3, \bar{\beta}^3_{-3}, \bar{\beta}^3_1, \bar{\beta}^3_{-1}, \bar{\beta}^3_0\}$	$\{\bar{\beta}^1_1, \bar{\beta}^1_{-1}, \bar{\beta}^1_0\}$
	Internal Potentials	
A_1	$\frac{1}{\sqrt{2}}[1,1,1,1]$	
T_2	$\{\frac{1}{\sqrt{12}}[3,-1,-1,-1]\ ,\frac{1}{\sqrt{2}}[0,0,-1,1],\frac{1}{\sqrt{6}}[0,2,-1,-1]\}$	
	Ideal Triphenyl Geometry, D_{3h} symmetry Hyperpolarizabilities	
Symmetry	J = 3	J = 1
A'_1	$\frac{1}{\sqrt{2}}\left[\bar{\beta}^3_3 + \bar{\beta}^3_{-3}\right]$	
E'	$\{\bar{\beta}^3_1, \bar{\beta}^3_{-1}\}$	$\{\bar{\beta}^1_1, \bar{\beta}^1_{-1}\}$
	Internal Potentials	
A_1	$\frac{1}{\sqrt{3}}[1,1,1]$	
E	$\{\frac{1}{\sqrt{6}}[2,-1,-1]\ ,\frac{1}{\sqrt{2}}[0,1,-1]\}$	
	Optimized Triphenyl Geometry, D_3 symmetry Hyperpolarizabilities	
Symmetry	J = 3	J = 1
A_1	$\frac{1}{\sqrt{2}}\left[\bar{\beta}^3_3 + \bar{\beta}^3_{-3}\right]$	
A_2	$\frac{1}{\sqrt{2}}\left[\bar{\beta}^3_{-3} - \bar{\beta}^3_3\right]\ ,\ \frac{1}{\sqrt{2}}\bar{\beta}^3_0$	$\bar{\beta}^1_0$
E	$\{\bar{\beta}^3_1, \bar{\beta}^3_{-1}\}$	$\{\bar{\beta}^1_1, \bar{\beta}^1_{-1}\}$
	Internal Potentials	
A_1	$\frac{1}{\sqrt{3}}[1,1,1]$	
E'	$\{\frac{1}{\sqrt{6}}[2,-1,-1]\ ,\frac{1}{\sqrt{2}}[0,1,-1]$	

Table 4.2: Results of the SVD analysis on the benzene skeleton, using the quantum chemical models discussed in Section 3.3. Only those values of the matrices **U** and **W** corresponding to nonzero values of **T** are reported. In the INDO models, results are shown with the internal potential applied to the entire atom or to the just the π orbitals.

Hyperpolarizability Magnitudes, from the matrix **T**	
Carbon Tetrafluoride, T_d symmetry	
A_1	T_2
0.0747	0.0552
Ideal geometry, D_{3h} symmetry	
A_1'	E'
67.2	63.5
Optimized geometry, D_3 symmetry	
A_1	E
29.4	36.4

4.4 Discussion

The methods developed in Chapter 3 are applied to three additional molecular skeletons. The results yield symmetry adapted substitution patters along with the hyperpolarizabilities induced by these patterns. As in benzene, different symmetry-adapted patterns lead to hyperpolarizabilities with different m values. The various substitution patterns are predicted to yield hyperpolarizabilities of similar magnitude.

Part II

Periodic Materials

Chapter 5

An introduction to periodic systems

5.1 Introduction

The following three chapters deal with calculations involving periodic boundary conditions. This chapter presents some preliminary background information that is useful in the discussion of the following chapters. Since the following chapters deal with one- and two-dimensional periodic systems, we will concentrate our discussion on examples with these two dimensionalities.

5.2 The lattice of the periodic system

We will start by defining the periodic system under consideration. As an example, consider a one-dimensional infinite chain with the lattice vector, $\vec{R}$, defining the distance from one site in the chain to another (Figure 5.1). Any translation along the chain by an integer multiple amount of the lattice vector $(m\vec{R})$ leaves the system unchanged.[44, 38, 45, 46]

In a multi-dimensional system, the translation vector $\vec{R}$ has multiple components, $\vec{R} = \sum_i m_i \hat{R}_i$, where m_i is an integer and $\hat{R}_i$ is a unit vector of the lattice. Each component of $\vec{R}$ represents a translation by an integer amount in some direction in

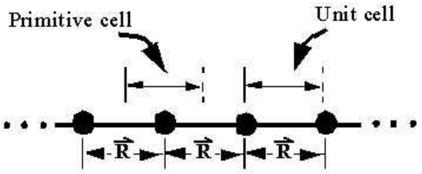

Figure 5.1: One dimensional infinite chain with lattice vector $\vec{R}$. The centered primitive cell of this lattice has its origin at one of the atoms of the lattice. The distance from the origin of the primitive cell to its sides is $\frac{|\vec{R}|}{2}$. The dashed line indicates that only one of the two sides is contained in the primitive or unit cell.

the lattice such that the lattice remains unchanged. For example, in a two dimensional system $\vec{R}$ would have the form $\vec{R} = m\hat{R}_1 + n\hat{R}_2$ (Figure 5.2). The unit cell is the regular polyhedron that is created by unit translations along the lattice vectors.[44] The choice of lattice vectors is not unique; the only requirement is that repeated translation by the unit vectors provide a covering of the lattice.[44, 45] In a cubic lattice, such as that of Figure 5.2(a), $\hat{R}_1$ and $\hat{R}_2$ are orthogonal, although there is no requirement that the unit vector be orthogonal, *e.g.*, the unit vectors of the hexagonal lattice in Figure 5.2(b) have an angle of 60^o between them.[44, 45]

It is often convenient to determine the minimum number of points that can make up a unit cell, referred to as the primitive unit cell. The primitive cell is defined as the maximal set of translationally inequivalent points in the lattice. The primative unit cell consists of an open regular polyhedron created by the normal bisector planes of the unit vectors of $\vec{R}$ (Figures 5.1 and 5.2), which by definition does not contain all of its sides (otherwise some points would be members of multiple primitive cells).[44] In the example of a one-dimensional infinite chain with only one type of atom, the primitive cell corresponds to one atom per cell. For solid state theory it is also useful to place the origin at the center of the cell, as in Figures 5.1 and 5.2. Often, centering the primitive cell best reflects the symmetry of the system, *e.g.,* compare the centered primitive cell of the hexagonal lattice with the crystallographic cell of the same lattice (see Figure 5.2(b)).[44] Centering the primitive cell allows for solutions to operations on the system wavefunctions, such as solutions to the Hartree-Fock problem, to be symmetric about the cell origin, thus reflecting the invarience of the solutions to

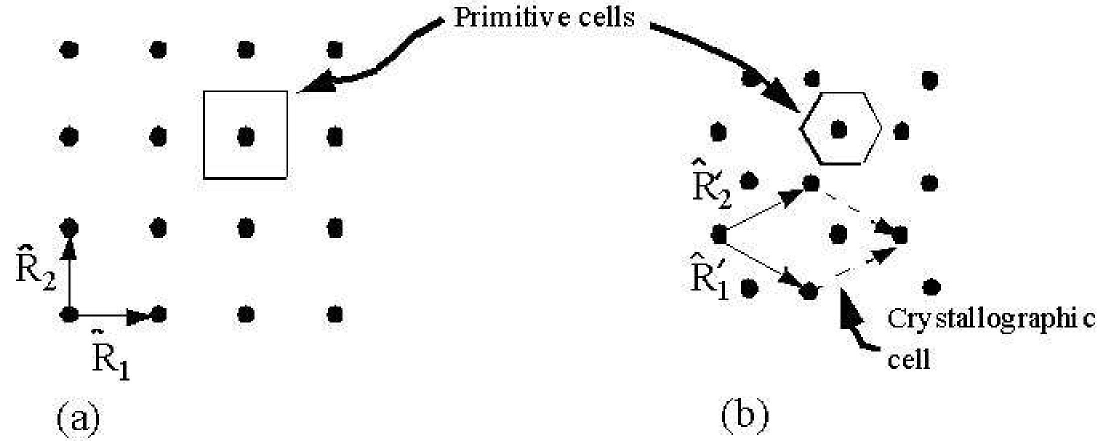

Figure 5.2: Two dimensional lattices. Lattice (a) has orthogonal lattice unit vectors ($\hat{R}_1$ and $\hat{R}_2$). Lattice (b) has non-orthogonal lattice vectors ($\hat{R}'_1$ and $\hat{R}'_2$). The centered primitive cells are also shown for each lattice. In the hexagonal lattice, the crystallographic unit cell is shown, illustrating how the centered primitive cell expresses the symmetry of the hexagonal lattice.

changing the sign of the wavevector, *i.e.*, $E(\vec{k}) = E(-\vec{k})$ (see below).[44, 45]

5.3 Periodic functions

To obtain information about the infinite periodic system, functions that exhibit the same transformation properties as the periodic system are required. The goal is to create functions that are invariant under the operations of the system's point group.

5.3.1 Bloch functions

In a crystal, each electron experiences a potential field due to the presence of the other electrons and nuclei. Functions which are periodic and take into account the potential field must satisfy Bloch's theorem[44, 45],

$$\psi_k\left(\vec{r}+\vec{R}\right) = e^{i\vec{k}\cdot\vec{R}}\psi_k\left(\vec{r}\right), \tag{5.1}$$

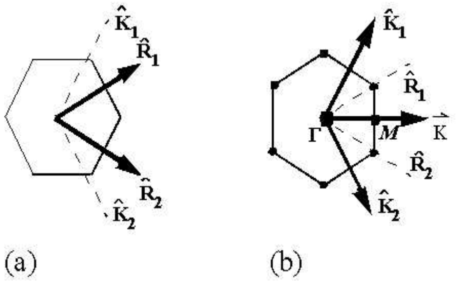

Figure 5.3: Example of a two dimensional, hexagonal lattice showing the unit vectors of the (a) direct lattice ($\hat{R}_1$ and $\hat{R}_2$) and those of the (b) reciprocal lattice ($\hat{K}_1$ and $\hat{K}_2$). The filled circles on Figure (b) represent points where the Brillouin zone intersects the Fermi surface and other points of interest in the Brillouin Zone.

where $\vec{r}$ is any vector, $\vec{R}$ is a lattice vector, and $\vec{k}$ is the wavevector. An example of a function that satisfies Bloch's theorem is the Bloch function,

$$\psi_k(\vec{r}) = e^{i\vec{k}\cdot\vec{r}}u_k(\vec{r}), \tag{5.2}$$

where $u_k(\vec{r})$ is a functinon that is periodic in the lattice,

$$u_k(\vec{r}+\vec{R}) = u(\vec{r}). \tag{5.3}$$

5.3.2 The reciprocal lattice

As is stated in section 5.2, the lattice vectors are not necessarily orthogonal. To obtain a periodic function in a lattice with a non-orthogonal set of unit vectors one must define a set of reciprocal lattice vectors, $\hat{K}_i$, such that $\hat{K}_i \cdot \hat{R}_j = 2\pi\delta_{i,j}$. With $\vec{k}$ of eq. 5.2 redefined as,

$$\vec{k} = g\hat{K}_1 + h\hat{K}_2 + k\hat{K}_3, \tag{5.4}$$

eq. 5.2 still satisfies Bloch's theorem. It is now useful to refer to the lattice formed by $\hat{R}_i$ as the direct lattice and the set of points formed by repeated translations of $\hat{K}_i$ as the reciprocal lattice. Figure 5.3 shows examples of both the direct and reciprocal lattices of a two-dimensional, hexagonal system.

The primitive cell of the reciprocal lattice is referred to as the first Brillouin zone (defined in the same fashion as the primitive cell of the direct lattice). In the Brillouin zone, values of the wavevector become discretized in correspondence to the number of unit cells explicitly considered in the system.[44, 45] For periodic systems with N unit cells the function must be invarient to translations by $N\vec{R}$. This is accomplished by setting $\alpha_i = \frac{2\pi k_i}{N}$, with $k_i = 1, \cdots, N$.[44, 45, 46] It is useful to define the Brillouin zone so that the energy is symmetric about the origin of the Brillouin zone. This can be achieved by setting the possible values of $|\vec{k}|$ to $-\frac{(N-1)}{2}, \cdots, \frac{(N-1)}{2}$ and moving the origin to the center of the Brillouin zone. It is also useful to define certain points of high symmetry within the Brillouin zone; the origin of the Brillouin zone is given the symbol Γ and points at the surface of the Brillouin zone along directions $\vec{K}$ of high symmetry are given the symbol M (examples of these points can be found in Figure 5.3).[46]

Within the Brillouin zone, surfaces of constant energy can be determined, the dimension of which is one less than that of the dimension of the Brillouin zone. For example, in a two dimensional Brillouin zone, the constant energy surfaces are lines. One such surface of particular interest is the Fermi surface, a surface whose energy is half-way between the energy of the highest occupied molecular orbital (HOMO) and the energy of the lowest unoccupied molecular orbital (LUMO). The location of the Fermi surface has important consequences in determining the conduction properties of a material. The size of the gap between the HOMO and LUMO determines whether the material is a conductor, insulator, or semi-metal. One definition of a conductor is that both the HOMO and LUMO intersect the Fermi level at the same point. As was discussed above, values of $\vec{k}$ in the Brillouin zone are discretized. A periodic system is a conductor if at least one of the allowed values of $\vec{k}$ passes through a point where the HOMO and LUMO touch the Fermi surface.

5.3.3 Wannier functions

Bloch functions, eq. 5.2, are delocalized over the chain and reflect the periodicity of the direct lattice.[45] If we wish to examine localized phenomena, then functions that are localized on unit cells would be useful.[44] Wannier functions, $W_n^{band}(\vec{r})$, are a type of function that is periodic in the reciprocal lattice and localized in the

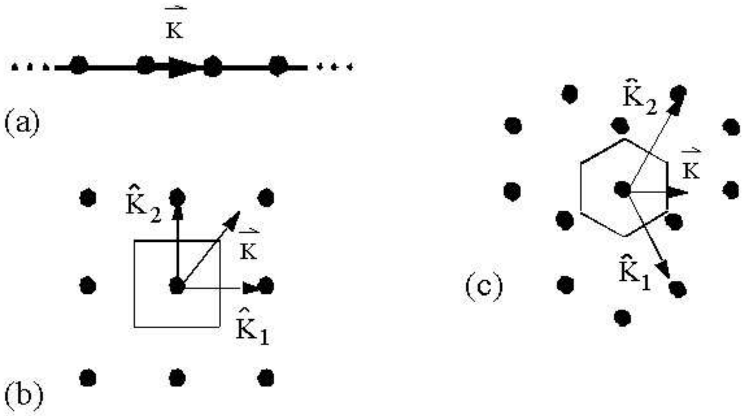

Figure 5.4: Examples of the reciprocal lattices for (a) an one-dimensional chain, (b) a two dimensional cubic reciprocal lattice, and (c) a hexagonal reciprocal lattice. In each lattice an example of a possible choice for $\vec{k}$ of $\hat{k}_1 = \hat{k}_2$ is shown.

direct lattice.[45] The Fourier series for the wavefunction may be written as a periodic function in the reciprocal lattice,

$$\psi^{(\vec{k})}_{band}(\vec{r}) = \sum_{\vec{R}} W^{band}(\vec{r} - \vec{R}) e^{i\vec{k}\cdot\vec{R}}, \tag{5.5}$$

where the sum is over all lattice vectors. The Wannier function is then the inverse Fourier transform of the Bloch functions,

$$W^{band}(\vec{r} - \vec{R}) = \frac{1}{\sqrt{N}} \sum_{k} e^{-ik(\vec{r}-\vec{R})} \Psi^{(k)}_{band}(\vec{r}), \tag{5.6}$$

where $\Psi^{(k)}_{band}(\vec{r})$ are the molecular wavefunctions written in Bloch form. While $\Psi^{(k)}_{band}(\vec{r})$ is associated with a particular wavevector $(\vec{k})$ of the lattice, the Wannier function, $W^{band}_n(\vec{r})$, is a localized function centered on the unit cell.

5.4 Operator evaluations in periodic boundary conditions

As an example of how periodic functions can be used to obtain information about the system, we will consider the Hartree-Fock problem within periodic boundary conditions. Start with a wavefunction for a one-dimensional chain,

$$\mid \psi_k \rangle = \frac{1}{\sqrt{N}} \sum_n e^{i\vartheta kn} \left| n \right\rangle , \tag{5.7}$$

where n is a unit cell index, N is the total number of unit cells, k is the wavevector, $\vartheta = \frac{2\pi}{N}$, and $|n\rangle$ is the Wannier function centered on the unit cell n. Consider a general operator, $\hat{O}$, that depends only on the distance between unit cells, *e.g.*, the Fock operator, $\hat{F}$ and the Hamiltonian, $\hat{H}$. The expectation value of $\hat{O}$ for the function ψ is then

$$\begin{aligned} \langle\ \psi^{\dagger}_{k'} \mid \hat{O} \mid \psi_k \ \rangle &= \frac{1}{N} \sum_{n,m} e^{-i\vartheta k'm} \left\langle m \right| \hat{O} \left| n \right\rangle e^{i\vartheta kn} \\ &= \frac{1}{N} \sum_{n,m} e^{i\vartheta (kn - k'm)} \left\langle m \right| \hat{O} \left| n \right\rangle \\ &. \end{aligned} \tag{5.8}$$

$(kn - k'm)$ can be rewritten as $k(n-m) - (k'-k)m$ and the distance between unit cells defined as $\Delta = (n-m)$. Substituting these relations into eq. 5.8 gives,

$$\langle\ \psi^{\dagger}_{k'} \mid \hat{O} \mid \psi_k \ \rangle = \frac{1}{N} \sum_{n,m} e^{i\vartheta k\Delta} e^{i\vartheta (k'-k)m} \left\langle m \right| \hat{O} \left| n \right\rangle . \tag{5.9}$$

Recall that the operator $\hat{O}$ depends only on the distance between unit cells not their absolute position on the chain, and so the matrix elements between unit cells m and n is

$$\left\langle m \right| \hat{O} \Big| \, n \, \Big\rangle = \left\langle 0 \right| \hat{O} \Big| \, \Delta \, \Big\rangle \, . \tag{5.10}$$

In summations over m, the second exponential in eq. 5.9 reduces to $N\delta_{k,k'}$. Using equation 5.10, eq. 5.9 can be rewritten ,

$$\langle\ \psi^{\dagger}_{k'} \mid \hat{O} \mid \psi_k \ \rangle = \sum_{\Delta} e^{i\vartheta k\Delta} \left\langle 0 \right| \hat{O} \Big| \, \Delta \Big\rangle \, \delta_{k',k}. \tag{5.11}$$

Choices for the values of ϑ and k corresponding to that of section 5.3.2 can be obtained for the exponential in eq. 5.11 by setting $\vartheta = \frac{2\pi}{N}$ and allowing k to range over $-\frac{(N-1)}{2}, \cdots, \frac{(N-1)}{2}$, N odd.

5.4.1 Determination of the Hückel energy in a periodic system

To illustrate the use of eq. 5.11 for a specific operator, $\hat{H}$, we will determine the energy of a linear chain of N atoms, such as that shown in Figure 5.1. The energy of the system can be determined by,

$$E(\vec{k}) = \frac{\langle\, \psi^{\dagger}_{\vec{k}} \mid H \mid \psi_{\vec{k}} \,\rangle}{\langle\, \psi^{\dagger}_{\vec{k}} \mid \psi_{\vec{k}} \,\rangle}. \tag{5.12}$$

Substituting eq. 5.11 into eq. 5.12, and since, for $|\psi_k\rangle$ of eq. 5.7, $\langle\psi^{\dagger}_{\vec{k}}|\psi_{\vec{k}}\rangle = 1$,

$$\vec{E}(\vec{k}) = \langle\, \psi^{\dagger}_{\vec{k}} \mid H \mid \psi_{\vec{k}} \,\rangle \; = \sum_{\Delta} e^{i\vartheta k\Delta} \left\langle O \right| H \left| \Delta \right\rangle . \tag{5.13}$$

In Hückel theory,

$$\langle 0 \left| H \right| \Delta \rangle = \begin{cases} E_o, & \text{if } \Delta = 0 \\ \beta, & \text{if } \Delta = \pm 1, \\ 0, & \text{otherwise} \end{cases} \tag{5.14}$$

where E_o is the on-atom energy and β is the hopping integral from one atom to the next. Substitution of eq. 5.14 into eq. 5.13 results in an expression for the band structure of a one-dimensional Hückel chain,

$$\begin{aligned} E(\vec{k}) &= E_o + (-\beta) \sum_{\Delta} e^{i\vartheta k\Delta} \left[\delta_{\Delta,1} + \delta_{\Delta,-1}\right] \\ &= E_o + (-\beta) \left[e^{i\vartheta k} + e^{-i\vartheta k}\right] \\ &= E_o - 2\beta cos(\vartheta k). \end{aligned} \tag{5.15}$$

Figure 5.5 shows the band structure for eq. 5.15. Since $cos(\vartheta k)$ is periodic over the range $-\pi$ to π, eq. 5.15 and Figure 5.5 straightforwardly illustrate how choosing $\vartheta = \frac{2\pi}{N}$ and allowing k to range over $-\frac{(N-1)}{2}, \cdots, \frac{(N-1)}{2}$, N odd, reflects the periodicity of the exponential.

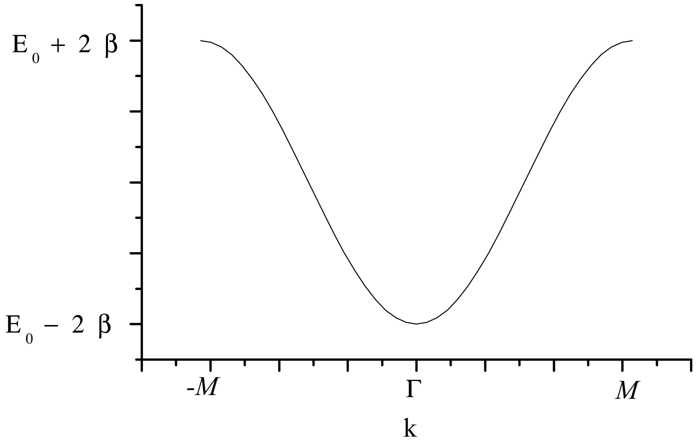

Figure 5.5: Band structure solutions of eq. 5.15 for an one dimensional infinite chain. Where Γ is the origin of the Brillouin zone and M is a point on the surface of the Brillouin zone along the direction $\vec{k}$ indicated in Figure 5.4(a).

Chapter 6

INDO/SCI in periodic boundary conditions: the absorption spectrum of poly(*para*-phenylene vinylene)

6.1 Introduction

Conjugated polymers are an important class of organic semiconductors that may be useful for the construction of flat screen displays[3, 4], transistors[12] and lasers[5, 6]. The electronic structure of these materials is quite complex, and constructs borrowed both from the photophysics of organic molecules and the photophysics of bulk semiconductors have proven useful in their description. A central goal of the work presented here is to develop methods and tools that further promote the integration of these two approaches. The Intermediate Neglect of Differential Overlap (INDO)[27] method has been found to be quite useful in describing the photophysics of medium-size organic molecules; however, current implementations of INDO theory may be applied only to oligomers of conjugated polymers[47]. Here, we develop the tools needed to perform INDO calculations within periodic boundary conditions. This generates constructs such as the band structure and Wannier functions that help cast the results in the language of solid-state physics. In addition, the use of periodic boundary conditions makes calculations on large systems computationally feasible and, due to the introduction of the crystal momentum as a good quantum number, aids in the interpretation of the complex energy-level structure that arises from INDO calculations on large systems.

These tools are especially useful for studying the photophysics of conjugated polymers with more than one active valence and conduction band. Much of our current theoretical understanding of the electronic structure of conjugated polymers is based on studies performed on two-band systems, such as the π-electron model of polyacetylene, for which there is only one type of hole and one type of electron[48, 14, 17, 16]. This limits the number of parameters in the model and makes it possible to explore a wide range of parameter space. Indeed, such studies have revealed many general features of the photophysics, including the nature of the $2A_g$ electronic state[14, 17] and the essential states that dominate the nonlinear optical response[16].

PPV and many other conjugated polymers, however, have a number of bands that participate in the photophysics and this raises new and interesting questions that are beginning to be addressed[49, 50, 51, 52]. Studies of these systems are complicated by the large number of parameters present in models of multi-band systems and the finding that many predictions are sensitive to the choice of these parameters. INDO has the advantage of providing a systematic approach to the determination of these parameters from the chemical structure. Given the chemical structure of organic molecules, INDO has been quite successful in predicting the photophysical properties. It therefore provides a useful starting point for studies of multi-band conjugated polymer systems.

As a first application of these tools, we present studies of the electronic structure of PPV, an important candidate material for flat-screen display technologies. In particular, we consider the origin of the 3.7 eV transition in the UV/VIS spectrum of PPV[52, 53, 54, 55, 56]. This transition becomes allowed only through electron-hole symmetry breaking, and here we explore various mechanisms for breaking this symmetry. The formalism is developed in Sec. 6.2 and the details of the calculations are given in Sec. 6.3, followed by a discussion in Sec. 6.4.

6.2 Formalism

6.2.1 Hartree-Fock

The INDO Hamiltonian is discussed in detail in Ref. [27], and is summarized here at a level that establishes the notation. The one-electron matrix elements on a single atom, $U_{i,i}$, are obtained from the Slater-Condon factors. Between atoms, the one electron matrix elements are given by,

$$(i\left|h_1\right|j)=\bar{S}_{i,j}\left(\beta_A+\beta_B\right)/2, \tag{6.1}$$

where $\bar{S}_{i,j}$ is the overlap between the i^{th} and j^{th} orbitals, scaled such that the π overlaps between p-orbitals are multiplied by 1.266 and the σ overlaps between p-orbitals are multiplied by 0.585. β_A and β_B are semi-empirical parameters that depend only on the respective elements. The overlaps between Slater orbitals are calculated using the method of Fernandez Rico *et al*[57].

We use chemist's notation for the two electronic integrals, $(ij\,|\,k\,l)$[58]. Both Coulomb and exchange integrals are retained for orbitals residing on the same atom,

$$(ii\,|\,j\,j)_{atom\ A}=J^A_{i,j} \tag{6.2}$$

$$(ij\,|\,j\,i)_{atom\ A}=K^A_{i,j}, \tag{6.3}$$

These are obtained from the Slater-Condon factors as in Ref. [27]. The zero differential overlap approximation is assumed between atoms,

$$(ij\,|\,k\,l)=\gamma_{A,B}\delta_{i,j}\delta_{k,l} \tag{6.4}$$

where the i^{th} orbital is on atom A, and the k^{th} orbital is on atom B. $\gamma_{A,B}$ is also used to describe the Coulomb repulsion between nuclei, and the attraction between an electron on atom A and the core of atom B. The Mataga-Nishimoto form is used for $\gamma_{A,B}$

$$\gamma_{A,B}=\frac{f_\gamma}{2f_\gamma/\left(\gamma_{AA}+\gamma_{BB}\right)+\varepsilon R_{A,B}} \tag{6.5}$$

where $\gamma_{A,A}$ is the Hubbard parameter for atom A, and $R_{A,B}$ is the distance between atoms A and B. The form used in INDO is equivalent to that of Eq. (6.5) with $\varepsilon =$

1/1.2, a value chosen to obtain better agreement with the spectrum of benzene[27]. But at long range, the potential is then stronger than a bare Coulomb force, and this is not appropriate for large systems such as those considered here. In particular, this would serve to raise the exciton binding energy. In the calculations presented here, we use $\varepsilon = 1$.

The Fock operator, written in atomic orbitals, is then,

$$\begin{aligned} F_{\substack{i,i \\ i \in A}} &= U_{i,i} + \sum_{j \in A} P_{j,j} \left[J^A_{j,i} - \frac{1}{2} K^A_{j,i} \right] \\ &\quad + \sum_{B \neq A} \left[P_B - Z^B_{eff} \right] \gamma_{A,B} \end{aligned} \tag{6.6}$$

$$F_{\substack{i,j \\ i,j \in A}} = P_{i,j} \left[\frac{3}{2} K^A_{i,j} - \frac{1}{2} J^A_{i,j} \right] \tag{6.7}$$

$$F_{\substack{i,j \\ i \in A, j \in B}} = \bar{S}_{i,j} \frac{(\beta_A + \beta_B)}{2} - \frac{1}{2} P_{i,j} \gamma_{A,B} \tag{6.8}$$

where i and j label atomic orbitals, A and B label atoms, $P_{i,j}$ is the density matrix, P_B is the total electron density on atom B, and Z^B_{eff} is the core charge of atom B.

For a polymer with N unit cells and periodic boundary conditions, the molecular orbitals may be written,

$$\left| \Psi^{(k)}_{band} \right\rangle = \frac{1}{\sqrt{N}} \sum_n e^{i\,k\,n} \sum_a C^{(k)}_{a,band} \left| \begin{matrix} n \\ a \end{matrix} \right\rangle , \tag{6.9}$$

where the notation $\left| \begin{matrix} n \\ a \end{matrix} \right\rangle$ will be used throughout this paper to indicate the a^{th} atomic orbital in the n^{th} unit cell. Unless otherwise noted, all sums are over the entire range of the summation index, i.e. $n = 1 \ldots N$. The labels *band* and k denote the band and wavevector of this orbital. $k = \theta j$ with j an integer between 1 and N, and $\theta = \frac{2\pi}{N}$. Both n and j are invariant with respect to addition of N, and it is often convenient to use the range $-\eta \ldots \eta$, with $\eta = \frac{N-1}{2}$ and N odd.

Note that for $k \neq 0$, $C^{(k)}_{a,band}$ is complex. The density matrix is then,

$$P_{\substack{n,m\\ c\ \ d}} = \frac{2}{N}\sum_{k}\sum_{band}^{occ} e^{ik(n-m)} C^{(k)}_{c,band} C^{(k)*}_{d,band}. \tag{6.10}$$

The Fock operator is block diagonal in the wavevector k, leading to N blocks of the form,

$$F^{(k)}_{a,b} = \sum_{n} e^{-ikn} F_{\substack{n,0\\ a\ \ b}}\,, \tag{6.11}$$

where $F_{\substack{n,0\\ a\ \ b}}$ is the Fock operator in the atomic basis, Eqs. (6.6-6.8). Due to periodic boundary conditions, an atom is invariant to displacement by $N\mathbf{B}$, where $\mathbf{B}$ is the Brillioun vector connecting unit cells. In evaluating $F_{\substack{n,0\\ a\ \ b}}$, the atoms are displaced to obtain the shortest distance consistent with the periodic boundary conditions.

The Hartree-Fock solution is obtained iteratively, starting with a diagonal density matrix constructed such that the atoms are neutral and the electron density is equally distributed among the orbitals on a given atom. The Hartree-Fock iterations continue until the largest change in any single Fock matrix element is less than one part in 10^{10}.

6.2.2 Wannier functions

The molecular orbitals of Eq. (6.9) may be written,

$$\left|\Psi^{(k)}_{band}\right\rangle = \frac{1}{\sqrt{N}}\sum_{n} e^{i\,k\,n}\left|W^{band}_{n}\right\rangle, \tag{6.12}$$

where $\left|W^{band}_{n}\right\rangle$ is the Wannier function centered on the n^{th} unit cell. In the atomic basis, these are given by,

$$\left|W^{band}_{n}\right\rangle = \sum_{m,a} w^{band}_{\substack{m-n\\ a}} \left|\begin{matrix} m\\ a\end{matrix}\right\rangle \tag{6.13}$$

$$w^{band}_{\substack{m\\ a}} = \frac{1}{N}\sum_{k} e^{ikm} e^{i\phi^{band}_{k}} C^{(k)}_{a,band} \tag{6.14}$$

The phase factor, $e^{i\phi^{band}_{k}}$, is included in Eq. (6.14) because the phase of the molecular orbitals, Eq. (6.9), may be chosen arbitrarily. For convenience, the Wannier functions are made real by choosing ϕ^{band}_{k} such that $e^{i\phi^{band}_{k}} C^{(k)}_{a,band}$ is the complex conjugate of

$e^{i\phi_{-k}^{band}} C_{a,band}^{(-k)}$. This leaves $\frac{(N-1)}{2}$ undetermined phases, which may be chosen to give a Wannier function of minimal size. For the PPP model of polyacetylene, Kertesz[59] showed that a Wannier function of minimal size is obtained by choosing equal and opposite phases for the two p-orbitals in the unit cell. We are not aware of an analytical solution for an arbitrary unit cell, and instead use a numerical approach. The size of the Wannier function is defined as,

$$Size = \sum_n n^2 \left| w_{\substack{n \\ a}}^{(band)} \right|^2 . \tag{6.15}$$

The ϕ_k^{band} that minimize the size are determined using the Simplex algorithm[60]. The resulting minimum is somewhat sensitive to the starting point, and we have found that the following procedure leads to well-localized Wannier functions. The size of the Wannier function of a dimerized one-dimensional chain is minimized when the "average phase" of the orbital coefficients is zero[59], where the phase being averaged does not include the sign change associated with nodes in the wavefunction. To generalize the concept of an "average phase", we first bring the coefficients for the various wavevectors into coarse alignment by identifying the orbital index, $a_{largest}$, for which $C_{a,band}^{k=0}$ has the largest norm, and then force $Re\left(C_{a_{largest},band}^{k}\right) > 0.0$ for all k by multiplying the wavefunctions by -1, when necessary. An average phase is then defined as,

$$\bar{\phi}_k^{band} = \frac{1}{S} \sum_a \arg\left((-1)^p \, C_{a,band}^{k}\right) \tag{6.16}$$

where the sum includes only those values of a for which $\left|C_{a,band}^{k}\right| > 0.1 \left|C_{a_{largest},band}^{k}\right|$, and S is the number of terms included in the sum. In calculating the average-phase, we are not interested in the 180^o phase shifts arising from nodes in the Wannier function. These shifts are removed via the $(-1)^p$ term of Eq. (6.16), with $p = 1$ if $Re\left(C_{a,band}^{k}\right) < 0$ and $p = 0$ otherwise. The starting point for the simplex algorithm is obtained by setting $\phi_k^{band} = -\bar{\phi}_k^{band}$.

The one and two electron Hamiltonian matrix elements are then transformed to the Wannier function basis. Transformation of the two electron matrix elements is accelerated by truncating the Wannier functions. The Wannier functions are peaked on the center, $n = 0$, unit cell and decay with increasing $|n|$. The Wannier function is truncated by setting $w^{(band)}_{\underset{a}{n}} = 0$ for $n > W_{cut}$, and then normalizing the resulting function. In the calculations presented below, W_{cut} was set to 5 unit cells, which was sufficient for convergence.

6.2.3 Configuration Interaction

In periodic boundary conditions, the single electron-hole pair basis functions may be written,

$$\Phi^{(K)}_{\underset{band}{0} \rightarrow \underset{band'}{\Delta}} = \frac{1}{\sqrt{N}} \sum_n e^{i\,K\,n} \psi_{\underset{band}{n} \rightarrow \underset{band'}{n+\Delta}} \tag{6.17}$$

where upper-case K is the wavevector of the many-body wavefunction (lower-case k is used for the molecular orbitals of Eq. (6.9)). $\psi_{\underset{band}{n} \rightarrow \underset{band'}{n'}}$ is a singlet electron-hole function, containing a hole in the valence band Wannier function on the n^{th} unit cell, $W^{(band)}_n$, and an electron in the conduction band orbital on the n'^{th} unit cell, $W^{(band')}_{n'}$. Note that, due to translational symmetry, only the separation between the electron and hole, Δ, is relevant. For convenience, we introduce the following notation for a general many-body basis function,

$$\left|\Phi^K_a\right\rangle = \frac{1}{\sqrt{N}} \sum_n e^{iKn} \left|a+n\right\rangle \tag{6.18}$$

where a labels a particular arrangement of electrons and holes and $|a+n\rangle$ indicates that these have been displaced by n unit cells.

The matrix elements of the Hamiltonian are then given by,

$$\begin{aligned} \left\langle\Phi^K_a \left|\hat{H}\right| GS\right\rangle &= \frac{1}{\sqrt{N}} \sum_\Delta e^{-iK\Delta} \left\langle a+\Delta\right| \hat{H} \left|GS\right\rangle \\ &= \sqrt{N} \left\langle a\right| \hat{H} \left|GS\right\rangle \delta_{K,0} \end{aligned} \tag{6.19}$$

and,

$$\left\langle\Phi^K_b\right| \hat{H} \left|\Phi^K_a\right\rangle = \left[\frac{1}{N} \sum_\Delta e^{iK\Delta} \left\langle b+\Delta\right| \hat{H} \left|a\right\rangle\right] \delta_{K,K} \tag{6.20}$$

where $|GS\rangle$ is the ground electronic state.

6.2.4 Transition moments

To obtain a transition moment operator that is consistent with the periodic boundary conditions, we use that for a ring of polymer with N unit cells[61, 62, 63]. We begin with a unit cell that lies (as much as possible) in the (x, y) plane and a Brillouin vector, $\mathbf{B}$, that lies along the x-axis. The vector $r_j^{(unit)}$ gives the position of the j^{th} atom in the unit cell with respect to the center of the unit cell. The center is chosen by bisecting the line that connects the first (left-most) atom of the unit cell to the corresponding atom of the next unit cell. A ring in the (x, z) plane is then formed by arranging the centers of the unit cells on a circle with radius,

$$R = \frac{|B|}{2\sin\left(\pi/N\right)}, \tag{6.21}$$

chosen such that the chord connecting the centers of the unit cells has length $|\mathbf{B}|$. The unit cells are rotated about the y-axis such that they are tangent to the ring. The x-coordinate of the j^{th} atom of the n^{th} unit cell is then given by

$$X_{\substack{n \\ j}} = x_j^{(unit)} \cos\left(\theta n\right) + \left(R - z_j^{(unit)}\right) \sin\left(\theta n\right), \tag{6.22}$$

where $\theta = \frac{2\pi}{N}$ (see text below eq. (6.9)).

It is convenient to introduce an operator, $\hat{\chi}$, which has the following matrix elements in the atomic basis,

$$\left\langle \begin{matrix} n \\ j \end{matrix} \middle| \hat{\chi} \middle| \begin{matrix} m \\ l \end{matrix} \right\rangle = \tag{6.23}$$

$$\frac{1}{2}\left(x_j^{(unit)} + i\left(-R + z_j^{(unit)}\right)\right)\delta_{n,m}\delta_{j,l}$$

The x-operator corresponding to Eq. (6.22) is then,

$$\hat{X} = \hat{\chi}e^{i\theta} + \hat{\chi}^{\dagger}e^{-i\theta} \tag{6.24}$$

The operator $\hat{\chi}$ is convenient because $\hat{\chi}$ raises the wavevector of a many-body state by θ, while $\hat{\chi}^{\dagger}$ lowers the wavevector by θ,

$$\left\langle \Phi_a^K \right| \hat{X} \left| GS \right\rangle = \tag{6.25}$$

$$\sqrt{N}\left[\langle a|\,\hat{\chi}\,|GS\rangle\,\delta_{K,K+\theta}+\langle a|\,\hat{\chi}^{\dagger}\,|GS\rangle\,\delta_{K,K-\theta}\right]$$

$$\left\langle \Phi_{b}^{K}\right|\hat{X}\left|\Phi_{a}^{K}\right\rangle = \tag{6.26}$$

$$\sum_{n}e^{-iKn}\left[\langle b+n|\,\hat{\chi}\,|a\rangle\,\delta_{K,K+\theta}+\langle b+n|\,\hat{\chi}\,|a\rangle^{\dagger}\,\delta_{K,K-\theta}\right]$$

The transition moment operator along the y-axis, perpendicular to the polymer axis, is diagonal in K and its evaluation is similar to that of the Hamiltonian, Eqs. (6.19) and (6.20).

The ring geometry is used only to obtain a periodic transition moment operator. As described in Sec. 6.2.1, the Hamiltonian parameters are those for a linear chain, and thus do not include curvature effects which would serve only to slow convergence to the long-chain limit. In generating spectra, it is useful to remove artifacts arising from the use of a ring geometry. For a ring in the (x, z)-plane, the absorption intensity due to transitions polarized parallel to the polymer axis is spread equally between the x and z axes, while that polarized perpendicular to the polymer axis lies only along the y axis. In the absorption spectra shown below, the parallel transition spectrum is multiplied by 2, so that in the long-chain limit, the relative intensities reflect those of a chain rather than a ring.

The C++ code used in these calculations is a general implementation of PPP and INDO calculations for both non-periodic and periodic systems. The non-periodic functionality was verified by comparison with the ZINDO program[27]. The periodic functionality was verified by comparison of state energies and both the linear and non-linear optical polarizabilities of a ring of polymer, calculated with and without the assumption of periodic boundary conditions.

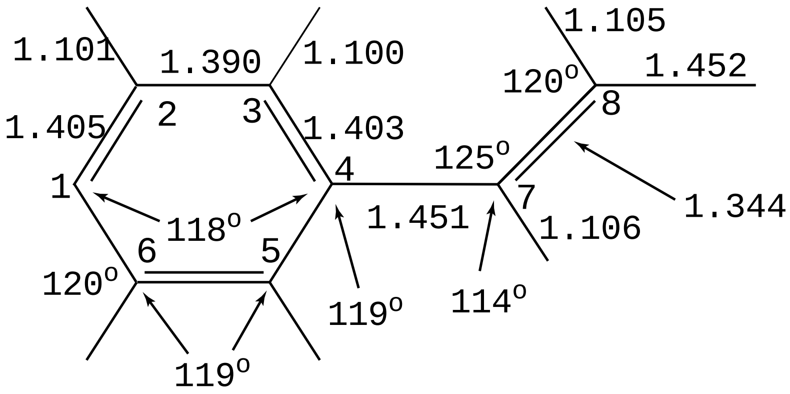

Figure 6.1: Geometry of a unit cell of PPV, extracted from an AM1 calculation on an oligomer with six phenyl rings and 5 double bonds, constrained to remain planar. Bond lengths are in Angstroms.

6.3 Results

6.3.1 Chemical Structures

The geometry of a unit cell of PPV and its derivatives was obtained from AM1 calculations[64] on an oligomer containing 6 phenyl rings connected by 5 *trans* double bonds. To allow for a rigorous separation of σ and π orbitals, we first constrained the geometry to remain planar. For unsubstituted PPV, this constraint has essentially no effect on the geometry, and its removal lowers the calculated heat of formation by less than 0.2 kcal/mole. The geometry of the unit cell, shown in Fig. 6.1, was obtained from the central double bond and an adjacent phenyl ring of the optimized oligomer structure.

As a simple model of MEH-PPV, or general alkoxy substituted PPV, we consider dihydroxy-PPV (OH-PPV) obtained through hydroxy substitution at the 2 and 5 positions of the phenyl ring in Fig. 6.1. The molecular geometries were obtained following the procedure outlined above for PPV. However, when the geometry of OH-PPV is constrained to be planar, the resulting energy is 9 kcal/mole higher than the energy obtained from an unconstrained geometry optimization. In the fully optimized structure, the vinylene bonds rotate out of plane by about 20^o. Results are presented below for both planar and fully-optimized, non-planar OH-PPV. The results for the

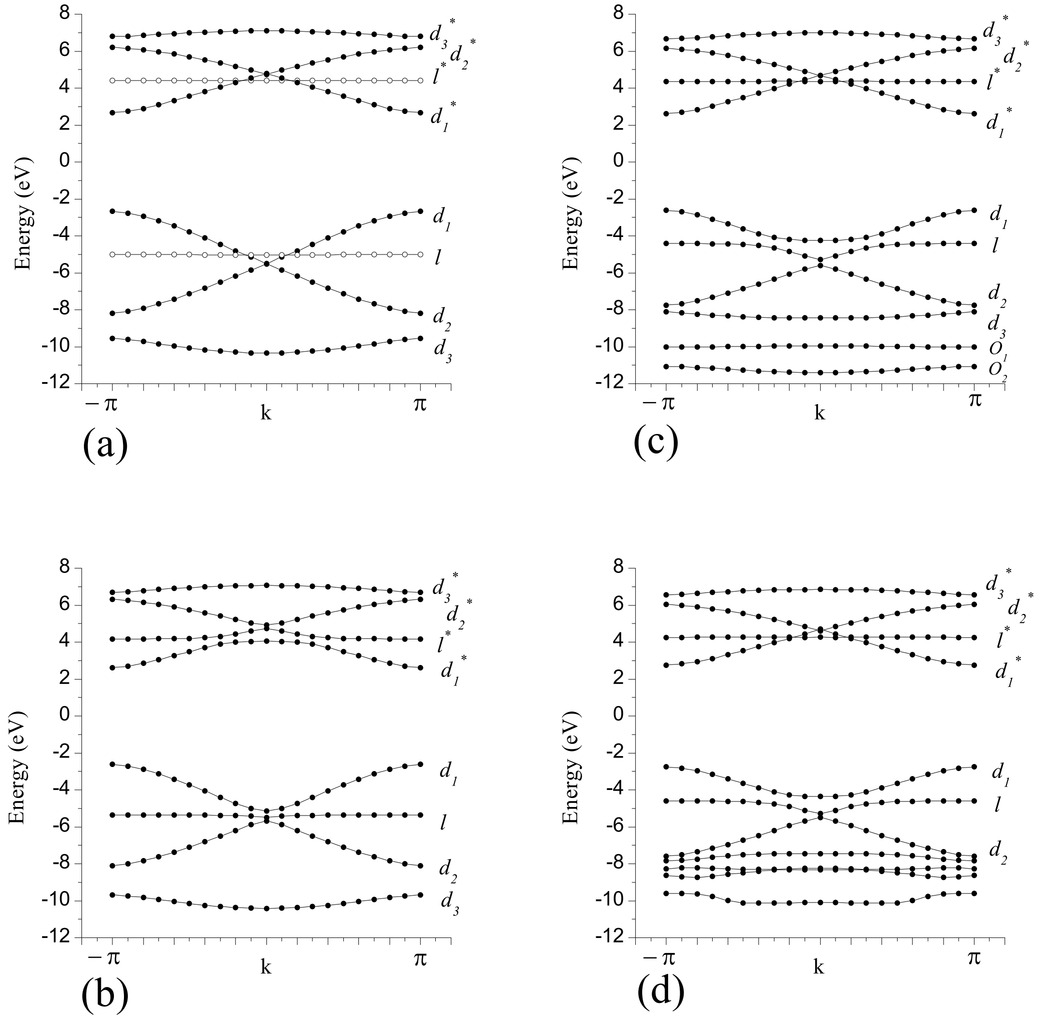

Figure 6.2: π band structure and band labels for (a) unsubstituted, planar PPV, (b) PPV with the p_z-orbitals on carbons 2 and 5 perturbed by -1 eV (subs-PPV), (c) planar di-hydroxy-PPV (OH-PPV), and (d) fully-optimized, non-planar OH-PPV.

planar structure show the effects of the hydroxy substitution, without the added complication of the σ-π orbital mixing that arises from the vinylene rotation. Replacing the hydroxy groups with methoxy groups (MeO-PPV) leaves the structure of the backbone essentially unchanged. Since the photophysical predictions for MeO-PPV are essentially identical to those of OH-PPV, below, we present a detailed analysis of the band structure and photophysics of the simpler OH-PPV system. In particular, OH-PPV is simpler because the methyl groups of MeO-PPV make the structure non-planar and prevent a rigorous separation of σ and π electrons.

The chemical structures of the oligomers studied below were obtained from AM1 geometry optimizations on oligomers with between 4 and 8 phenylene rings connected by $trans$-vinylenes.

6.3.2 Hartree-Fock band structure and Wannier functions

The π band structures of PPV and OH-PPV, obtained as described in Sec. 6.2.1 with N=21 unit cells, are shown in Fig. 6.2. The results for unsubstituted PPV are shown in Fig. 6.2(a). The flat bands are labeled l for localized, and the delocalized bands are labeled d_n with n increasing as one moves away from the Fermi energy. A $*$ is used to indicate conduction, as opposed to valence, bands.

Previous studies[52, 51], performed using a π-electron model, included the effects of alkoxy substitution by altering the energy of the p-orbital to which the substituent is attached. A similar approach can be implemented in the INDO Hamiltonian by adding a perturbation to the Hamiltonian of Sec. 6.2.1 that alters the energy of the $2p_z$ orbital on the respective carbon atoms. The results in Fig. 6.2(b) were obtained by subtracting 1 eV from the orbital energy of the p_z orbital on carbons 2 and 5 of PPV (Fig. 6.1). We will refer to this system as subs-PPV for substituted PPV.

Fig. 6.2(c) shows the π bands of planar OH-PPV. For a planar molecular geometry, such as in Figs. 6.2(a)-(c), there is a rigorous separation of σ and π orbitals, and only the π bands are shown. Such a separation is not rigorous for fully-optimized, non-planar OH-PPV, and the bands shown in Fig. 6.2(d) are those with the largest π content. Significant mixing of π and σ character occurs only in the four lowest-energy

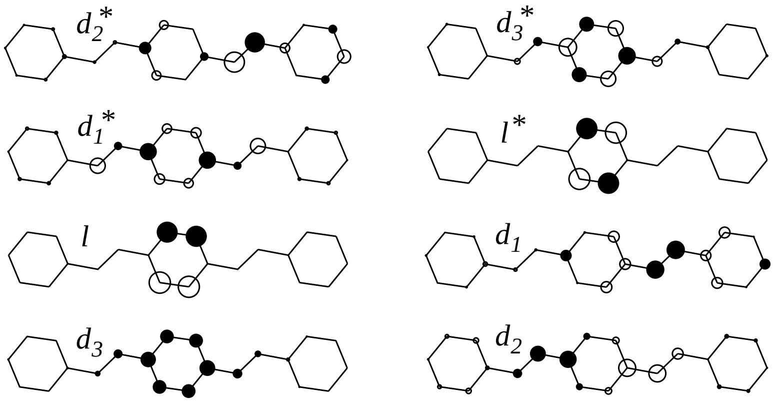

Figure 6.3: Wannier functions for the π-bands of PPV in Fig. 6.2(a). The sizes of the circles are proportional to the absolute value of the Wannier function on the p_z-orbital of that carbon. Open and closed circles indicate positive and negative values, respectively.

bands of Fig. 6.2(d).

The Wannier functions for the π bands of PPV and planar OH-PPV are shown in Figs. 6.3 and 6.4, respectively.

6.3.3 Singles-CI

Fig. 6.5 shows the absorption spectra from singles-configuration interaction (S-CI) calculations for the systems of Fig. 6.2. For the planar molecular structures of Figs. 6.5(a)-(c), there is no mixing of σ and π bands and the S-CI calculations include all π bands. For non-planar OH-PPV, Fig. 6.5(d), the calculation includes the 8 highest-energy valence and 6 lowest-energy conduction bands. Table 6.1 shows the contributions of various bands to the transitions labeled I through IV in Fig. 6.5.

Figs. 6.6 and 6.7 show spectra obtained from S-CI calculations on oligomers of PPV and OH-PPV. The oligomers contain between N=4 and N=8 phenyl rings, connected by trans-vinylenes. For N=4 through N=6, the S-CI basis was formed from all excitations between the 8N highest-energy filled molecular orbitals and the 6N lowest-energy empty molecular orbitals. For N=7 and N=8, the basis was formed from the 48 highest filled and 36 lowest empty orbitals. The labeling of the peaks is discussed in Sec. 6.4.

Table 6.1: State energies, oscillator strengths, and band composition for the states giving rise to peaks in the absorption spectra of Fig. 6.2. The band labels correspond to those of Fig. 6.2.

Peak	E	osc_x	osc_y	band composition
(a) planar, unsubstituted PPV				
I	3.0	100		99.3% $d_1 \rightarrow d_1^*$
II	4.0	0.2		63.3% $d_1 \rightarrow l^*$, 31.4% $l \rightarrow d_1^*$
II	4.0		0.7	63.3% $d_1 \rightarrow l^*$, 31.4% $l \rightarrow d_1^*$
III	5.4		21	59.0% $l \rightarrow d_1^*$, 36.4% $d_1 \rightarrow l^*$
IV	6.5	20		63.9% $l \rightarrow l^*$, 13.6% $d_1 \rightarrow d_2^*$, 9.31% $d_2 \rightarrow d_1^*$, 7.44% $d_1 \rightarrow d_1^*$
(b) planar PPV with the energy of carbon atoms 2 and 5 (Fig. 6.1) lowered by 1 eV				
I	2.9	100		98.4% $d_1 \rightarrow d_1^*$
II	4.0	7		67.0% $d_1 \rightarrow l^*$, 16.8% $l \rightarrow d_1^*$, 8.88% $d_1 \rightarrow d_1^*$
II	4.0		5	67.9% $d_1 \rightarrow l^*$, 17.0% $l \rightarrow d_1^*$, 7.62% $d_1 \rightarrow d_1^*$
III	5.5		7	65.5% $d_1 \rightarrow d_1^*$, 16.8% $d_1 \rightarrow l^*$, 15.3% $l \rightarrow d_1^*$
III	5.5		8	38.3% $d_1 \rightarrow d_1^*$, 36.6% $l \rightarrow d_1^*$, 20.7% $d_1 \rightarrow l^*$
IV	6.1		10	78.7% $d_1 \rightarrow l^*$, 12.6% $l \rightarrow d_1^*$, 6.59% $d_1 \rightarrow d_1^*$
IV	6.5	20		32.0% $l \rightarrow l^*$, 18.3% $d_1 \rightarrow l^*$, 12.8% $d_1 \rightarrow d_3^*$, 12.0% $d_1 \rightarrow d_2^*$, 9.43% $l \rightarrow d_1^*$, 9.19% $d_1 \rightarrow d_1^*$
IV	6.5	7		35.6% $d_1 \rightarrow l^*$, 16.6% $d_1 \rightarrow d_2^*$, 16.0% $d_1 \rightarrow d_3^*$, 12.1% $l \rightarrow l^*$, 6.51% $l \rightarrow d_1^*$, 6.46% $d_2 \rightarrow d_1^*$, 5.22% $d_1 \rightarrow d_1^*$
(c) planar di-hydoxy-PPV				
I	3.0	100		96.4% $d_1 \rightarrow d_1^*$
II	3.9	4		42.8% $l \rightarrow d_1^*$, 41.0% $d_1 \rightarrow l^*$, 10.7% $d_1 \rightarrow d_1^*$
III	5.1		50	52.2% $d_1 \rightarrow l^*$, 41.5% $l \rightarrow d_1^*$
IV	5.7	30		43.4% $l \rightarrow l^*$, 25.6% $d_1 \rightarrow l^*$, 16.4% $l \rightarrow d_1^*$, 11.5% $d_1 \rightarrow d_2^*$
(d) non-planar, di-hydroxy-PPV				
I	3.0	100		97.2% $d_1 \rightarrow d_1^*$
II	3.9	4		49.8% $d_1 \rightarrow l^*$, 35.4% $l \rightarrow d_1^*$, 6.39% $d_1 \rightarrow d_1^*$
III	5.1		30	44.5% $l \rightarrow d_1^*$, 34.3% $d_1 \rightarrow l^*$, 18.3% $d_1 \rightarrow d_1^*$
IV	5.7	30		45.9% $l \rightarrow l^*$, 29.2% $d_1 \rightarrow l^*$, 11.4% $d_1 \rightarrow d_2^*$, 7.47% $l \rightarrow d_1^*$

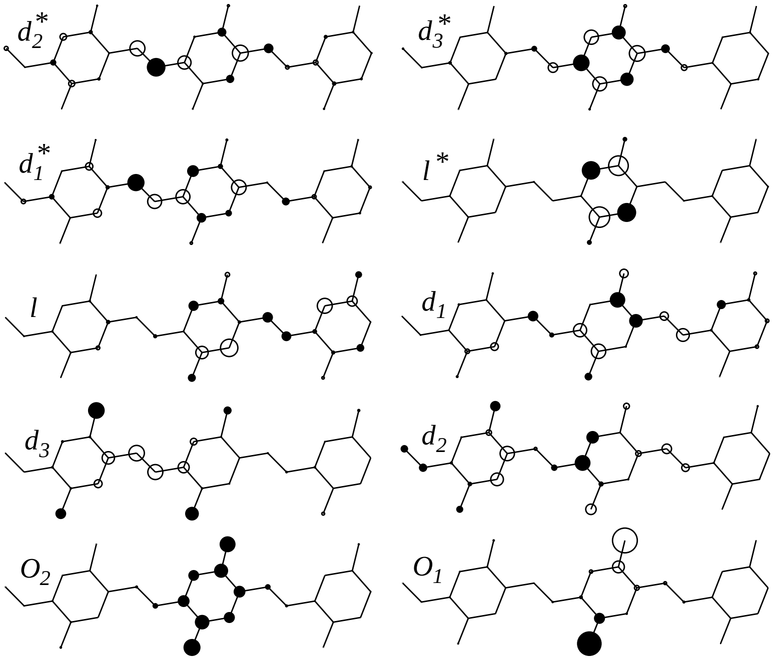

Figure 6.4: Wannier functions of the π-bands of planar di-hydroxy-PPV (OH-PPV) in Fig. 6.2(c).

6.4 Discussion

The experimental absorption spectrum[52, 53, 54, 55, 56] of PPV exhibits strong transitions at about 2.4 eV, 4.7 eV and 6 eV. A transition at about 3.7 eV is observed in substituted PPV samples, with an intensity that is roughly equal to that of the transition at 4.7 eV. We will refer to these transitions as I (2.4eV), II (3.7 eV), III (4.7 eV) and IV (6.0 eV). Transitions I and IV are polarized parallel to the polymer axis and transition III is polarized perpendicular to the polymer axis. Transition II appears to be primarily polarized parallel to the polymer axis[52, 54, 55].

In previous theoretical studies[49, 51, 52], there is general agreement that peak I consists of an excitation from the highest valence to the lowest conduction band, $d_1 \rightarrow d_1^*$, and that peak IV arises from a transition between the localized valence and conduction bands, $l \rightarrow l^*$. Similar results are obtained here from INDO calculations on long-chains of PPV with periodic boundary conditions. For both unsubstituted and substituted PPV, Table 6.1 indicates that peak I is greater than 95% $d_1 \rightarrow$

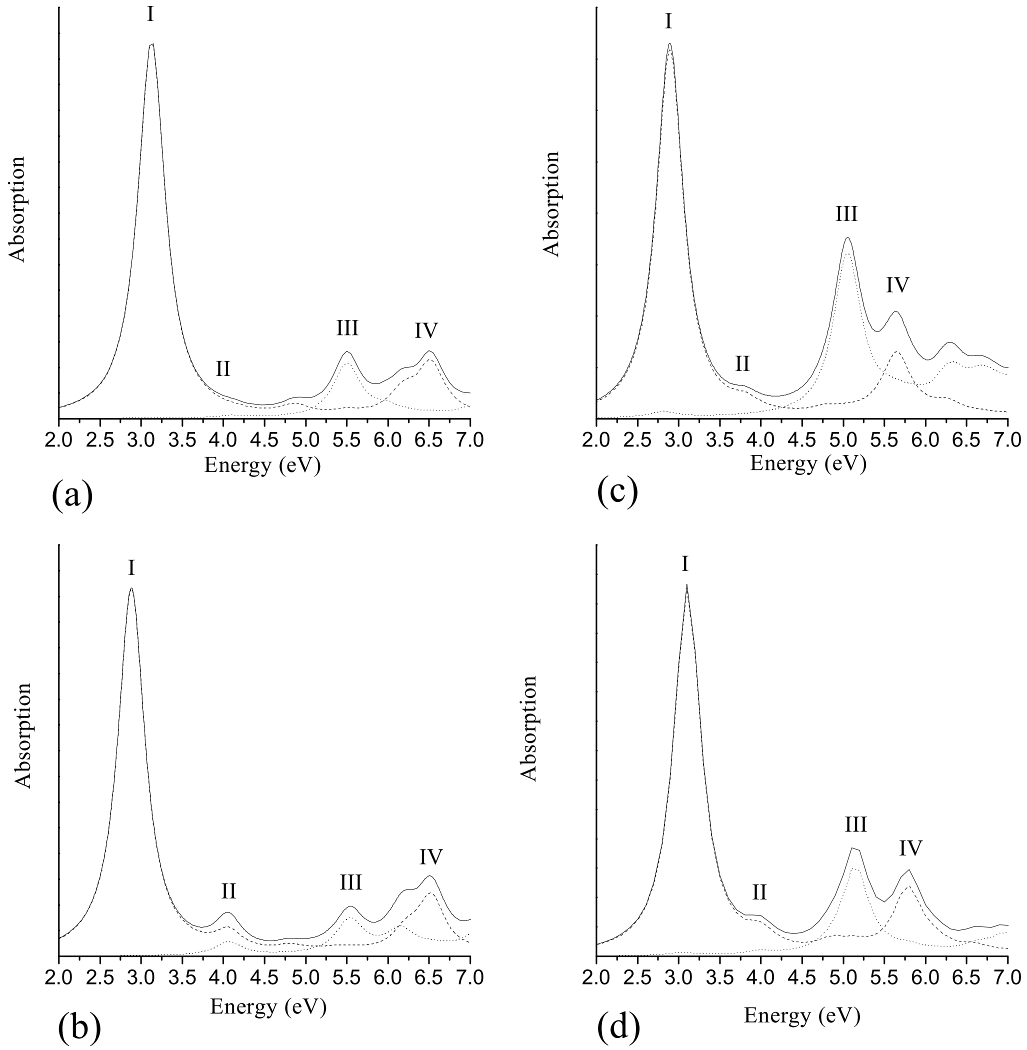

Figure 6.5: Absorption spectra of (a) unsubstituted, planar PPV, (b) PPV with the p_z-orbitals on carbons 2 and 5 perturbed by -1 eV (subs-PPV), (c) planar di-hydroxy-PPV (OH-PPV), and (d) fully-optimized, non-planar OH-PPV. The solid line is the total absorption spectrum, the dotted line is absorption polarized perpendicular to the chain axis, and the dashed line is absorption polarized parallel to the chain axis. The peaks are labeled according to the discussion in Sec. 6.4.

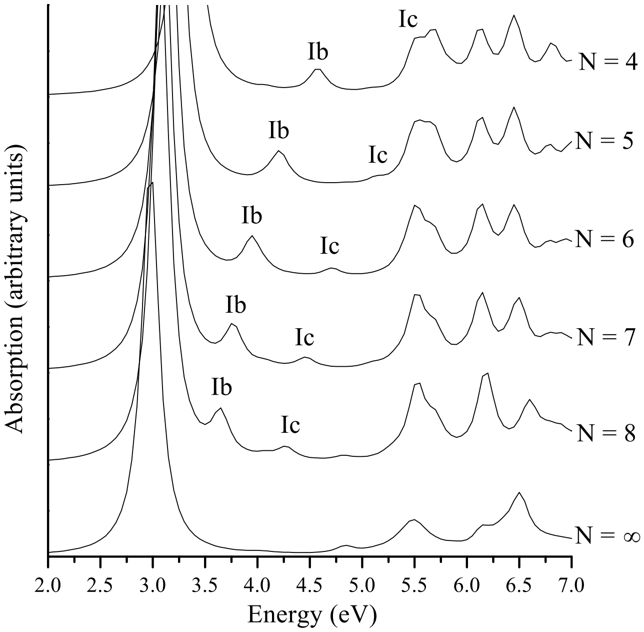

Figure 6.6: Absorption spectrum of oligomers of PPV, consisting of N phenyl rings connected by trans-vinylene groups. $N{=}\infty$ denotes the long-chain limit, obtained from a calculation on 21 unit cells with periodic boundary conditions (as in Fig. 6.5). The peaks are labeled according to the discussion in Sec. 6.4, with peaks Ib and Ic converging to peak I in the limit of a long chain. The oligomer spectra are divided by the number of phenylene units, N, such that the intensities are comparable. The intensity of the long-chain spectrum is adjusted such that the peak III intensity is equal to the average of that seen for the oligomers.

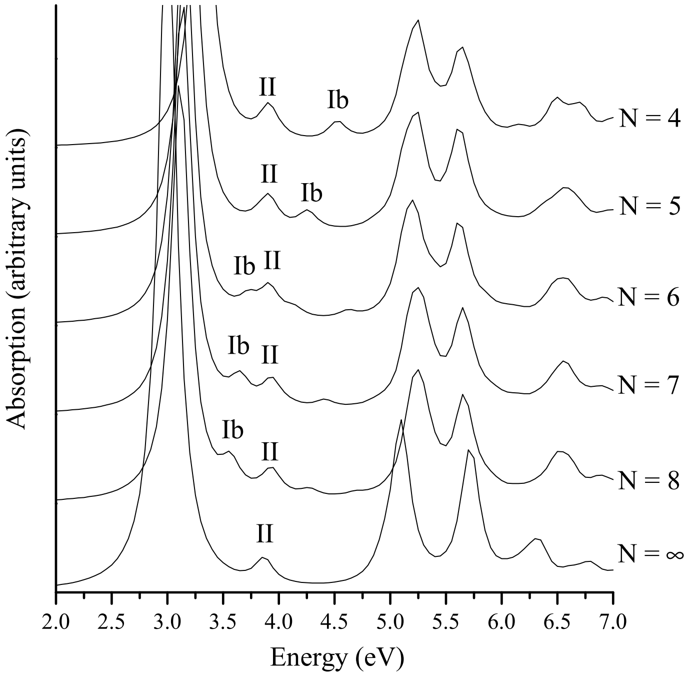

Figure 6.7: Absorption spectrum of oligomers of fully-optimized, non-planar dihydroxy-PPV (OH-PPV). The notation is as in Fig. 6.6.

d_1^* in character. Although the calculated transition energy of 3.0 eV is somewhat higher than the experimentally observed 2.4 eV, this is perhaps expected since these calculations are for an isolated chain and dielectric effects present in the solid-state are expected to lead to a red-shift of a few tenths of an eV[65, 32]. The INDO calculations also support the assignment of peak IV to $l \to l^*$, although there are 35% contributions from other configurations in PPV and this increases to 55% in OH-PPV. This increase likely reflects the mixing between localized and delocalized bands seen in Fig. 6.2(c). Overall, the INDO results for peaks I and IV are consistent with past work.

Peaks II and III are typically assigned to states arising from the $l \to d_1^*$ and $d_1 \to l^*$ excitations; however, the details of these assignments differ[51, 52]. A central issue is the breaking of electron-hole symmetry, also known as alternancy or charge-conjugation symmetry[39]. Electron-hole symmetry is present for π-electron models that include only nearest neighbor transfer integrals, such as Hückel or Parriser-Parr-Pople (PPP) theory[14], and chemical structures that are alternant. In an alternant chemical structure, only carbon atoms participate in the π-electronic structure and these carbons may be divided into two disjoint sets, $\{A\}$ and $\{B\}$, such that no carbon atom is bonded to another carbon atom in the same set[39]. When alternancy symmetry applies, the valence and conduction band orbitals form pairs with energies distributed symmetrically about the Fermi energy. Since PPV is an alternant structure, Hückel or Parriser-Parr-Pople (PPP) theory yields bands that exhibit electron-hole symmetry. In these models, the band structure resembles that of Fig. 6.2(a) but with bands d_1 and d_1^* being perfect mirror images of one other and likewise for the other bands. (The slight breaking of this symmetry in Fig. 6.2(a) is discussed below.) In models with electron-hole symmetry, the configurations formed from an $l \rightarrow d_1^*$ excitation are degenerate with those formed from $d_1 \rightarrow l^*$. In Hückel theory, this leads to two overlapping transitions with an energy half-way between that of peaks I and IV. In a model such as PPP theory that includes electron-electron interactions, there is a significant coupling between these two configurations. This configuration interaction leads to in-phase and out-of-phase combinations of $l \rightarrow d_1^*$ and $d_1 \rightarrow l^*$. The estimated splitting between these in-phase and out-of-phase combinations is sufficient to account for states at the positions of peaks II and III; however, only the upper state is predicted to carry optical intensity. Models with electron-hole symmetry can therefore account for peak III and for a state with an energy appropriate for peak II; however, they cannot account for the observed intensity in peak II.

It has been suggested that chemical substitution, such as in MEH-PPV, may break charge conjugation symmetry and thus account for the intensity in peak II[51, 52]. Here, we examine this and other symmetry breaking mechanisms. In examining these mechanisms, we consider their effects on the relative intensities of peaks II and III (see Table 6.2). In the experimental spectrum of substituted PPV's, these two peaks have roughly equal intensity[52, 53, 54, 55, 56].

While Hückel and PPP theory include one-electron matrix elements only between adjacent atoms, the INDO Hamiltonian includes one-electron matrix elements between all atoms, Eq. (6.1). This breaks electron-hole symmetry and causes the va-

Table 6.2: Ratios of intensities for selected peaks in the spectra of Figs. 6.5, 6.6, and 6.7.

Periodic calculations

Unsubstituted PPV	Intensity peak II : peak III	OH-PPV	intensity peak II : peak III	OMe-PPV	intensity peak II:III
planar	1 : 24.0	planar	1 : 12.2		
Non-planar	1 : 26.7	non-planar	1 : 7.0	non-planar	1:8.9
subs-PPV	1 : 1.10				

OH-PPV Oligomers

Number of rings in the OH-PPV oligomer	intensity peak II : peak III	intensity peak Ib : II
4	1 : 3.96	1 : 1.47
5	1 : 4.26	1 : 1.48
6	1 : 3.81	1 : 1.86
7	1 : 3.88	1 : 1.06
8	1 : 4.43	1.18 : 1

MeO-PPV Oligomers

Number of rings in the MeO-PPV oligomer	intensity peak II : peak III	intensity peak Ib : II
4	1 : 4.90	1 : 1.16
5	1 : 6.63	1.29 : 1
6	1 : 4.78	1 : 1.47
7	1 : 5.07	1.16 : 1
8	1 : 4.44	1.32 : 1

lence bands to be wider than the conduction bands in Fig. 6.2(a). The breaking of electron-hole symmetry is also apparent in the Wannier functions of Fig. 6.3. As discussed above, an alternant chemical structure is one where it is possible to divide the carbons into two disjoint sets, {A} and {B}, such that no carbon atom is bonded to another carbon atom in the same set. When electron-hole symmetry applies, the valence and conduction band orbitals are related by changing the sign of the wavefunction on one of these sets, {A} or {B}. This is the case for the relatively flat bands, d_3, d_3^* and l, l^*. However, the other bands, including the highest valence and lowest conduction bands, deviate rather strongly from this particle-hole symmetry behavior. While this symmetry breaking does give some intensity to peak II in Fig. 6.5(a), the ratio of intensities for peak II to peak III is 1:24 (Table 6.2), as compared to the roughly equal intensities seen experimentally.

Considerably larger effects from electron-hole symmetry breaking are seen in the band structure of planar 2,5 dihydroxy-PPV (OH-PPV), Fig. 6.2(c). The lone pairs on the oxygens of the hydroxy substituents add two additional valence bands to the π-band structure and these are labeled O_1 and O_2 in Fig. 6.2(c). There is also substantial mixing of the delocalized and localized valence bands, and this mixing is not mirrored in the conduction bands. Comparison of the Wannier functions of OH-PPV (Fig. 6.4) with unsubstituted PPV (Fig. 6.3) also reveals significantly stronger effects from electron-hole symmetry breaking. In unsubstituted PPV, the Wannier functions for bands d_3 and l are related to those of d_3^* and l^* by electron-hole symmetry. In OH-PPV, none of the bands are paired in this manner. The absorption spectrum of Fig. 6.5(c) shows a weak peak II, with polarization parallel to the polymer axis and an intensity ratio with peak III of 1:12 (see Table 6.2). Table 6.1 indicates that, in addition to the expected $l \rightarrow d_1^*$ and $d_1 \rightarrow l^*$ excitations, peak II has an 11% contribution from $d_1 \rightarrow d_1^*$. This may result form the substitution-induced mixing between the localized and delocalized bands.

The band structure and absorption spectrum of fully-optimized, non-planar OH-PPV are shown in Figs. 6.2(d) and 6.5(d), respectively. In the optimized structure, the vinylene bonds are rotated out of plane by about 20^o, which can lead to mixing of σ and π bands. While the conduction and highest valence bands are similar to those of the planar structure, significant differences are seen in the lower-energy valence bands. In the absorption spectrum, peak II retains roughly the same intensity as for the planar structure, but peak III loses intensity such that the ratio of the intensities is 1:7 (see Table 6.2). A similar behavior is seen in the band compositions of Table 6.1. While the band composition of peak II stays roughly the same as for the planar structure, peak III gains about 18% $d_1 \rightarrow d_1^*$ character. In OH-PPV, the rotation of the vinylene by 20^o has a significant effect on the intensity ratio of peak II:peak III, which is 1:12 for the planar structure and 1:7 for the nonplanar structure. In unsubstituted PPV, a rotation of the vinylene by 20^o has a much smaller effect, changing the ratio from 1:24 to 1:27 (see Table 6.2).

As discussed in Sec. 6.3.2, π-electron models may include the effects of chemical substitution by altering the energy of the p_z-orbital on the carbon atom to which the substituent is attached[52, 51]. We can apply a similar perturbation in INDO theory, and Figs. 6.2(b) and 6.5(b) show the band structure and spectrum obtained in INDO theory when the energy of the p_z-orbitals on carbons 2 and 5 of Fig. 6.1 are lowered by 1 eV. We will refer to this model as subs-PPV, and compare the results

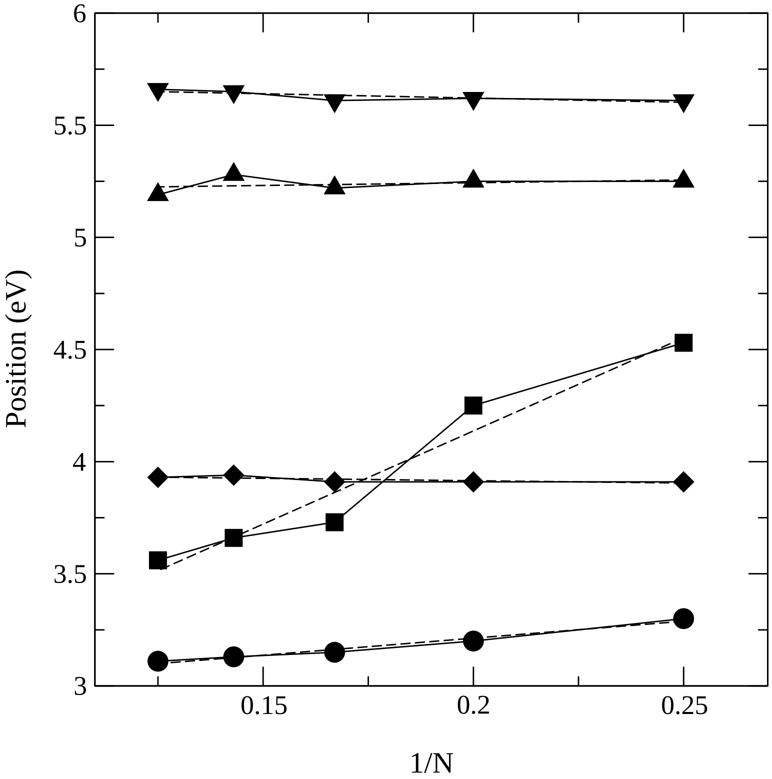

Figure 6.8: Energies of the states giving rise to peaks in the spectra of fully-optimized, non-planar OH-PPV (Fig. 6.7), versus $1/N$ where N is the number of phenylene units in the oligomer. The solid lines connect the points, and the dotted lines show the results of a linear regression. The linear regression gives infinite chain limits of: peak I (circles) 2.91 eV; peak Ib (squares) 2.48 eV; peak II (diamonds) 3.96 eV; peak III (upward-pointing triangles) 5.19 eV; and peak IV (downward-pointing triangles) 5.70 eV.

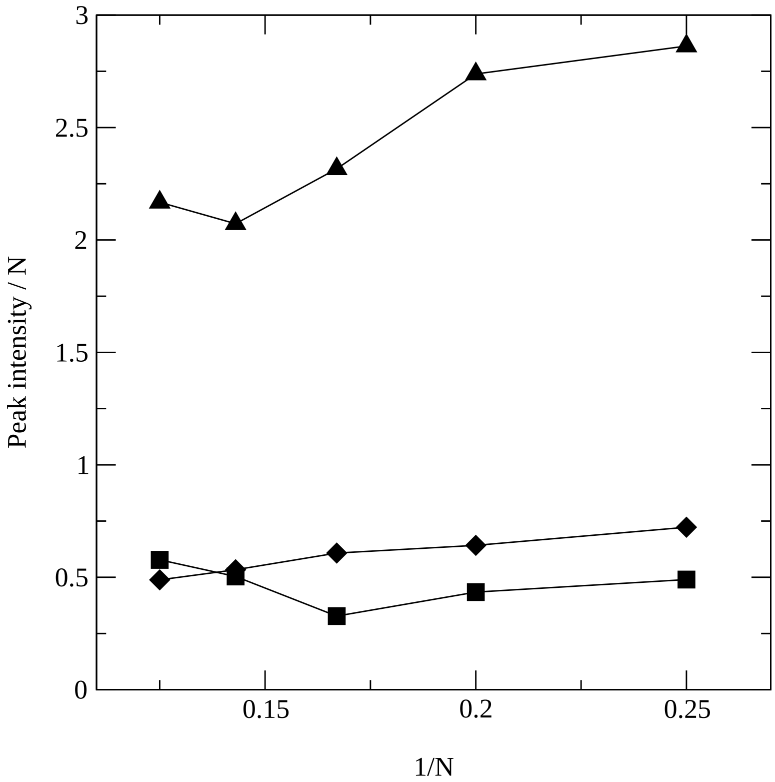

Figure 6.9: Oscillator strengths (intensities) for the states giving rise to peaks in the spectra of fully-optimized, non-planar OH-PPV. The notation is as in Fig. 6.8. The intensities are shown on a per-unit-cell basis, by dividing by the oligomer length, N.

with OH-PPV to determine how well this approach models the effects of chemical substitution. Comparison of the band structure of subs-PPV and OH-PPV reveals some substantial differences. In OH-PPV, mixing between localized and delocalized bands occurs primarily within the valence bands, while in subs-PPV, mixing occurs in both the valence and conduction bands and is a bit stronger in the conduction bands. Despite these differences, the overall magnitude of the mixing between bands appears fairly similar between subs-PPV and OH-PPV. It is therefore somewhat surprising that the spectrum of subs-PPV shows roughly equal intensity for peaks II and III. Also, peak III has greater than 50% character for $d_1 \rightarrow d_1^*$ excitations. In summary, the subs-PPV model breaks electron-hole symmetry and gives peak II substantial intensity, but the details of the symmetry breaking do not agree with the results obtained for the actual chemical substitution of OH-PPV. This indicates that perturbing the energy of p-orbitals is not a good model of chemical substitution.

Although the subs-PPV model is quite similar to the π-electron models used by Gartstein *et al*[51] and Chandross *et al*[52], there are some significant differences in the results. The model of Gartstein *et al*[51] predicts that peak II is polarized perpendicular to the polymer axis while the model of Chandross *et al*[52] predicts the polarization is parallel to the polymer axis. For the subs-PPV model, peak II is polarized roughly 50% perpendicular and 50% parallel to the polymer axis (Fig. 6.5 (b)). Note that in OH-PPV, peak II is polarized parallel to the polymer axis, and so the perpendicular component appears to be an artifact of the subs-PPV model. Gartstein *et al*[51] also predict peaks II and III to have roughly equal intensity in the limit of long chains, while Chandross *et al*[52] predict peak II to have substantial intensity on oligomers but vanishing intensity in the long-chain limit. The subs-PPV model predicts peaks II and III to have equal intensity on long chains. But again, the large intensity in peak II is an artifact of the subs-PPV model, and peak II is predicted to be weak for long chains of planar OH-PPV.

Finite-size effects are examined in Figs. 6.6 and 6.7, which compare the spectrum of oligomers with between 4 and 8 phenyl rings with the spectrum obtained in the limit of long chains. Fig. 6.6 shows that oligomers of PPV exhibit two new peaks, labeled Ib and Ic, that approach peak I as the chain length is increased. We attribute these transitions to states that have the same excitation as is present in peak I, but with higher kinetic energy, i.e. they are higher particle-in-a-box states of the same exciton that is present in peak I. These transitions will not be resolved in experiments on amorphous samples, since amorphous samples contain a distribution of effective conjugated lengths. The location of these peaks changes rapidly with chain length and the average over the effective conjugation lengths will lead to a broad spectrum that will appear as a background in the experimental spectrum.

OH-PPV also shows a peak, labeled Ib in Fig. 6.7, that approaches peak I with increasing chain length. However, unlike PPV, OH-PPV also exhibits peak II with a position that is relatively independent of chain length. The energies of the states that give rise to the peaks in Fig. 6.7 are plotted against $\frac{1}{N}$ in Fig. 6.8. The results show that peak Ib is converging onto I in the long chain limit, while the other peaks are relatively independent of chain length. Fig. 6.8 also suggests that as the state responsible for peak Ib crosses that responsible for peak II, it interacts and is repelled. This raises the possibility that, as suggested by Chandross *et al*[52], peak II may be borrowing intensity from Ib. However, Fig. 6.9, which plots the intensities of peaks Ib, II and III against $\frac{1}{N}$, shows little effect of the crossing of peaks Ib and II on the intensities. This argues against peak II borrowing intensity from peak Ib.

Fig. 6.7 and Table 6.2 show that finite-size effects nearly double the intensity of peak II relative to peak III. For non-planar OH-PPV, the intensity ratio of peak II to peak III is about 1:4 for oligomers and 1:7 in the long chain limit.

To determine the validity of OH as a general model of alkoxy substitution, calculations were also done on a series of di-methoxy substituted PPVs, (MeO-PPV). There is no visible difference in the OH-PPV and MeO-PPV spectra, in both the periodic and oligomer calculations. The intensities of the peaks change somewhat (Table 6.2), but the conclusions obtained above for OH-PPV still apply.

6.5 Conclusion

The calculations presented here examine a number of factors that break electron-hole symmetry and so give intensity to peak II. In all cases, the predicted polarization of peak II is parallel to the polymer axis, in agreement with experiment[52, 54, 55]. The results are summarized in Table 6.2, which lists the ratio between the intensities of peak II and peak III. The next-nearest neighbor transfer integrals present in INDO theory cause the conduction bands to be narrower than the valence bands, and this small breaking of electron-hole symmetry leads to an intensity ratio of 1:24. Chemical substitution, modeled here as 2,5 di-hydroxy-PPV (OH-PPV), leads to strong mixing between localized and delocalized valence bands. For a planar OH-PPV structure, the predicted intensity ratio is 1:12. However, AM1 calculations on OH-PPV indicate that the vinylene group rotates out of the plane of the phenyl rings by about 20^o, and this changes the intensity ratio to 1:7. Finite size effects further increase the intensity of peak II relative to peak III, giving an intensity ratio of about 1:4 for oligomers with between 4 and 8 phenyl rings. While this intensity ratio is still somewhat smaller than the experimentally observed ratio of about 1:1[52, 53, 54, 55, 56], the results presented here indicate that chemical substitution, combined with the finite conjugation lengths present in amorphous samples, leads to substantial electron-hole symmetry breaking and gives considerable intensity to peak II.

6.6 Acknowledgments

This work was funded by the National Science Foundation CHE9985719.

Chapter 7

Electron-hole symmetry breaking in carbon nanotubes due to next nearest neighbor interactions

7.1 Introduction

Carbon nanotubes have been actively studied since their initial discovery in 1991.[66] Of particular interest are the conduction properties of carbon nanotubes, which vary from metallic to semiconducting depending on subtle changes in the structure. This, and other features of the electronic structure, have been studied using tight-binding (Hückel) models.[67, 68, 69, 70, 71, 72, 73] These tight-binding models include only nearest-neighbor transfer terms, and the resulting electronic structure exhibits electron-hole symmetry. Here, we develop a simple means for including next-nearest-neighbor (NNN) electron transfer terms in tight-binding models of fullerenes. Such terms break electron-hole symmetry, and the effects of this symmetry breaking on the band gap and thermopower are examined.

The inclusion of next nearest neighbor terms has been found to be important in the calculation of a number of chemical properties.[74]-[75] The addition of the next nearest neighbor hopping has been shown to modify some of the energy gaps in C_{60}.[2] Kim and Wu have also found that a simple π-electron tight-binding model can explain

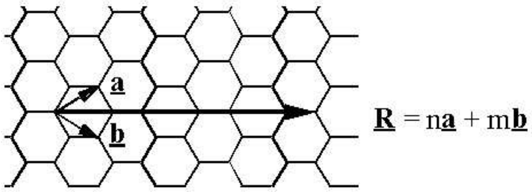

Figure 7.1: A portion of a graphite sheet showing the location of the lattice unit vectors $\hat{a}$ and $\hat{b}$ and the characteristic armchair tube wrapping vector $\vec{R}$ for $m = n$. The diameter of the resulting tube would be $D = \frac{|\vec{R}|}{\pi}$.

the low-energy excitation spectra of C_{60} only if next nearest neighbor terms and on-site electron-electron interactions are included.[76] Next nearest neighbor terms have also been shown to have significant effects on the band structure of polydiacetylene.[74] The inclusion of next nearest neighbor terms has also been used in the investigation of the metal-insulator transition in materials and has been shown to be important in the investigation of cuprate superconductors.[77]-[75] Judging by this previous work on conjugated carbon systems, it seems that the inclusion of these next nearest neighbor terms is necessary in the treatment of systems where the ratio between nearest-neighbor and the next-nearest-neighbor hopping integrals is relatively large, as is the case in the fullerenes, and graphene type structures.

A nanotubes may be viewed as a graphite sheet that has been wrapped into a tube structure and capped at the ends by curved fullerene structures. The orientation of the carbon-carbon bonds in the tube can be described by defining a wrapping vector ($\vec{R}$) that lies perpendicular to the tube axis, and has a length that is equal to the circumference of the tube. This vector may be written as a linear combination of the lattice vectors ($\hat{a}$ and $\hat{b}$) of the graphite sheet $\vec{R} = m\hat{a} + n\hat{b}$. The integer coefficients (m, n) provide a convenient notation for the tube structure. The electronic structure of nanotubes can be understood in terms of the band structure of a graphite sheet, with the introduction of periodic boundary conditions that take into account the finite circumference of the nanotube. These periodic boundary conditions serve to quantize the crystal momentum perpendicular to the tube, and each allowed value of the crystal momentum gives rise to a separate one-dimensional band of the nanotube.

Nanotubes can be divided into general classes based on the orientation of $\vec{R}$ (Figure 7.2) and the general electronic properties of that tube type as predicted by tight-binding methods. Figure 7.2(a) is referred to as an armchair, or perpendicular, type of tube ($m = n$ in $\vec{R}$). Using a one-dimensional, tight-binding model with only nearest neighbor hopping, armchair tubes have been predicted to have metallic properties.[68, 69, 70, 71, 72, 73] The remaining two general classes of tubes occur when $m \neq n$. Figure 7.2(b) is a zigzag or parallel tube ($n = 0$), which is predicted to be metallic for m an integer multiple of 3 and semi-conducting otherwise.[70] The last type (Figure 7.2(c)) is an example of a chiral tube ($m \neq n \neq 0$), in which the carbon-carbon bonds have an orientation between that in the armchair and the zigzag tube. Chiral tubes are predicted to be semiconducting.

7.2 Hückel Theory and Graph Theory

The Hückel Hamiltonian is a π electron model that includes one p-orbital for each carbon atom (site) and allows electron transfer between adjacent sites,

$$\mathbf{H} = \mathbf{H}_{\mathbf{on-site}} + \mathbf{H}_{\mathbf{nearest-neighbor}}, \tag{7.1}$$

or in terms of creation and annihilation operators,

$$\hat{H}^{H\ddot{u}ckel} = \sum_{i,\sigma} \alpha a^{\dagger}_{i,\sigma} a_{i,\sigma} + \sum_{i \neq j,\sigma} \beta_{i,j} a^{\dagger}_{i,\sigma} a_{j,\sigma}, \tag{7.2}$$

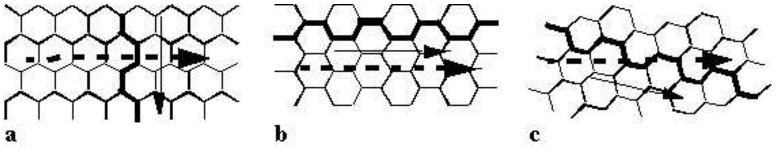

Figure 7.2: A portion of a graphite sheet showing the orientation of the carbon-carbon bonds for the three general classes of nanotubes. Tube (a) is an armchair tube, tube (b) a zigzag or parallel tube, and tube (c) is a chiral tube. The dashed arrow shows the direction of the tube axis. The bold series of carbon-carbon bonds and solid arrow serve to illustrate how the orientation of the bonds differs in the tubes.

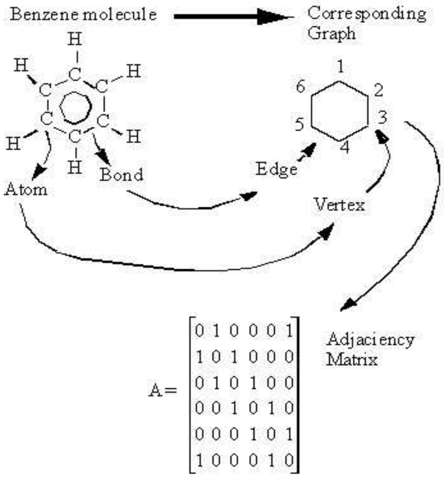

Figure 7.3: The benzene molecule, its graph representation, and the resulting adjacency matrix.

where σ is the electron spin, i,j are atomic sites, $a^{\dagger}(a)$ is the creation (annihilation) operator on the i^{th} carbon atom, α is the on-site potential, and β is the electron transfer integral. In the basis of p-orbitals, the Hückel models leads to a matrix of the form

$$\langle i| \hat{H}^{Hückel} |i\rangle = \alpha \tag{7.3}$$

$$\langle i| \hat{H}^{Hückel} |j\rangle = \begin{cases} \beta(r) & \text{if atoms } i \text{ and } j \text{ are bonded} \\ 0 & \text{otherwise} \end{cases}, \tag{7.4}$$

where r is the bond length.

Chemical graph theory provides a convenient approach to Hückel theory, as in the general methods of [78] and [79]. The molecule may be represented by a simple, unoriented graph, which consists of only vertices and edges, *i.e.*, lines and points (see Figure 7.3 for an example). In fact, the way in which the structural formula of a molecule is normally represented by the chemist is essentially a chemical graph, where the vertices of the graph are the atoms and the edges are the chemical bonds.

A listing of which atoms (vertices) are connected by bonds (edges) can be found in the vertex adjacency matrix (hereafter adjacency matrix) of the graph, **A** (see

Figure 7.3),

$$\mathbf{A}_{\mathrm{i,j}} = \begin{cases} 1 & \text{if atoms i and j are bonded} \\ 0 & \text{otherwise} \end{cases} . \tag{7.5}$$

In a system where all bond lengths are equal, the nearest neighbor hopping terms, $\beta(r)$ of eq. (7.4), are all equal and the Hückel matrix can be rewritten as a combination of the identity matrix, **I** and adjacency matrices of the chemical graph,

$$\mathbf{H} = \alpha \mathbf{I} + \beta \mathbf{A} \ , \tag{7.6}$$

Since **H** and **A** commute, they share the same set of eigenvectors[79, 78, 79, 80]. The molecular orbital energies are the eigenvalues of the Hückel matrix and may be written,

$$E_k = \alpha + \beta a_k, \tag{7.7}$$

where a_k is the k^{th} eigenvalue of the adjacency matrix.[81]

7.3 Addition of Next Nearest Neighbor Terms

With the inclusion of next nearest neighbor terms, the Hückel matrix has the form,

$$\langle i| \hat{H}^{H\ddot{u}ckel} |i\rangle = \alpha \tag{7.8}$$

$$\langle i| \hat{H}^{H\ddot{u}ckel} |j\rangle = \begin{cases} \beta(r) & \text{if atoms i and j are bonded} \\ \gamma(r) & \text{if i and j are next nearest neighbors} \\ 0 & \text{otherwise} \end{cases} . \tag{7.9}$$

In benzene, C_{60}, and infinite nanotubes, not only are all bond lengths equal, but the distance between next nearest neighbor carbon atoms is also equal. This means that $\beta(r)$ and $\gamma(r)$ have the same value for all pairs of atoms. The next-nearest neighbor terms of the Hückel matrix of eq. (7.8) may then be written in terms of the square of the adjacency matrix, similar to the way the nearest-neighbor terms were added using the adjacency matrix in eq. 7.6. When squaring the adjacency matrix, the off-diagonal terms are 1 if and only if the two vertices are connected by a path of length two, or equivalently, are bonded to a common atom (see Figure 7.4 for an example). The diagonal elements of $\mathbf{A^2}$ count the number of paths of length two that originate and terminate on the corresponding vertex. This is equal to degree of the vertex, or the number of bonds on a particular atom (2 for benzene, and 3 for C_{60}, and infinite nanotubes). The matrix elements of $\mathbf{A^2}$ are given by,

$$\left(\mathbf{A}_{i,j}\right)^2 = \begin{cases} n & \text{if } i = j \\ 1 & \text{if there is a path of length 2 between } i \text{ and } j \text{, with } i \neq j \\ 0 & \text{otherwise} \end{cases} , \quad (7.10)$$

where n is the degree of the vertices. The Hückel matrix of eq. (7.9) may then be written,

$$\mathbf{H} = (\alpha - n\gamma)\,\mathbf{I} + \beta\mathbf{A} + \gamma\mathbf{A}^2. \quad (7.11)$$

where $-n\gamma\mathbf{I}$ serves to cancel the diagonal matrix elements of $\mathbf{A^2}$ in eq. (7.10).

As we saw in the previous section, since $\mathbf{I}$, $\mathbf{A}$ and $\mathbf{H}$ commute, they have common eigenvectors and therefore the molecular orbital energies were simply related to the eigenvectors of the $\mathbf{A}$ (eq. (7.7)). This is also the case here, since $\mathbf{A}^2$ commutes with $\mathbf{I}$, $\mathbf{A}$, and $\mathbf{H}$. The eigenvalues of $\mathbf{A}^2$ are the squares of the eigenvalues of $\mathbf{A}$. The molecular orbital energies may then be written,

$$E_k = \alpha - n\gamma + \beta a_k + \gamma a_k^2. \quad (7.12)$$

A similar result has been determined for C_{60} using a basis of vectors for the nearest neighbors of the carbon atoms.[2]

7.4 Electron-hole symmetry breaking

Electron-hole symmetry is present for π-electron models that include only nearest neighbor transfer integrals, such as Hückel theory[14], and chemical structures that are alternant. In an alternant chemical structure, only carbon atoms participate in the π-electronic structure and these carbons may be divided into two disjoint sets, {A} and {B}, such that no carbon atom is bonded to another carbon atom in the same set[39]. Benzene, C_{60} and nanotubes are alternant structures (see Fig. 7.6). When

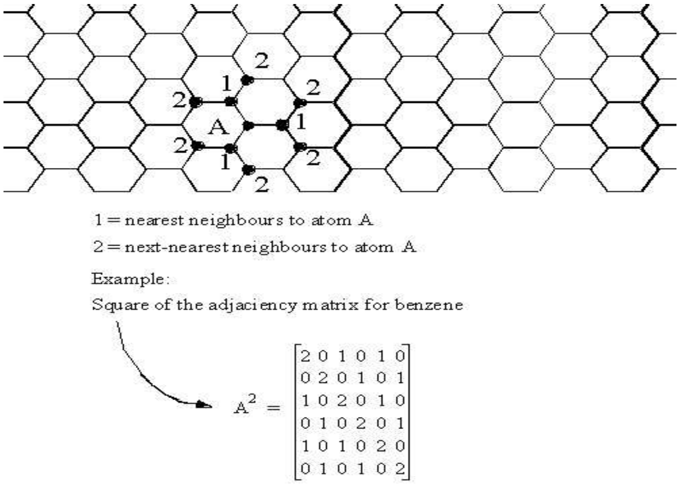

Figure 7.4: A section of the graphite sheet showing the nearest and next nearest neighbor atoms and an example of the square of the adjacency matrix for benzene.

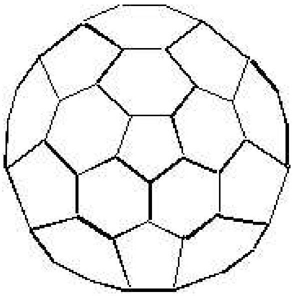

Figure 7.5: Fullerene type structure (in this case C_{60}) with only the bond framework and front facing bonds shown for clarity.

electron-hole symmetry applies, the valence and conduction band orbitals form pairs with energies distributed symmetrically about the Fermi energy. In terms of the adjacency matrix, electron hole symmetry implies that for every positive eigenvalue of the adjacency matrix, a_k, there exists a negative eigenvalue, $-a_k$.[82]

The inclusion of next-nearest-neighbor interactions in Hückel theory breaks electron-hole symmetry. This can be seen in Eq. (7.12), where the next-nearest-neighbor terms contribute to the orbital energies through the square of the eigenvalues of the adjacency matrix, γa_k^2. Note that the electron transfer terms, β and γ of Eq. (7.9), have negative algebraic sign[39]. The positive eigevalues of the adjacency matrix, a_k, therefore correspond to the valence bands. In the valence bands, the terms βa_k and γa_k^2 of Eq. (7.12) have the same sign and so the next-nearest-neighbor terms increase the width of the valence bands. In the conduction bands, a_k is negative and βa_k and γa_k^2 have opposite signs. The next-nearest neighbor terms therefore decrease the width of the conduction bands. This clearly breaks electron-hole symmetry.

The electron-hole symmetry breaking in a metallic (5,5) tube is shown in Fig. 7.7). Mintmire, Dunlap, and White[1] reported tight-binding results for the highest valence (HOMO) band and lowest conduction (LUMO) band as

$$E(k) = \pm\beta\left[1 + 2cos(k)\right], \tag{7.13}$$

where $k = 0..\pi$ is the length of the wavevector along the Γ reciprocal lattice direction, and the Fermi energy is at zero. The HOMO and LUMO bands intersect one another

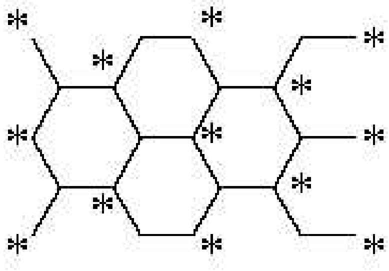

Figure 7.6: A portion of a hexagonal alternant sheet showing the partitioning of the carbon atoms into two disjoint sets of starred and unstarred carbons. The eigenvalues of the adjacency matrix in such a case are symmetric about zero.

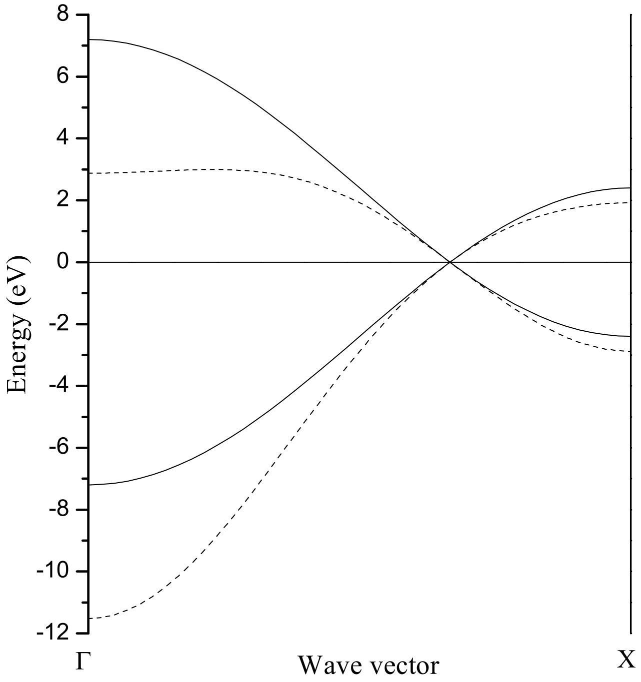

Figure 7.7: Plot of the highest occupied and lowest unoccupied bands for a (5,5) carbon nantube (eq. 7.15) with and without next-nearest-neighbor interactions as calculated using eq. 7.12.[1] Calculation of the bands including only nearest-neighbor interactions are represented by the solid lines and the dashed lines represent the calculuations done with the inclusion of next-nearest-neighbor interactions. β of eq. 7.12 was set to -2.4eV [1] and γ was set to 0.2β [2]. Crossing of the Fermi level occurs at $k = \frac{2}{3}\pi$.

at the Fermi energy, when $k = \frac{2}{3}\pi$. The eigenvalues of the adjacency matrix for the HOMO and LUMO bands of Eq. (7.13), are

$$a_k = \pm \left[1 + 2cos(k)\right]. \tag{7.14}$$

such that introduction of next-nearest neighbor terms leads to band energies

$$E(k) = \pm\beta \left[1 + 2cos(k)\right] + \gamma \left[1 + 2cos(k)\right]^2. \tag{7.15}$$

Fig. 7.7 shows the energies of these bands for β=-2.4eV, the value used in Ref. [1], and γ=0.2β, as derived for C_{60} in Ref. [2].

7.4.1 Effects of electron-hole symmetry breaking on the band gap

Here, we consider whether breaking of electron-hole symmetry alters the band gap. Before introduction of next-nearest-neighbor interactions, the band gap is present between a valence and conduction band that are related by electron-hole symmetry. Consider the difference in energy between these bands after introduction of next-nearest-neighbor terms,

$$E_{gap}(k) = \left|(\alpha - n\gamma + a_k\beta + a_k^2\gamma) - \Big(\alpha - n\gamma + b_k\beta + b_k^2\gamma\,)\right|, \tag{7.16}$$

where a_k and b_k are the eigenvalues of the adjacency matrix for the conduction and valence bands, respectively. Due to alternancy symmetry in the molecular structure, $a_k = -b_k$, and the Eq. (7.16) becomes

$$E_{gap}(k) = 2\,|\beta a_k|\,. \tag{7.17}$$

The gap between the bands is therefore unaffected by the next-nearest-neighbor terms, γ.

7.5 Effects of electron-hole symmetry breaking on the thermoelectric power

Here, we examine the thermoelectric power (TEP) of single walled nanotubes (SWNT). The thermoelectric power measures the electrical current that flows in response to a temperature gradient. The sign of the thermoelectric power indicates the sign of the predominant charge carriers in the material. Experimental measurements of the thermoelectric power have, until recently, been performed in air, exposing the nanotube to the presence of oxygen. Under these conditions, the thermoelectric power of the tubes is found to be positive, indicating that holes are the dominant charge carrier.[23] Recently, experiments have shown the extreme sensitivity of the thermoelectric power of carbon nanotubes to the presence of oxygen.[83, 25, 84] Oxygen is believed to induce electron traps in the material, such that holes become the dominant charge carrier. When care is taken to avoid oxygen contamination, the measured sign of the thermoelectric power becomes negative, indicating that electrons are the dominant charge carrier. Collins *et al.*[85] have found that at 350K, the TEP is about $-10\frac{\mu V}{K}$. Bradley *et al.* found that at 350K, the TEP is at least $-60\frac{\mu V}{K}$. This disagreement has not, to the best of our knowledge, been resolved.

In a system with electron-hole symmetry, the TEP is zero, since thermal excitation will create equal amounts of electrons and holes and these electrons and holes will have identical drift velocities. There will then be no net flow of current in response to a temperature gradient. Breaking of electron-hole symmetry will lead to a nonzero TEP, and here we derive an analytical expression for the TEP arising from next-nearest-neighbor interactions in a single nanotube.

The standard Mott form for the drift thermoelectric power, in one dimension, is,

$$S_d = -\frac{\pi^2 k_b^2 T}{3e}\left(\frac{v'}{v}+\frac{\tau'}{\tau}\right), \tag{7.18}$$

where v is the band velocity, τ is the electron relaxation (scattering) time, and the primes indicate derivatives with respect to energy.[23] The relaxation time is expected to be relatively independent of energy[23], and so this term is typically ignored. We will also adopt this approximation. The band velocity is given by $v = \frac{1}{\hbar}\frac{\partial E(\vec{k})}{\partial \vec{k}}$.[86]

For eq. 7.12, the v and v' are given by,

$$\begin{aligned} v &= \frac{1}{\hbar}\frac{\partial E_{nextnearestneighbor}(\vec{k})}{\partial \vec{k}} = \frac{1}{\hbar}\left(\beta a_k' + 2\gamma a_k a_k'\right) && (7.19) \\ v' &= \frac{\partial v}{\partial E(\vec{k})} = \frac{\partial v}{\partial \vec{k}}\frac{\partial \vec{k}}{\partial E(\vec{k})} = \frac{\partial^2 E(\vec{k})}{\partial \vec{k}^2}\frac{\partial \vec{k}}{\partial E(\vec{k})} && (7.20) \\ &= \frac{1}{\hbar}\frac{\beta a_k'' + 2\gamma a_k a_k'' + 2\gamma (a_k')^2}{\beta a_k' + 2\gamma a_k a_k'}. \end{aligned}$$

where, here, the primes indicate differentiation with respect to $\vec{k}$. Substituting eqs 7.20 and 7.21 into eq. 7.18 the resulting expression for the $\frac{v'}{v}$ is,

$$\frac{v'}{v} = \frac{\beta a_k'' + 2\gamma (a_k')^2 + 2\gamma a_k a_k''}{(a_k')^2(\beta + 2\gamma a_k)^2}. \tag{7.21}$$

For a system with alternancy symmetry, the contribution of the a_k'' must cancel. For instance, for the (5,5) nanotube of Fig. 7.7, the bands crossing at the Fermi energy will lead to a_k'' of equal magnitudes but opposite signs and thus make cancelling contributions to the TEP. This is a consequence of the fact that for a system with electron-hole symmetry, thermal excitation will create equal numbers of electrons and holes and these will have equivalent velocities, v. Removing the contributions of a_k'', Eq. (7.21) becomes

$$\frac{v'}{v} = \frac{2\gamma(a_k')^2}{(a_k')^2(\beta + 2\gamma a_k)^2}. \tag{7.22}$$

This may be re-written in terms of the ratio between γ and β, C such that $\gamma = C\beta$, we obtain

$$\frac{v'}{v} = \frac{2C(a_k')^2}{\beta(a_k')^2(1 + 2Ca_k)^2} = \frac{2C}{\beta(1 + 2Ca_k)^2}. \tag{7.23}$$

For a metallic (5,5) tube, the eigenvalues of the adjacency matrix, a_k are given by Eq. (7.14). The HOMO and LUMO bands intersect at the Fermi level for $k = \frac{2}{3}\pi$. At $k = \frac{2}{3}\pi$, $a_k = 1 + 2cos(k) = 0$. About the Fermi level and considering only the HOMO and LUMO bands, eq. 7.23 reduces to,

$$\frac{v'}{v} = \frac{4C}{\beta}. \tag{7.24}$$

Mintmire *et al.* estimate that for the (5,5) tube $\beta = -2.4$eV, and in their study of C$_{60}$ Wang *et al.* show that C of eq. 7.24 should lie between 0 and 0.5[1, 2]. Using this range of parameters in Eqs. (7.18) and (7.24) leads to a TEP of between 0 and $-0.02\frac{\mu V}{K^2}$T. The negative values of the TEP calculated using eq. 7.24 indicate that the predominant charge carrier in the armchair nanotubes are electrons. This is as expected, since the next-nearest-neighbor terms compress the conduction bands and expand the valence bands (Fig. 7.7), leading to a higher thermal population of electrons. At 350K, the predicted thermopower is between 0 and $-7\frac{\mu V}{K}$. This is in reasonable agreement with the measurement of $-10\frac{\mu V}{K}$ by Collins *et al*[85], and considerably smaller than the measurement of greater than $-60\frac{\mu V}{K}$ by Bradley *et al*[25].

7.6 Discussion

This chapter derives a simple means for including next-nearest-neighbor transfer terms in Hückel calculations of certain types of carbon structures. The requirements are that (i) all bond lengths be identical, (ii) the atoms must all have equal numbers of nearest neighbors, and (iii) all next-nearest neighbor distances must be equal. These conditions hold for benzene, C_{60} and the infinite nanotubes that are the primary subject of this chapter.

The next-nearest-neighbor terms break electron-hole symmetry in these systems. Although this symmetry breaking has no effect on the band gap, it does alter the thermoelectric power (TEP). When electron-hole symmetry applies, the TEP of a single nanotube is zero. For reasonable estimates of next-nearest-neighbor interactions, the TEP induced by such interactions can be as high as $-7\frac{\mu V}{K}$ at 350K. Experimental estimates include $-10\frac{\mu V}{K}$ and $-60\frac{\mu V}{K}$. The results presented here suggest that electron-hole symmetry breaking due to next-nearest-neighbor interactions may account for a substantial portion of the TEP of nanotubes.

Part III

Dielectric effects

Chapter 8

Dynamic dielectric screening and exciton binding energies in conjugated polymers

8.1 Introduction

In light-emitting-diodes (LEDs) based on conjugated polymers, an electron and hole are injected into an undoped conjugated polymer, such as poly-(para-phenylene vinylene) (PPV)[4, 87]. These charges migrate through the material and combine to emit a photon. An important quantity for developing an understanding of this process is the exciton binding energy, the difference in energy between a well-separated electron-hole pair and the state that emits the photon. Standard semi-empirical quantum chemistry models such as PPP[26], ZINDO[27] or MNDO[28] yeild exciton binding energies of greater than 2.5eV, when applied to a single polymer chain. This is much greater than the exciton binding energies seen in solid-state conjugated polymers. For instance, there is general agreement that the exciton binding energy in polydiacetylene is 0.5eV [88, 89, 90], and that photoexcitation of polyacetylene leads to the rapid formation of both charged and neutral solitons[91, 92, 93]. In PPV, experimental estimates for the exciton binding energy include near 0.0[94], 0.2eV[95], 0.4eV[96, 97], and 0.9eV[98, 31]; and theoretical estimates include 0.4eV[99, 100] and

0.9eV[31].

Many theoretical studies of conjugated polymers use a single-chain Hamiltonian parameterized to solid-state observations. To obtain agreement with solid-state exciton binding energies, the Coulomb repulsion between electrons must be substantially weaker than that typically used in semi-empirical quantum chemistry[29, 30, 31]. This need to weaken the electron-electron interactions in a single-chain Hamiltonian likely reflects the importance of Coulomb screening from adjacent polymer chains. This paper continues our development of an electronic-polaron model that explicitly includes Coulomb screening from adjacent chains. The model was originally applied to two polyene chains, one "solute" polyene and one "solvent" polyene. Recently, this model has been extended such that the number of solvent chains is sufficient to allow a reliable extrapolation to the solid-state limit. In both the two-chain and solid-state calculations, the solute chain was described with a PPP Hamiltonian and the solvent chains were described with Hückel theory. Hückel theory was used for the solvent chains because it greatly simplifies the evaluation of the Hamiltonian matrix elements. In this paper, the use of Hückel theory for the solvent is tested and shown to be a good approximation.

There are two important aspects to our electronic-polaron model. The first is the use of electron-hole, rather than electron-electron, screening. In the parameterization of a single-chain Hamiltonian to solid-state data, it is typically the *electron-electron* interaction potential that is modified[29, 30, 31]. Here, we consider how interchain interactions modify the *electron-hole* interactions present in the excited states. This is analogous to models of three-dimensional semiconductors, where it is the electron-hole potential, not the electron-electron potential, that is screened[101]. The second important aspect of our model is the inclusion of the time-scale of both the electron-hole motion and the solvent polarization. In electron-hole screening, the relevant time-scales are those of the solvent polarization and the electron-hole motion. The time scale of the solvent polarization is inversely proportional to the optical gap, about 2eV. The time scale for electron-hole motion in the exciton is inversely proportional to the exciton binding energy. (A non-stationary state prepared with a dipole moment pointing to the left will oscillate to the right on this time scale.) When the exciton binding energy is only a few percent of the band gap, as in many inorganic semiconductors[101], the electron-hole motion is orders of magnitude slower than the solvent polarization. In such systems, the polarization of the surroundings can follow the motion of the electron and hole and thus a screened electron-hole interaction potential, such as that used Wannier exciton theory, is a good approximation.[101] But in conjugated polymers, the exciton binding energies may be greater than 2.5eV for an isolated chain and 0.5eV or larger in the solid state. A separation of time-scales is then not apparent, and the timescales of both electron-hole motion and solvent polarization must be included in the model.

The dynamic aspects of the electron-hole screening process play a central role in establishing the exciton binding energy. Interchain interactions lower the exciton binding energy because the "solvation energy" of the free electron and hole is greater than the solvation energy of the exciton. In the free electron-hole pair states, the charge fluctuations arising from electron-hole motion are slow and the polarization of the surrounding chains can nearly follow the electron-hole motion. This leads to a relatively large solvation energy for the free electron-hole pair states. In the exciton state, the charge-fluctuations are quite fast, and the polarization of the surrounding chains cannot follow the electron-hole motion. The exciton state is then only weakly solvated. The electron and hole then shed their solvation cloud when they join to form an exciton. This enhances the differential solvation of the free electron-hole pair versus the exciton, and leads to a large reduction in the exciton binding energy.

Explicit inclusion of screening will likely lead to better transferability of parameters between different polymer systems. It should also allow detailed information on molecules, either from experiment or high-level *ab initio* calculations, to be used in the parametrization of solid-state models. The use of molecular data is especially important when detailed solid-state experimental data is difficult to obtain, such as when modeling the effects of chemical defects and physical morphology.

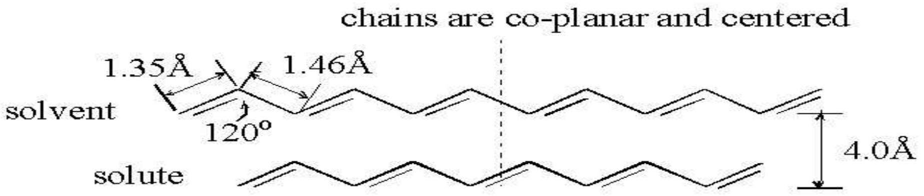

Figure 8.1: Chemical structure of the system used to study the effects of interchain interactions on the exciton binding energy. In all the calculations presented here, the solvent chain has 15 unit cells. The solute chain length is varied in the calculations.

8.2 Computational Methods

8.2.1 Hamiltonian

The calculations are performed on a model system consisting of two polyenes, one solute and one solvent chain, with the geometries shown in Figure 8.1. The Hamiltonian is

$$H = H^{sol} + H^{solv} + H^{sol-solv}, \tag{8.1}$$

where H^{sol} is the solute Hamiltonian, H^{solv} the solvent Hamiltonian, and $H^{sol-solv}$ is the solute-solvent interaction Hamiltonian.

The solute is described using Pariser-Parr-Pople theory[26],

$$\begin{aligned} H^{sol} &= \sum_{i,j,\sigma} \left[-I\delta_{i,j} + \alpha^{sol}_{j,i}\right] a^{\dagger}_{j,\sigma} a_{i,\sigma} \\ &+\frac{1}{2}\sum_{i} U\left(\hat{\rho}_i - 1\right)\hat{\rho}_i + \sum_{i<j} U(r_{j,i})\,\hat{\rho}_j\hat{\rho}_i, \end{aligned} \tag{8.2}$$

where $a^{\dagger}_{i,\sigma}(a_{i,\sigma})$ creates (destroys) an electron with spin σ in the p-orbital on the i^{th} carbon, $\hat{\rho}_i$ is the charge operator on the i^{th} carbon, $\hat{\rho}_i = 1 - a^{\dagger}_{i,\alpha}a_{i,\alpha} - a^{\dagger}_{i,\beta}a_{i,\beta}$, and $r_{i,j}$ is the distance between carbons i and j. For the one electron terms, $\alpha^{sol}_{j,i}$, we use nearest-neighbor transfer integrals of β^{sol}_1=-2.228eV for single bonds and β^{sol}_2=-2.581eV for double bonds. Both the electron-electron and nuclear-nuclear repulsions are described with the Ohno potential,

$$U(r) = \frac{14.397eVA}{\sqrt{\left(\frac{14.397eVA}{U}\right)^2 + r^2}} \tag{8.3}$$

where U is the Hubbard parameter. I and U are chosen such that application of the Hamiltonian to a single carbon atom yields the ionization potential and electron affinity of an sp^2 hybridized carbon; I is set equal to the ionization potential of an sp^2 hybridized carbon, 11.16eV, and U is set equal to the difference between the ionization potential and electron affinity of an sp^2 hybridized carbon, U=11.13eV.[102]

The solute and solvent interact through Coulomb interactions,

$$H^{sol-solv} = \sum_{I,i} U(r_{I,i})\, \hat{\rho}_I \hat{\rho}_i, \tag{8.4}$$

where i is summed over solute atoms and I is summed over solvent atoms.

We will compare the results from two different models for the solvent. The simpler model is Hückel theory,

$$H^{solv} = \sum_{I,J,\sigma} \alpha_{J,I}^{solv}\, a_{J,\sigma}^{\dagger} a_{I,\sigma}, \tag{8.5}$$

with $\alpha_{J,I}^{solv}$ being nearest-neighbor transfer integrals, (β_1^{solv} for single bonds and β_2^{solv}) for double bonds. The other solvent Hamiltonian is the PPP Hamiltonian of eq. 8.2.The Hückel Hamiltonian for polyenes has only two relevant parameters, the transfer integrals for single and double bonds, β_1^{solv} and β_2^{solv}. In the long-chain limit, both the band (free-charge) gap and optical gap are equal to $2\left|\beta_1^{solv} - \beta_2^{solv}\right|$. The band width is set by $2\left|\beta_1^{solv} + \beta_2^{solv}\right|$, which is equal to the difference in energy between the top of the valence band and the bottom of the conduction band. The Hückel parameters are chosen to mimic the PPP Hamiltonian. To keep approximately the same band width as in PPP theory, we set the sum of the Hückel transfer integrals to the sum of the transfer integrals of PPP theory, $(\beta_1^{solv} + \beta_2^{solv})/2 = -2.4045$eV. In PPP theory, the optical gap can be quite different from the band gap. The choice of the Hückel gap depends on which aspect of PPP theory we are trying to mimic. The relevant aspect here is the response of the solvent to charge fluctuations on the solute, i.e., the response to an external electric field. The Hückel gap is thus set equal to the optical gap from PPP theory, as calculated from the Random Phase Approximation (RPA)[103]. The RPA gap is used because the linear response obtained from RPA theory is equal to that obtained from time-dependent Hartree-Fock theory (TDHF). The calculations discussed below use Hartree-Fock theory to calculate the polarization induced by the solute charge distribution, and are thus analogous to TDHF theory. The RPA gap from PPP theory is 2.66 eV, so the Hückel model for the solvent uses $2\left|\beta_1^{solv} + \beta_2^{solv}\right| = 2.66eV$.

8.2.2 Description of isoluted solute

The effects of interchain interactions on the exciton binding energy are obtained by comparing the solvation energy of the exciton to that of a free electron (a polyene anion) and a free hole (a polyene cation). The symmetry of the Hamiltonian is such that the solvation energy of the anion and cation are equal. The isolated solute is described with S-CI theory in a local orbital basis[26],

$$\Psi^{isolated\ neutral} = \sum_{a,r} c_a^r \psi_a^r \tag{8.6}$$

where ψ_a^r has a hole in the valence-band orbital centered on the a^{th} unit cell and an electron in the conduction-band orbital centered on the r^{th} unit cell. The summation of eq. 8.6 is over all positions of the electron and hole, and the coefficients, c_a^r are determined variationally. The cationic polyene is described with the variational trial form,

$$\Psi^{isolated\ cation} = \sum_{a} c_a \psi_a. \tag{8.7}$$

where ψ_a has a hole in the valence-band orbital centered on the a^{th} unit cell.

8.2.3 Basis set for solvent polarization

The solvent is described using the following basis set. The basis function, Φ_0, is the unpolarized solvent, i.e. the solvent in the absence of the ground state of the solute. Φ_a^r is the Hartree-Fock ground state of the solvent in the presence of the solute charge distribution corresponding to ψ_a^r. (The magnitude of the solute charge distribution is multiplied by a constant scaling factor, ζ, for reasons to be discussed below.) Φ_a^r thus describes the polarization induced by a hole on the a^{th} unit cell of the solute and an electron on the r^{th} unit cell. Using this basis, the variational procedure can optimize the magnitude of the solvent polarization by mixing the unpolarized function, Φ_0, with the polarized functions, Φ_a^r. The spatial distribution of the polarization can be optimized by mixing together the various polarized functions, Φ_a^r. A similar basis is used for the cation, consisting of the unpolarized solvent Φ_0 and functions Φ_a that describe the polarization induced by a hole on the a^{th} unit cell of the solute polyene.

The above basis sets are used to describe the polarization induced by an exciton or hole delocalized over a polymer. These charge distributions are much more diffuse than the charge distributions of ψ_a or ψ_a^r, which describe holes and electrons localized at specific positions on the solute. Thus in generating Φ_a and Φ_a^r, the solute charge distribution is multiplied by the scaling parameter, $\zeta < 1$. This is useful because the localized charge distributions of ψ_a or ψ_a^r can cause the solvent polarization to respond nonlinearly. The basis set performs best when ζ is chosen such that Φ_a and Φ_a^r are not in the nonlinear regime[63]. In the calculations presented here, $\zeta = 0.2$.

The calculation of the Hamiltonian matrix elements is discussed in the Appendix.

8.2.4 Simplified reaction-field model

The reaction-field model assumes the dielectric response of the solvent is much slower than the charge fluctuations arising from electron-hole motion on the solute. In the implementation used here, the electron and hole on the solute are first delocalized as in Eqs. 8.6 and 8.7, and the averaged charge distribution is then solvated. This differs from the self-consistent reaction-field (SCRF) model[104, 105], which allows interaction with the solvent to alter the solute charge distribution. Since the systems studied here do not have a permanent dipole moment, our model should not differ significantly from the SCRF model. An important exception is when solvation effects are sufficiently strong that the SCRF model favors symmetry-breaking on the solute chain. For instance, in the case of a charged polyene, the SCRF model may favor the localization of charge on some portion of the chain. This charge localization is not allowed in the reaction-field model used here, which assumes the solute charge distribution is that of the isolated solute polyene.

The solvation energies are calculated by diagonalizing the solvent Hamiltonian, including the interaction with the solute charge distribution, in the basis set described in Section 8.2.3.

8.2.5 Screened electron-hole interaction model

This limit is that of Wannier exciton theory[101], where the dielectric response of the solvent is assumed to be much faster than the charge fluctuations arising from electron-hole motion on the solute. The solvent polarization is then set by the instantaneous position of the electron and hole, leading to dielectric screening of the electron-hole interaction. This model is implemented by starting with the matrix representation of the solute Hamiltonian, H^{sol} of Eq. 8.1, in the solute basis, ψ_a or ψ_a^r of Eqs. 8.7 and 8.6. The solvation energy of the charge distributions corresponding to ψ_a or ψ_a^r are then calculated and added to the diagonal of the Hamiltonian matrix. The resulting matrix is then diagonalized.

For the exciton calculation, the solvation energies are calculated from the Hartree-Fock ground state energies of the solvent in the presence and absence of the charge distributions corresponding to ψ_a^r. As discussed in Section 8.2.3, the localized charge distribution of ψ_a^r may induce a nonlinear polarization in the solvent. This is prevented by first multiplying the charge distributions by the scaling factor ζ=0.2. The calculated solvation energy is then scaled up assuming a linear solvent response, i.e. the solvation energy of the scaled charge distribution is divided by ζ^2. For the cation calculations, the solvation energies are calculated using the basis set described in Section 8.2.3.

8.2.6 Electronic Polaron Model

In the electronic-polaron model, the Hamiltonian of Eq. 8.1 is diagonalized in a direct-product basis of solute and solvent functions[106]. The solute basis functions are the ψ_a and ψ_a^r of Eqs. 8.7 and 8.6. The solvent basis functions are the Φ_a and Φ_a^r described in Section 8.2.3. Since the full Hamiltonian is used and the matrix elements are evaluated exactly (see the Appendix), no assumptions are made about the relative time scale of electron-hole motion as compared to solvent polarization.

For the exciton calculation, the size of a complete direct-product basis scales as

N^4, N being the number of unit cells on the solute. To avoid this rapid increase in the size of the basis with solute chain length, the following variational form is used for the combined solute-solvent wavefunction,[107]

$$\Psi = \sum_{a,r} \psi_a^r \left(d_a^r \Phi_0 + \sum_{a',r'} c_{a,a'}^{r,r'} \Phi_{a'}^{r'} \right) \left\{ \begin{array}{l} |a' - a| \leq m_{lag} \\ |r' - r| \leq m_{lag} \end{array} \right. . \tag{8.8}$$

A similar basis may be constructed for the cation. As m_{lag} is increased, this basis approaches the full direct-product basis. When $m_{lag} = 0$, each solute function ψ_a^r is paired with the corresponding solvent polarization Φ_a^r; the spatial distribution of the solvent polarization is thereby constrained to follow the motion of the electron and hole on the solute, and the variational procedure adjusts only the magnitude of the polarization by changing the ratio of the c and d coefficients. With $m_{lag} > 0$, the solvent polarization may lag behind the motion of the electron and hole, and the variational procedure has more flexibility in determining the spatial distribution of the polarization.

8.3 Results

Figures 8.2 and 8.3 show the calculated solvation energies of a cationic polyene and the $1B_{1u}$ exciton state of a polyene, as a function of solute chain length.

The simplified reaction-field model of Sec. 8.2.4 assumes the solvent polarization is much slower than electron-hole motion on the solute. The solvent polarization is then set by the *averaged* charge distribution of the solute. Within this model, the exciton state is non-polar and has zero solvation energy (Figure 8.3). For the cation, as the solute chain length is increased, the solute charge distribution becomes increasingly diffuse and the solvation energy tends toward zero (Figure 8.2). Soliton formation will localize the solute charge distribution and lead to a finite solvation energy in the long-chain limit. A reasonable estimate for the soliton size[108, 109] is about 14 unit cells[110, 111]. This corresponds to a rather diffuse charge distribution, and a low solvation energy in Figure 8.2. Within this model, the solvation energies obtained using the Hückel Hamiltonian for the solvent agree well with those obtained using the PPP Hamiltonian.

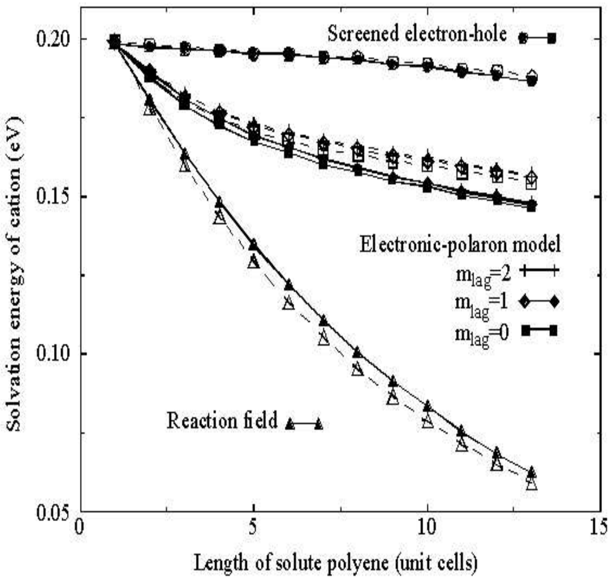

Figure 8.2: Solvation energy of a polyene cation due to interaction with a solvent chain of 15 unit cells. The reaction-field, screened electron-hole and electronic-polaron models are described in Secs. 8.2.4, 8.2.5, and 8.2.6. The solid lines and filled symbols are the results obtained using the PPP model for the solvent. The dashed lines and open symbols are the results obtained using the Hückel model for the solvent.

At the opposite extreme is the screened electron-hole interaction model of Sec. 8.2.5, which assumes the solvent polarization is much faster than electron-hole motion. The solvent polarization is then set by the *instantaneous* position of the electron and hole, thus screening the electron-hole interaction. In this model, the solvation energy of the cation is that of a localized hole, and thus is relatively independent of chain length. The solvation energy of the exciton is that appropriate for a screened Coulomb interaction between the electron and hole. For the cation, the solvation energies obtained using the Hückel Hamiltonian for the solvent agree well with those obtained using the PPP Hamiltonian. However, for the exciton, there is substantial disagreement. This is discussed further in Section 8.4.

The electronic-polaron model of Section 8.2.6 makes no assumptions about the relative time-scale of electron-hole motion versus solvent polarization. Figures 8.2 and 8.3 show that the predicted solvation energies lie between those of the reaction-field and screened electron-hole interaction models. This can be understood as follows.

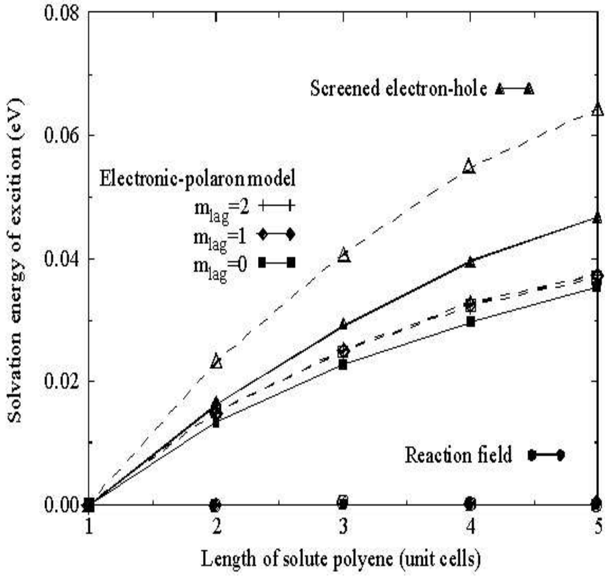

Figure 8.3: Solvation energy of the exciton state due to interaction with a solvent chain of 15 unit cells. Notation is as in Figure 8.2. Using the PPP Hamiltonian of the solvent only lag=0 results were obtained.

Formation of a polarization cloud around the electron and hole leads to a favorable electrostatic interaction between the solute and solvent chains; however, the resulting increase in the effective mass of the electron and hole lowers the delocalization energy. The electronic-polaron model includes these changes in effective mass, since it calculates the matrix elements of the full Hamiltonian, Eq. 8.1, between the basis functions of Eq. 8.8. However, the increase in effective mass is ignored by the screened electron-hole interaction model, which modifies only the Coulomb interaction between the electron and hole. The screened electron-hole interaction model thereby overestimates the solvation energy of both the exciton and the cation. The solvation energies obtained using the Hückel Hamiltonian for the solvent agree well with those obtained using the PPP Hamiltonian.

8.4 Conclusions

Figures 8.2 and 8.3 show that, with one exception, the solvation energies obtained using the Hückel Hamiltonian for the solvent agree well with those obtained using the PPP Hamiltonian. That Hückel theory is a good approximation is not surprising since Hückel theory provides a reasonable description of the linear response of a conjugated polymer to an applied electric field. Unlike dielectric continuum models, which implicitly assume a solvent made up of point dipoles, Hückel theory captures the delocalized electronic structure of the solvent. Hückel theory also contains the correct time-scale for the dielectric response, an issue of importance to the electronic polaron model. This time-scale is set by the optical gap and the Hückel parameters were chosen to yield same optical gap as PPP theory.

While there is in general good agreement between the Hückel and PPP models for the solvent, Figure 8.3 indicates a rather large disagreement between for the solvation energy of the exciton in the screened electron-hole model. In the screened electron-hole model, the solvation energies of the charge distributions associated with various positions of the electron and hole, ψ_a^r, are calculated and added to the diagonal of the S-CI matrix (see Section 8.2.5). The disagreement between the Hückel and PPP models indicates that these two Hamiltonians find different solvation energies for these charge distributions. This is surprising since they agree on the solvation energy of the cation (Figure 8.2), and thus agree on the solvation energy of a hole located at various positions on the chain, ψ_a. We are currently investigated the origin of this disagreement.

The electronic-polaron model makes no assumptions about the relative time-scale of electron-hole motion versus solvent polarization, and so is the most accurate model considered here. Within this model, the Hückel Hamiltonian for the solvent gives solvations energies that are in good agreement with those obtained using the PPP Hamiltonian. The use of Hückel theory is much less computationally intensive than PPP theory, and allows us to include up to 18 solvent chains with 80 carbons each. This is sufficient to allow extrapolation to the solid-state limit. The agreement between the Hückel and PPP models for the solvent validates the use of Hückel theory in these calculations, and confirms that the dynamic dielectric response plays a crucial role in establishing the exciton binding energy in conjugated polymers.

Interchain interactions lower the exciton binding energy because the “solvation” energy of the free electron and hole is greater than the solvation energy of the exciton.

For instance, in Figure 8.2, the electronic-polaron model predicts that the solvation energy of a free hole (a cation) is about 0.15eV. Since, for the Hamiltonian used here, the solvation energy of an electron is equal to that of a hole, the free electron-hole pair states are solvated by about 0.3eV. This solvation energy is large because the charge fluctuations arising from electron-hole motion are slow and the polarization of the surrounding chains can nearly follow the electron-hole motion. In Figure 8.3, the electronic-polaron model gives a solvation energy for the exciton of about 0.04eV. That the solvation energy of the free electron-hole pair states is nearly an order of magnitude larger than that of the exciton remains true in the solid-state limit. The solvation energy of the exciton state is small because the charge-fluctuations arising from electron-hole motion are fast, and the polarization of the surrounding chains cannot follow the motion of the electron and hole. While interchain interactions have a large effect on the exciton binding energy, they have relatively minor effects on the exciton state itself. The electron and hole must shed their solvation cloud when they join to form an exciton. This consequence of dynamic dielectric screening enhances the differential solvation of the free electron-hole pair versus the exciton, and leads to a large reduction in the exciton binding energy.

More generally, the electronic polaron model predicts that the effective strength of the dielectric medium varies from state to state depending on the time-scale for charge fluctuations (electron-hole motion) in that particular state. This observation may help resolve many long-standing questions concerning the relative importance of electron-electron interactions in these materials.

8.5 Acknowledgment

The work was supported by the National Science Foundation (Grant No. CHE-9530148).

8.6 Appendix

8.6.1 Evaluation of the matrix elements

In the electronic polaron model, the Hamiltonian of eq. 8.1 is diagonalized in a direct-product basis of solute and solvent basis functions. Here, we consider the evaluation of the Hamiltonian matrix elements needed in this procedure. The solute basis functions are those of S-CI theory, and the matrix elements are the standard elements of configuration-interaction theory[112]. The solvent basis functions, Φ_0 and Φ_a^r discussed in Section 8.2.3 describe the solvent in the presence of various solute charge distributions. We will derive expressions for the matrix elements between any two of these functions, denoted $\overline{\Phi}$ and Φ. These functions are the Hartree-Fock ground state of the solvent in the presence of various solute charge distributions, and so are single Slater determinants,

$$\overline{\Phi} = \overline{a}_1^\dagger \overline{a}_2^\dagger \ldots |0\rangle \ ; \ \Phi = a_1^\dagger a_2^\dagger \ldots |0\rangle \, , \tag{8.9}$$

where $a_i^\dagger$ creates an electron in spin-orbital ϕ_i of Φ, and $\overline{a}_i^\dagger$ creates an electron in spin-orbital $\overline{\phi}_i$ of $\overline{\Phi}$.

The overlap between $\overline{\Phi}$ and Φ is the following determinant of the spin-orbital overlap matrix,

$$\left\langle \bar{\Phi} \,\middle|\, \Phi \right\rangle = \left| \underline{\underline{S^{occ}}} \right| \tag{8.10}$$

where $\underline{\underline{S^{occ}}}$ is a matrix holding the overlaps between the occupied spin-orbitals,

$$S^{occ}_{i,j} = \langle \overline{\phi}_i | \phi_j \rangle \ ; \ i,j = 1 \ldots N_{occ}, \tag{8.11}$$

and N_{occ} is the number of occupied spin-orbitals in $\overline{\Phi}$ and Φ.

The matrix elements of a one-electron operator, $\hat{O}_1$, may be obtained by first expanding the operator in the spin-orbital basis of Φ,

$$\hat{O}_1 = \sum_{i,j} O_{i,j} a_i^\dagger a_j, \tag{8.12}$$

where $O_{i,j} = \langle \phi_i | \hat{O}_1 | \phi_j \rangle$. When $\hat{O}_1$ is applied to $|\Phi\rangle$, it generates singly-excited configurations, Φ_a^r, in which an electron has been promoted from a filled spin-orbital,

a, to an empty spin-orbital, r. The overlap between this singly excited configuration and $\overline{\Phi}$ is then similar to the overlap in eq. 8.11, with the a^{th} column of $\underline{\underline{S^{occ}}}$ replaced as follows,

$$\left\langle \bar{\Phi} \,\middle|\, \Phi_a^r \right\rangle = \underline{\underline{S_a^r}} \quad ; \quad (S_a^r)_{i,j} = \begin{cases} S^{occ}_{i,j} & (j \neq a) \\ \left\langle \bar{\phi}_i \,\middle|\, \phi_r \right\rangle & (j = a) \end{cases} \tag{8.13}$$

The matrix element of $\hat{O}_1$ may now be written,

$$\left\langle \overline{\Phi} \right| \hat{O}_1 \left| \Phi \right\rangle = \left| \underline{\underline{S^{occ}}} \right| \sum_a O_{a,a} + \sum_{a,r} O_{r,a} \left| \underline{\underline{S_a^r}} \right|, \tag{8.14}$$

where a is summed over the occupied spin-orbitals of Φ and r is summed over the unoccupied spin-orbitals of Φ.

Evaluating the determinant $|\underline{\underline{S_a^r}}|$ is a potentially expensive step, especially since it occurs inside a two-fold orbital summation. However, a large simplification may be achieved by writing $\left|\underline{\underline{S^{occ}}}\right|$ as,

$$\left| \underline{\underline{S^{occ}}} \right| = \sum_i S^{occ}_{i,j} C_{i,j}, \tag{8.15}$$

where $\underline{\underline{C}}$ is the matrix of cofactors of $\underline{\underline{S^{occ}}}$. The determinant of $\underline{\underline{S_a^r}}$ can be then be obtained from,

$$\left| \underline{\underline{S_a^r}} \right| = \sum_{i \in occ} \left\langle \bar{\phi}_i \,\middle|\, \phi_r \right\rangle C_{i,a} = \left| \underline{\underline{S}} \right| \sum_{i \in occ} \left\langle \bar{\phi}_i \,\middle|\, \phi_r \right\rangle (\underline{\underline{S^{occ-1}}})_{a,i}. \tag{8.16}$$

where the cofactor matrix has been written in terms of the inverse of $\underline{\underline{S^{occ}}}$. The computationally expensive matrix inversion needs to be done only once for each set of functions, Φ and $\overline{\Phi}$.

The above is sufficient when the Hückel Hamiltonian is used for the solvent since both it and the Coulomb interactions with the solute, are one-electron operators. However, when the PPP Hamiltonian is used for the solvent, it is also necessary to evaluate the two-electron operator,

$$\hat{O}_2 = \frac{1}{2} \sum_{i,j,k,l} \langle i\ j | k\ l \rangle a_i^\dagger a_j^\dagger a_l a_k, \tag{8.17}$$

where $\langle i\ j | k\ l \rangle$ is the two-electron integral between spin-orbitals in physicist's notation[112]. This is much more difficult than the one-electron operator, because when $\hat{O}_2$ operates on Φ it generates both singly-excited, Φ^{r}_{a}, and doubly-excited, $\Phi^{r,s}_{a,b}$ configurations. So in addition to evaluating $\underline{\underline{S^{r}_{a}}}$ of eq. 8.16, it is necessary to evaluate,

$$\left\langle \bar{\Phi} \,\middle|\, \Phi^{r,s}_{a,b} \right\rangle = \underline{\underline{S^{r,s}_{a,b}}} \quad ; \quad \left(S^{r,s}_{a,b}\right)_{i,j} = \begin{cases} S^{occ}_{i,j} & (j \neq a; j \neq b) \\ \left\langle \overline{\phi}_i \,\middle|\, \phi_r \right\rangle & (j = a) \\ \left\langle \overline{\phi}_i \,\middle|\, \phi_s \right\rangle & (j = b) \end{cases} \tag{8.18}$$

The matrix elements of $\hat{O}_2$ are then,

$$\langle \overline{\Phi} | \hat{O}_2 | \Phi \rangle = \frac{1}{2} \sum_{a,b \in occ} \langle ab||ab\rangle \left|\underline{\underline{S}}\right| + \sum_{\substack{a,b \in occ \\ r \in unocc}} \langle rb||ab\rangle \left|\underline{\underline{S^{r}_{a}}}\right| + \frac{1}{2} \sum_{\substack{a,b \in occ \\ r,s \in unocc}} \langle rs||ab\rangle \left|\underline{\underline{S^{r,s}_{a,b}}}\right|, \tag{8.19}$$

where $\langle ab||ab\rangle = \langle ab|ab\rangle - \langle ab|ba\rangle$. The third term of eq. 8.19 is computationally expensive, due to both the four-fold orbital summation and the double substitution in $|\underline{\underline{S^{r,s}_{a,b}}}|$.

The basis functions Φ and $\overline{\Phi}$ are restricted Hartree-Fock ground states and thus have doubly-occupied spatial orbitals. It is convenient to rewrite eq. 8.19 in terms of summations over spatial orbitals. A simplification results from the fact that the overlap matrices $\underline{\underline{S^{occ}}}$, $\underline{\underline{S^{r}_{a}}}$ and $\underline{\underline{S^{r,s}_{a,b}}}$ are block diagonal in the spin coordinate. In particular, when a and b have different spins, the determinant of the doubly-substituted spin-orbital matrix, $\underline{\underline{S^{r,s}_{a,b}}}$, may be written as the product of the determinants of two singly-substituted spatial-orbital matrices. In terms of spatial orbitals, eq. 8.19 becomes

$$\begin{aligned} \langle \Phi' | \hat{O}_2 | \Phi \rangle \quad &= \sum_{a,b \in occ} \left(2\langle ab|ab\rangle - \langle ab|ba\rangle\right) \left|\underline{\underline{S}}\right|^2 + \sum_{\substack{a,b \in occ \\ r \in unocc}} \left(4\langle rb|ab\rangle - 2\langle rb|ba\rangle\right) \left|\underline{\underline{S}}\right| \left|\underline{\underline{S^{r}_{a}}}\right| \\ &+ \sum_{\substack{a,b \in occ \\ r,s \in unocc}} \langle rs|ab\rangle \left|\underline{\underline{S}}\right| \left|\underline{\underline{S^{r,s}_{a,b}}}\right| + \sum_{\substack{a,b \in occ \\ r,s \in unocc}} \langle rs|ab\rangle \left|\underline{\underline{S^{r}_{a}}}\right| \left|\underline{\underline{S^{s}_{b}}}\right| . \end{aligned} \tag{8.20}$$

The determinant $\left|\underline{\underline{S^{r,s}_{a,b}}}\right|$ may be simplified in a manner similar to that used in eq. 8.16. This is accomplished by considering $\underline{\underline{S^{r,s}_{a,b}}}$ as resulting from a single excitation $\underline{\underline{S^{r}_{a}}}$,

$$\left|\underline{\underline{S^{r,s}_{a,b}}}\right| = \left|\underline{\underline{S^{r}_{a}}}\right| \sum_{i \in occ} \langle \overline{\phi}_i | \phi_s \rangle \left[\underline{\underline{S^{r}_{a}}}\right]^{-1}_{b,i} . \tag{8.21}$$

Substituting eq. 8.16 into eq. 8.21 then leads to,

$$\left|\underline{\underline{S^{r,s}_{a,b}}}\right| = \left|\underline{\underline{S}}\right| \sum_{i,j \in occ} \langle \overline{\phi}_j | \phi_r \rangle \langle \overline{\phi}_i | \phi_s \rangle (\underline{\underline{S^{occ}}})^{-1}_{a,j} \left[\underline{\underline{S^{r}_{a}}}\right]^{-1}_{b,i} . \tag{8.22}$$

When Hückel theory is used for the solvent, the most computationally expensive step is the evaluation of eq. 8.16. PPP theory is much more computationally demanding, since it requires the evaluation of eq. 8.22.

Bibliography

[1] J. W. Mintmire and B. T. Dunlap C.T.White. Are fullerene tubules metallic? *Phys. Rev. Lett.*, 68:631, 1992.

[2] Chui-Lin Wang, Wen-Zheng Wang, and Zhao-Bin Su. *Phys. Rev. B*, 49(24):17468–17471, 1994.

[3] J. H. Burroughes, D. D. C. Bradley, A. R. Brown, R. N. Marks, K. Mackay, R. H. Friend, P. L. Burns, and A. B. Holmes. Light-emitting diodes based on conjugated polymers. *Nature*, 347:539, 1990.

[4] G. Gustafsson, Y. Cao, G. M. Treacy, F. Klavetter, N. Colaneri, and A. J. Heeger. Flexible light-emitting diodes made from soluble conducting polymers. *Nature*, 357:477, 1992.

[5] N. Tessler, G. J. Denton, and R. H. Friend. Lasing from conjugated-polymer microcavities. *Nature*, 382:695, 1996.

[6] F. Hide, M. A. Diaz-Garcia, B. J. Schwartz, M. R. Andersson, Q. Pei, and A. J. Heeger. Semiconducting polymers: a new class of solid-state laser materials. *Science*, 273:1833, 1996.

[7] Isabelle Ledoux and Joseph Zyss. *Novel Optical Materials and Applications: Molecular nonlinear optics: Fundamentals and applications.* John Wiley & Sons, Inc., NY, 1997.

[8] Joseph Zyss and Isabelle Ledoux. Nonlinear optics in multipolar media: Theory and experiments. *Chem. Rev.*, 94:77, 1994.

[9] D. R. Kanis, M. A. Ratner, and T. J. Marks. Design and construction of molecular assemblies with large second-order optical nonlinearities. quantum chemical aspects. *Chem. Rev.*, 94:195, 1994.

[10] S.R.Marder, J. W. Perry, G. Bourhill, C. B. Gorman, and B.G.Tiemann. Relation between bond-length alternation and second electronic hyperpolarizability of conjugated organic molecules. *Science*, 261:186, 1993.

[11] David P. Shelton and Julia E. Rice. Measurements and calculations of the hyperpolarizabilities of atoms and small molecules in the gas phase. *Chem. Rev.*, 94:3–29, 1994.

[12] F. Garnier, R. Hajlaoui, A. Yassar, and P. Srivastava. All-polymer field-effect transistor realized by printing techniques. *Science*, 265:1684, 1994.

[13] Ullrich Mitschke and Peter B

[14] P. Tavan and K. Schulten. Electronic excitations in finite and infinite polyenes. *Phys. Rev. B*, 36:4337, 1987.

[15] S. N. Dixit, D. Guo, and S. Mazumdar. Essential-states mechanism of optical nonlinearity in pi-conjugated polymers. *Phys. Rev. B*, 43:6781, 1991.

[16] S. Mazumdar and F. Guo. Observation of three resonances in the third harmonic generation spectrum of conjugated polymers: Evidence for the four-level essential states model. *J. Chem. Phys.*, 100:1665, 1994.

[17] Z. G. Soos, S. Ramasesha, and D. S. Galvao. Band to correlated crossover in alternating hubbard and ppp chains: nature of the lowest singlet excitation of conjugated polyers. *Phys. Rev. Lett.*, 71:1609, 1993.

[18] J. L. Bredas, C. Adant, P. Tackx, A. Persoons, and B. M. Pierce. Third-order nonlinear optical response in organic materials: theoretical and experimental aspects. *Chem. Rev.*, 94:243, 1994.

[19] Seth R. Marder, Lap-Tak Cheng, Bruce G. Tiemann, Friedli Andrienne C., Mireille Blanchard-Desce, Joseph W. Perry, and Jorgen Skindhoj. Large first hyperpolarizabilities in push-pull polyenes by tuning of the bond length alternation and aromacity. *Science*, 263:511, 1994.

[20] S. R. Marder, D. N. Beratan, and L.-T. Cheng. Approaches for optimizing the first electronic hyperpolarizability of conjugated organic molecules. *Science*, 252:103, 1991.

[21] Celine Fiorini, Fabrice Charra, Jean-Michel Nunzi, Ifor D. W. Samuel, and Joseph Zyss. Light-induced second-harmonic generation in an octupolar dye. *Opt. Lett.*, 20:2469, 1995.

[22] J. L. Oudar and D. S. Chemla. Theory of second-order susceptibilities of benzene substitutes. *Opt. Comm.*, 13:164, 1975.

[23] J. Hone, I. Ellwood, M. Muno, Ari Mizel, Marvin L. Cohen, A. Zettl, Andrew G. Rinzler, and R. E. Smalley. Thermoelectric power of single-walled carbon nanotubes. *Phys. Rev. Lett.*, 80:1042, 1998.

[24] M. Rohlfing and S. G. Louie. Optical excitations in conjugated polymers. *Phys. Rev. Lett.*, 82:1959, 1999.

[25] Philip G. Collins J. Hone Marvin L. Cohen S.G. Louie Keith Bradley, Seung-Hoon Jhi and A Zettl. Is the intrinsic thermopower of carbon nanotubes positive? *Phys. Rev. Lett.*, 85(20):4361, 2000.

[26] I. Ohmine, M. Karplus, and K. Schulten. Renormalized configuration interaction method for electron correlation in the excited states of polyenes. *J. Chem. Phys.*, 68:2298, 1978.

[27] J. Ridley and M. Zerner. An intermediate neglect of differential overlap technique for spectroscopy: pyrrole and the azines. *Theor. Chim. Acta*, 32:111, 1973.

[28] M. J. S. Dewar and W. Thiel. Ground states of molecules. 38. the mndo method. approximations and parameters. *J. Am. Chem. Soc.*, 99:4899, 1977.

[29] T. Hasegawa, Y. Iwasa, H. Sunamura, T. Koda, Y. Tokura, H. Tachibana, M. Matsumoto, and S. Abe. Nonlinear optical spectroscopy on one dimensional excitons in silicon polymer, polysilane. *Phys. Rev. Lett.*, 69:668, 1992.

[30] S. Abe, M. Schrieber, W. P. Su, and J. Yu. Nonlinear optical spectra of excitons in polydiacetylene. *J. Luminesc.*, 53:519, 1992.

[31] M. Chandross, S. Mazumdar, S. Jeglinski, X. Wei, Z. V. Vardeny, E. W. Kwock, and T. M. Miller. Excitons in poly(para-phenylenevinylene). *Phys. Rev. B*, 50:14702, 1994.

[32] Eric E. Moore and David Yaron. An explicit-solvent dynamic-dielectric screening model of electron-hole interactions in conjugated polymers. *J. Chem. Phys.*, 109:6147, 1998.

[33] N. Bloembergen. *Nonlinear Optics.* W. A. Benjamin, Inc., NY, 1965.

[34] J. O. Morley, V. J. Docherty, and D. Pugh. J. chem. soc., perkin trans. *J. Chem. Soc., Perkin Trans.*, 11:1351, 1987.

[35] D.S. Chemla and J. Zyss, editors. *Nonlinear Optical Properties of Organic Molecules and Crystals.* Academic Press, Inc., New York, 1987.

[36] Jean-Michel Nunzi, Fabrice Charra, Celine Fiorini, and Joseph Zyss. Transient optically induced non-centrosymmetry in a solution of octupolar molecules. *Chem. Phys. Lett.*, 219:349, 1994.

[37] Fabrice Charra, Fabrice Devaux, Jean-Michel Nunzi, and Paul Raimond. Picosecond light-induced noncentrosymmetry in a dye solution. *Phys. Rev. Lett.*, 68:2440, 1992.

[38] J. D. Jackson. *Classical Electrodynamics.* John Wiley & Sons, NY, 1975.

[39] Lionel Salem. *The molecular orbital theory of conjugated systems.* W. A. Benjamin, New York, 1966.

[40] D. Chemla J. Jerphagnon and R. Bonneville. The description of the physical properties of condensed matter using irreducible tensors. *Adv. in Phys.*, 27(4):609–650, 1978.

[41] C. G. Gray and K. E. Gubbins. *Theory of molecular fluids: Volume 1: Fundamentals.* Clarendon Press, Oxford, 1984.

[42] R. W. Terhune, P. D. Maker, and C. M. Savage. Measurements of nonlinear light scattering. *Phys. Rev. Lett.*, 14:681, 1965.

[43] Joseph Zyss, Thai Chau Van, Christophe Dhenaut, and Isabelle Ledoux. Harmonic rayleigh scattering from nonlinear octupolar molecular media: the case of crystal violet. *Chem. Phys.*, 177:281, 1993.

[44] Simon L. Altmann. *Band Theory of Solids: An Introduction from the Point of View of Symmetry.* Oxford University Press, NY, 1991.

[45] William Jones and Norman H. March. *Theoretical Solid State Physics, Volume 1: Perfect Lattices in Equilibrium.* Dover Publications, Inc., NY, 1973.

[46] Alejandro Pisanty. The electronic structure of graphite. *J. Chem. Ed.*, 68:804, 1991.

[47] J. L. Bredas, J. Cornil, D. Beljonne, D. DosSantos, A. Donizetti, and Z. Shuai. Excited-state electronic structure of conjugated oligomers and polymers: A quantum-chemical approach to optical phenomena. *Acc. Chem. Res.*, 32:267, 1999.

[48] W. P. Su, J. R. Schrieffer, and A. J. Heeger. Solitons in polyacetylene. *Phys. Rev. Lett.*, 42:1698, 1979.

[49] S. Brazovskii, N. Kirova, A. R. Bishop, V. Klimov, D. McBranch, N. N. Barashkov, and J. P. Ferraris. Excitations and optical properties of phenylene-based conjugated polymers and oligomers. *Optical Materials*, 9:472, 1998.

[50] D. Beljonne, Z. Shuai, J. Cornil, D. A. dos Santos, and J. L. Bredas. On the nature of electronic excitations in poly(paraphenylenevinylene): A quantum-chemical investigation. *J. Chem. Phys*, 111:2829, 1999.

[51] Yu. N. Gartstein, M. J. Rice, and E. M. Conwell. Charge conjugation symmetry breaking and the absorption spectra of polyphenylenes. *Phys. Rev. B*, 51:5546, 1995.

[52] M. Chandross, S. Mazumdar, M. Liess, P. A. Lane, Z. V. Vardeny, M. Hamaguchi, and K. Yoshino. Optical absorption in the substituted phenylene-based conjugated polymers: Theory and experiment. *Phys. Rev. B*, 55:1486, 1997.

[53] J. Cornil, D. Beljonne, R. H. Friend, and J. L. Bredas. Optical absorptions in poly(paraphyenylene vinylene) and poly(2,5-dimethoxy-1,4-paraphenylene vinylene) oligomers. *Chem. Phys. Lett.*, 223:82, 1994.

[54] E. K. Miller, D. Yoshida, C. Y. Yang, and A. J. Heeger. Polarized ultraviolet absorption of highly oriented poly(2-methoxy, 5-(2'-ethyl)-hexyloxy) paraphenylene vinylene. *Phys. Rev. B*, 59:4661, 1999.

[55] E. K. Miller, C. Y. Yang, and A. J. Heeger. Polarized ultraviolet absorption by a highly oriented dialkyl derivative of poly(paraphenylene vinylene). *Phys. Rev. B*, 62:6889, 2000.

[56] A. Kohler, D. A. dos Santos, D. Beljonne, Z. Shuai, J.-L. Bredas, A. B. Holmes, A. Kraus, K. Mullen, and R. H. Friend. Charge separation in localized and delocalized electronic states in polymeric semiconductors. *Nature*, 392:903, 1998.

[57] J. Fernandez Rico, R. Lopez, and G. Ramirez. Molecular integrals with slater basis. ii. fast computational algorithms. *J. Chem. Phys.*, 91:4213–22, 1989.

[58] A. Szabo and N. Ostlund. *Modern Quantum Chemistry: Introduction to Advanced Electronic Structure Theory*. Dover, New York, 1989.

[59] M. Kertesz. Bond length alternation and energy gap in $(\mathrm{ch})_x$. application of the intermediate exciton formalism. *Chem. Phys.*, 44:349, 1979.

[60]

[61] David Yaron and Robert Silbey. Effects of electron correlation on the nonlinear optical properties of polyacetylene. *Phys. Rev. B: Condens. Matter*, 45:11655, 1992.

[62] F. C. Spano and Z. G. Soos. Second hyperpolarizability of huckel rings: analytical results for size and alternation dependence. *J. Chem. Phys.*, 99:9265, 1993.

[63] David Yaron. Nonlinear optical response of conjugated polymers: essential excitations and scattering. *Phys. Rev. B: Condens. Matter*, 54:4609, 1996.

[64] M. J. S. Dewar, E. G. Zoebisch, E. F. Healy, and J. J. P. Stewart. Am1: A new general purpose quantum mechanical molecular model. *J. Am. Chem. Soc.*, 107:3902, 1985.

[65] Eric Moore, Benjamin Gherman, and David Yaron. Coulomb screening and exciton binding energies in conjugated polymers. *J. Chem. Phys.*, 106:4216, 1997.

[66] S. Iijima. *Nature*, 54:56, 1991.

[67] Paul Delaney, Hyoung Joon Choi, Jisoon Ihm, Steven G. Louie, and Marvin L. Cohen. *Nature*, 391(6666):466, 1998.

[68] J. W. Mintmire and C.T. White. *Synthetic Metals*, 77:231, 1996.

[69] J. W. Mintmire, B.I. Dunlap, and C. T. White. *Phys. Rev. Lett.*, 68(5):631, 1992.

[70] Riichiro Saito, Mitsutaka Fujita, G. Dresselhaus, and M.S. Dresselhaus. *Mat. Sci. and Engineering*, page 185, 1993.

[71] Yoshiyuki Miyamoto, Steven G. Louie, and Marvin L. Cohen. *Phys. Rev. Lett.*, 76(12):2121, 1996.

[72] R.A. Jishi, Daisuke Inomata, Kenji Nakao, M.S. Dresselhaus, and G. Dresselhaus. *J. Phys. Soc. Jpn.*, 63(6):2252, 1994.

[73] Noriaki Hamada, Shin ichi Sawada, and Atsushi Oshiyama. *Phys. Rev. Lett.*, 68(10):1579, 1992.

[74] H.F. Hu and K.L. Yao. *Mod. Phys. Lett. B*, 10(19):931–937, 1996.

[75] G. Stemann, C. Pépin, and M. Lavagna. *Phys. Rev. B*, 50(6):4075, 1994.

[76] Jaewan Kim and Wu-Pei Su. *Phys. Rev. B*, 50(12):8832, 1994.

[77] Tetsuya Mutou, Naokazu Shibata, and Kazuo Ueda. *Phys. Rev. B*, 57(21):13702–13705, 1998.

[78] Nenad Trinajstić. *Chemical Graph Theory.* CRC Press, Ann Arbor, 1992.

[79] Ante Graovac, Ivan Gutman, and Nenad Trinajstić. *Topological Approach to the Chemistry of Conjugated molecules.* Springer-Verlag, NY, 1977.

[80] D.E. Manolopoulos, D.R. Woodall, and P.W. Fowler. *J. Chem. Soc., Faraday Trans.*, 88(17):2427–35, 1992.

[81] David E. Manolopoulos, Douglas R. Woodall, and Patrick W. Fowler. *J. Chem. Soc. Faraday Trans.*, 88(17):2427–2435, 1992.

[82] Ira N. Levine. *Quantum Chemistry.* Prentice-Hall Inc., NJ, 1991.

[83] J. Hone, M. C. Llaguno, N. M. Nemes, A. T. Johnson, J. E. Fischer, D. A. Walters, M. J. Casavant, J. Schmidt, and R. E. Smalley. Electrical and thermal transport properties of magnetically aligned single wall carbon nanotube films. *Appl. Phys. Lett.*, 77(5):666, 2000.

[84] Steven G. Louie Seung-Hoon Jhi and Marvin L. Cohen. Electronic properties of oxidized carbon nanotubes. *Phys. Rev. Lett.*, 85(8).

[85] Philip G. Collins, Keith Bradley, Masa Ishingami, and A. Zettl. Extreme oxygen sensitivity of electronic properties of carbon nanotubes. *Science*, 287:1801, 2000.

[86] Neil W. Ashcroft and N. David Mermin. *Solid State Physics*. Holt, Rinehart and Winston, NY, 1976.

[87] N. C. Greenham, S. C. Morattl, D. D. C. Bradley, R. H. Friend, and A. B. Holmes. Efficient light-emitting diodes based on polymers with high electron affinities. *Nature*, 365:628, 1993.

[88] K. Lochner, H. Bassler, B. Tieke, and G. Wegner. Photoconduction in polydiacetylene multilayer structures and single crystals. evidence for band-to-band excitation. *Phys. Status Solidi B*, 88:653, 1978.

[89] L. Sebastian and G. Weiser. One-dimensional wide energy bands in a polydiacetylene revealed by electroreflectance. *Phys. Rev. Lett.*, 46:1156, 1981.

[90] L. Sebastian and G. Weiser. Electroreflectance studies on the exciton in pts and dchd single crystals. *Chem. Phys.*, 62:447, 1981.

[91] G. B. Blanchet, C. R. Fincher, and A. J. Heeger. Excitation profile for photogeneration of solitons in trans-(ch)x. *Phys. Rev. Lett.*, 51:2132, 1983.

[92] L. Rothberg, T. M. Jedju, P. D. Townsend, S. Etemad, and G. L. Baker. Femtosecond dynamics of photogenerated solitons and polarons in trans-polyacetylene. *Phys. Rev. Lett.*, 65:100, 1990.

[93] Z. V. Vardeny. Spectroscopy of photoexcitations in polyacetylene. *Prog. Theor. Phys. Suppl.*, 113:97, 1993.

[94] K. Pakbaz, C. H. Lee, A. J. Heeger, T. W. Hagler, and D. McBranch. Nature of the primary photoexcitations in poly(arylene-vinylenes). *Synth. Met.*, 64:295, 1994.

[95] I. H. Campbell, T. W. Hagler, D. L. Smith, and J. P. Ferraris. Direct measurement of conjugated polymer electronic excitation energies using metal/polymer/metal structures. *Phys. Rev. Lett.*, 76:1900, 1996.

[96] R. N. Marks, J. J. M. Halls, D. D. C. Bradley, R. H. Friend, and A. B. Holmes. The photovoltaic response in poly(p-phenylene vinylene) thin-film devices. *J. Phys., Condens. Matter*, 6:1379, 1994.

[97] M. Deussen, M. Scheidler, and H. Bassler. *Synth. Met.*, 73:123, 1995.

[98] J. M. Leng, S. Jeglinski, X. Wei, R. E. Benner, Z. V. Vardeny, F. Guo, and S. Mazumdar. Optical probes of excited states in poly(p-phenylenevinylene). *Phys. Rev. Lett.*, 72:156, 1994.

[99] P. Gomes da Costa and E. M. Conwell. Excitons and the band gap in poly(phenylene vinylene). *Phys. Rev. B*, 48:1993, 1993.

[100] Z. Shuai, J. L. Bredas, and W. P. Su. Nature of photoexcitations in poly(paraphenylene vinylene) and its oligomers. *Chem. Phys. Lett.*, 228:301, 1994.

[101] R. Knox. *Theory of Excitons, Solid State Physics: Supplement 5.* Academic Press, New York, 1963.

[102] Jurgen Hinze and H. H. Jaffe. Electronegativity. i. orbital electronegativity of neutral atoms. *J. Am. Chem. Soc.*, 84:540, 1962.

[103] D. J. Rowe. Equations-of-motion method and the extended shell model. *Rev. Mod. Phys.*, 40:153, 1968.

[104] J. Tomasi and M. Persico. Molecular interactions in solution: an overview of methods based on continuous distributions of the solvent. *Chem. Rev.*, 94:2027, 1994.

[105] M. W. Wong, K. B. Wiberg, and M. Frisch. Sovent effects. 3. tautomeric equilibria offormamide and 2-pyridone in the gas phase and solution. an ab initio scrf study. *J. Am. Chem. Soc.*, 114:1645, 1992.

[106] H. J. Kim, R. Bianco, B. J. Gertner, and J. T. Hynes. A simple basis set approach to solute electronic structure and free energy in solution. *J. Phys. Chem.*, 97:1723, 1993.

[107] When the electron and hole are on the same unit cell, $a = r$, the solute atoms are uncharged and Φ_a^r is equal to Φ_0. The basis functions $\psi_a^r \Phi_0$ and $\psi_a^r \Phi_a^r$ are then identical and are included only once in the basis.

[108] H. Thomann, L. R. Dalton, M. Grabowski, and T. C. Clarke. . *Phys. Rev. B*, 31:3141, 1985.

[109] S. Kuroda and H. Shirakawa. Electron-nuclear double-resonance evidence for the soliton wavefunction in polyacetylene. *Phys. Rev. B*, 35:9380, 1987.

[110] M. Mehring, A. Grupp, P. Hover, and H. Kass. The structure of the soliton in trans-polyacetylene: a pulsed endor investigation. *Synth. Met.*, 28:399, 1989.

[111] B. Kirtman, M. Hasan, and D. M. Chipman. Solitons in polyacetylene: magnetic hyperfine constants from ab initio calculations. *J. Chem. Phys.*, 95:7698, 1991.

[112] A. Szabo and N. Ostlund. *Modern Quantum Chemistry: Introduction to Advanced Electronic Structure Theory*. Dover, New York, 1989.